

**CATALYTIC FUNDAMENTALS OF AQUEOUS PHASE
REFORMING: A SPECTROSCOPIC APPROACH**

A Dissertation
Presented to
The Academic Faculty

by

Bryan J. Hare

In Partial Fulfillment
of the Requirements for the Degree
Doctor of Philosophy in the
School of Chemical & Biomolecular Engineering

Georgia Institute of Technology
December 2022

COPYRIGHT © 2022 BY BRYAN J. HARE

CATALYTIC FUNDAMENTALS OF AQUEOUS PHASE REFORMING: A SPECTROSCOPIC APPROACH

Approved by:

Dr. Carsten Sievers, Advisor
School of Chemical & Biomolecular
Engineering
Georgia Institute of Technology

Dr. Jake D. Soper
School of Chemistry & Biochemistry
Georgia Institute of Technology

Dr. Christopher Jones
School of Chemical & Biomolecular
Engineering
Georgia Institute of Technology

Dr. Rachel B. Getman
Department of Chemical and
Biomolecular Engineering
Clemson University

Dr. Andrew J. Medford
School of Chemical & Biomolecular
Engineering
Georgia Institute of Technology

Date Approved: November 08, 2022

ACKNOWLEDGEMENTS

I would like to first and foremost thank Dr. Carsten Sievers for the provided mentorship and professional development over the past few years. He welcomed me into his research group with open arms and supplied me with all the resources I needed to make this project a success. We had many intriguing scientific debates and discussions that improved my ability to formulate hypotheses, think critically about every possibility, and vividly express my conclusions in both voice and writing. He has also shown by example that by working smarter, rather than harder, you can accomplish great things while maintaining a healthy work-life balance (as evidenced by his sick guitar skills and strong devotion to cardio).

I would also like to thank the other members of my doctoral committee. Dr. Christopher Jones, Dr. Andrew J. Medford, Dr. Jake D. Soper, and Dr. Rachel B. Getman have all been very generous with their support and feedback on the progress of my dissertation throughout the years. The patience and understanding they expressed during the Covid-19 pandemic when I struggled to obtain preliminary data for my Ph.D. proposal was very much appreciated.

Dr. Rachel Getman deserves a special thanks, along with various members of her research group at Clemson University including Tianjun Xie, Paul J. Meza-Morales, and Ricardo A. Garcia Carcamo. The results of their modeling and computational work was integral for corroborating many of the conclusions and perspectives within this dissertation that would not have been as strong with experimental evidence alone. Even when Dr. Sievers and I decided to take a slightly different direction on the experimental side, they

were very accommodating in developing models and performing calculations that were not a part of the original project outline.

It was a great pleasure to work alongside many of the Sievers Research Group members throughout the years. Many of them including Dr. Giada Innocenti, Dr. Sean Najmi, Dr. Andrew Tricker, Dr. Michael Stellato, and Olivia Williams were also very contributing to my training and development. Of course let's not forget George, the Bossy Basset, who practically served as the laboratory mascot and brightened everyone's day.

I very much appreciate the assistance from various scientists that helped me acquire essential data. There is Dr. Yong Ding from the Georgia Tech School of Materials Science and Engineering who helped me obtain fantastic micrograms of my catalysts which were irrefutably crucial for this project. Consultations with Dr. Anibal Ramirez Cuesta and Dr. Yongqiang Cheng regarding the capabilities of vibrational spectroscopy with inelastic neutron scattering along the assistance provided by Dr. Luke Daemen to run those experiments are also greatly appreciated.

I'm also grateful for chemical engineering undergraduates Erika Yamazaki and Melanie Henderson for assisting me with experiments and allowing me to put my own mentorship skills to the test.

None of this would have been possible without funding from the National Science Foundation and the Dow Chemical Company. For the government officials that accepted my advisor's original grant proposal, thank you for allowing me to pay bills and put food on my plate while pursuing my education. A special thanks to Dr. Carlos Villa, Dr. Sukaran Arora, and Dr. Sandeep Dhingra from the Dow Chemical Company for funding the final

portion of my Ph.D. curriculum and allowing me to expand my skillset to include electrocatalysis.

I would also like to thank various national and Georgia-based institutions including Jackson Associates Research, WeAudition, Ava Grace Casting (previously Castellanos Casting), Destination Casting, Casting Taylormade, various academic film departments (namely SCAD, Clayton State, UGA), the PRC Marketing Corporation, CM Chicken, Chick-fil-A, and eBay. Enough said there.

Before I enrolled as a Ph.D. student at the Georgia Institute of Technology, I had the pleasure of working under Dr. John Kuhn and his graduate students in the Heterogeneous Catalysis & Materials Chemistry Group at the University of South Florida. In the five years I worked in this research group, from the beginning of my sophomore undergraduate year to the end of my Masters degree program, I was lucky enough to have an amazing advisor and the best graduate student mentors. I give full credit to Dr. Yolanda Daza and Dr. Debtanu Maiti for getting me excited about scientific research, providing me with the skills to work and think independently, and ultimately inspiring me to go further and pursue a doctorate degree in chemical engineering.

My family has been incredibly supportive throughout my academic journey. My parents have always stressed the importance of getting a good education and using what intellect I have to make the world a better place. My older sister, Jessie Brangan, had always serve as a role model and also inspired me when she finished her master's curriculum. I don't think anyone in my family anticipated me being in school for this long, so I'm thinking they might have emphasized the importance of education a bit too much.

Nonetheless, the love and unchanging support are things I will always cherish and never forget.

Lastly, I must give a big thanks to the love of my life, Christina-Anne Hare, who provided so much support and took my hand in marriage during my curriculum. Not only has she been extremely patient with me whenever I had late nights, but she was always a good listener when I came home from tough days. She helped me wind down over the weekends with wine from North Georgia, reminded me to call my mother, and even got me off the air mattress I slept on throughout the whole first year. Nothing inspires me to keep working hard more than envisioning the future we'll share together. I can't wait to see what the next chapter of our lives has in store for us. P.S. I love you more.

TABLE OF CONTENTS

| | |
|---|-------------|
| ACKNOWLEDGEMENTS | iii |
| LIST OF TABLES | x |
| LIST OF FIGURES | xii |
| LIST OF SYMBOLS AND ABBREVIATIONS | xv |
| SUMMARY | xvii |
| CHAPTER 1. Introduction | 1 |
| 1.1 Hydrogen: Applications and Sources | 1 |
| 1.2 Aqueous Phase Reforming of Polyols | 1 |
| 1.3 APR Surface Chemistry | 3 |
| 1.4 Infrared Spectroscopy and Adsorbed Carbon Monoxide | 5 |
| 1.5 Objectives and Outline | 7 |
| CHAPTER 2. The Dehydrogenation Reaction | 8 |
| 2.1 Introduction | 8 |
| 2.2 Materials and Methods | 9 |
| 2.2.1 Catalyst Synthesis | 9 |
| 2.2.2 Catalyst Characterization | 10 |
| 2.2.3 Pyridine Adsorption | 11 |
| 2.2.4 Infrared Spectroscopy | 11 |
| 2.3 Results | 12 |
| 2.3.1 Catalyst Characterization | 12 |
| 2.3.2 Formation of Surface Species from Methanol Adsorption | 15 |
| 2.3.3 Influence of Pt Particle Size | 16 |
| 2.3.4 Effects of co-adsorbed H ₂ O on Methanol Dehydrogenation | 20 |
| 2.3.5 Rates of CO Formation | 24 |
| 2.4 Discussion | 26 |
| 2.4.1 Interpretation of Adsorbed CO Spectra | 26 |
| 2.4.2 Pt Particle Size Effects on Dehydrogenation Activity | 28 |
| 2.4.3 Inter-adsorbate Interactions | 29 |
| 2.4.4 Effects of Co-adsorbed H ₂ O | 32 |
| 2.5 Conclusion | 34 |
| CHAPTER 3. Surface Chemistry of Di/Ketones on Lewis Acidic γ-Al₂O₃ | 36 |
| 3.1 Introduction | 36 |
| 3.2 Materials and Methods | 39 |
| 3.2.1 Experimental | 39 |
| 3.2.2 Computational | 41 |
| 3.3 Results | 43 |
| 3.3.1 Mesityl Oxide and Acetone | 44 |

| | | |
|--------------------|---|------------|
| 3.3.2 | Hydroxyacetone | 48 |
| 3.3.3 | Dihydroxyacetone | 51 |
| 3.3.4 | 2,4 Pentanedione | 53 |
| 3.3.5 | 2,3 Butanedione and 3,4 Hexanedione | 56 |
| 3.3.6 | 2,5 Hexanedione | 62 |
| 3.3.7 | Density Functional Theory | 64 |
| 3.4 | Discussion | 67 |
| 3.4.1 | Steric and Electronic Effects of Hydroxyl Groups | 68 |
| 3.4.2 | Influence of Alkyl Group Length | 69 |
| 3.4.3 | Intramolecular interactions of carbonyl groups and their effect on the formation of surface species | 70 |
| 3.4.4 | Impact of an Aqueous Phase | 71 |
| 3.5 | Conclusion | 72 |
| CHAPTER 4. | Pt catalyst Poisoning by di/ketones | 74 |
| 4.1 | Introduction | 74 |
| 4.2 | Materials and Methods | 77 |
| 4.2.1 | Materials | 77 |
| 4.2.2 | Infrared spectroscopy | 78 |
| 4.2.3 | Inelastic neutron scattering | 79 |
| 4.2.4 | Density Functional Theory | 80 |
| 4.3 | Results | 81 |
| 4.3.1 | Characterization | 81 |
| 4.3.2 | Di/Ketone adsorption on small Pt particles | 82 |
| 4.3.3 | Di/Ketone adsorption on large Pt particles | 85 |
| 4.3.4 | Evolution of CO _L band integrals | 88 |
| 4.3.5 | Inelastic neutron scattering | 90 |
| 4.3.6 | DFT Models of Adsorbate Configuration | 94 |
| 4.3.7 | Thermodynamics of potential reaction paths of surface methyl groups | 98 |
| 4.4 | Discussion | 100 |
| 4.4.1 | Decarbonylation of di/ketones on small and large Pt particles | 100 |
| 4.4.2 | Poisoning by alkyl groups and derivatives | 102 |
| 4.4.3 | Poisoning by molecular di/ketones | 103 |
| 4.4.4 | Possibilities for improving APR catalyst and process robustness | 106 |
| 4.5 | Conclusions | 108 |
| CHAPTER 5. | Summary and recommendations | 110 |
| 5.1 | Summary | 110 |
| 5.2 | Recommendations for Future Work | 112 |
| 5.2.1 | Experiments in the Aqueous Phase | 112 |
| 5.2.2 | Promotion of Highly Coordinated Metal Sites | 114 |
| 5.2.3 | Improving Catalyst Tolerance Against Di/Ketones and Alkyl Groups | 115 |
| 5.2.4 | Alternative Catalyst Supports | 117 |
| APPENDIX A. | Supplementary Information for Chapter 2 | 119 |
| A.1 | Lewis Acid Site Concentrations | 119 |
| A.2 | Methanol-derived Surface Species on γ-Al₂O₃ | 120 |

| | | |
|--|---|------------|
| A.3 | Effects of Chlorine | 124 |
| A.4 | H₂O Adsorption | 125 |
| APPENDIX B. Supplementary Information for Chapter 3 | | 127 |
| B.1 | DFT Cells | 127 |
| B.2 | IR Spectra of Vapor Phase Di/Ketones | 129 |
| B.3 | Full IR Spectra of Adsorbed Di/Ketones | 131 |
| B.4 | Supplementary IR Spectra | 132 |
| B.5 | Supplementary DFT Calculations | 137 |
| APPENDIX C. Supplementary Information for Chapter 4 | | 138 |
| C.1 | DFT Cells | 138 |
| C.2 | Full IR Spectra of Adsorbed Di/Ketones | 139 |
| C.3 | INS Spectra of Di/Ketones | 141 |
| REFERENCES | | 142 |

LIST OF TABLES

| | | |
|----------|--|-----|
| Table 1 | Characterization data for γ -Al ₂ O ₃ and all Pt/ γ -Al ₂ O ₃ catalysts. | 13 |
| Table 2 | Di/Ketone reagents adsorbed to γ -Al ₂ O ₃ . | 40 |
| Table 3 | IR band assignments for acetone and mesityl oxide adsorption on γ -Al ₂ O ₃ under HV at 50 – 250 °C. | 47 |
| Table 4 | IR band assignments for hydroxyacetone adsorption on γ -Al ₂ O ₃ under HV at 50 – 250 °C. | 50 |
| Table 5 | IR band assignments for 2,4 pentanedione adsorption on γ -Al ₂ O ₃ under HV at 50 – 250 °C. | 55 |
| Table 6 | IR band assignments for 2,3 butanedione and 3,4 hexanedione adsorption on γ -Al ₂ O ₃ under HV at 50 – 250 °C. | 61 |
| Table 7 | DFT-calculated binding energies for γ -Al ₂ O ₃ -adsorbed diketones, relative to that of acetone. | 66 |
| Table 8 | Ketone and diketone reagents adsorbed to Pt/ γ -Al ₂ O ₃ catalysts. | 78 |
| Table 9 | Fractional decreases in total CO _L band integrals at 250 °C following di/ketone and methanol TPDs on Pt/ γ -Al ₂ O ₃ catalysts under HV. | 90 |
| Table 10 | INS band assignments for di/ketones adsorbed on a Pt sponge. | 93 |
| Table 11 | Binding energies for Pt(111)-adsorbed di/ketones. | 98 |
| Table 12 | Reaction energies for processes on Pt(111) that produce and consume methyl groups under APR conditions. | 99 |
| Table B1 | Infrared band assignments for vapor-phase di/ketones. | 130 |
| Table B2 | Geometrical parameters of γ -Al ₂ O ₃ -adsorbed acetone and diketones. | 137 |

| | | |
|-------|---|-----|
| Table | DFT-calculated binding energies for γ -Al ₂ O ₃ -adsorbed diketones, | 137 |
| B3 | relative to that of acetone. | |

LIST OF FIGURES

| | | |
|-----------|--|----|
| Figure 1 | Polyol APR reaction sequence. | 2 |
| Figure 2 | STEM micrograms of Pt/ γ -Al ₂ O ₃ catalysts. | 14 |
| Figure 3 | IR spectra of adsorbed methanol on γ -Al ₂ O ₃ and Pt/ γ -Al ₂ O ₃ . | 16 |
| Figure 4 | CO _L stretching bands in infrared spectra obtained during temperature-programmed conversion of methanol adsorbed on Pt/ γ -Al ₂ O ₃ catalysts. | 18 |
| Figure 5 | Spectroscopic data for methanol adsorption on various dry Pt/ γ -Al ₂ O ₃ catalysts. | 20 |
| Figure 6 | IR spectra of temperature-programmed methanol dehydrogenation on R700 and the commercial catalyst with and without co-adsorbed H ₂ O. | 21 |
| Figure 7 | Position and fractional peak of the CO _L stretching peak after methanol adsorption on various hydrated Pt/ γ -Al ₂ O ₃ catalysts. | 23 |
| Figure 8 | CO stretching bands during isothermal (150 °C) kinetic experiments with methanol dehydrogenation on R500 and the commercial catalyst with and without H ₂ O. | 25 |
| Figure 9 | Deconvolution of the 1500 – 1750 cm ⁻¹ region of IR spectra for adsorbed mesityl oxide and acetone at 50 °C with corresponding temperature-dependent band integrals up to 250 °C. | 45 |
| Figure 10 | Deconvolution of the 1500 – 1800 cm ⁻¹ region of the IR spectrum of adsorbed hydroxyacetone on γ -Al ₂ O ₃ at 50 °C. with Corresponding temperature-dependent band integrals up to 250 °C. | 49 |
| Figure 11 | Infrared spectra (ν (C=O) region) of surface species formed from dihydroxyacetone adsorption on γ -Al ₂ O ₃ (prepared in the aqueous phase) during TPD experiments from 50 to 250 °C. | 52 |
| Figure 12 | Deconvolution of the 1500 – 1750 cm ⁻¹ region of the IR spectrum of adsorbed 24PD/Hacac on γ -Al ₂ O ₃ at 50 °C. b) Development of the ν (CH) stretching region during the TPD experiment. | 54 |
| Figure 13 | Deconvolution of the 1500 – 1800 cm ⁻¹ region of the IR spectrum of adsorbed 2,3 butanedione and 3,4 hexanedione on γ -Al ₂ O ₃ at 50 | 57 |

°C with corresponding temperature-dependent band integrals up to 250 °C.

| | | |
|-----------|--|-----|
| Figure 14 | Mid-IR spectrum region of 2,3 butanedione adsorbed on γ -Al ₂ O ₃ . | 59 |
| Figure 15 | Infrared spectra (ν (C=O) region) of 2,5 hexanedione adsorbed on γ -Al ₂ O ₃ (prepared via ex-situ impregnation) during TPD experiments from 50 to 250 °C. | 63 |
| Figure 16 | Lowest energy configurations of γ -Al ₂ O ₃ -adsorbed diketones | 65 |
| Figure 17 | Illustrations of theorized catalyst poisons that may result from the non-selective adsorption and dehydrogenation of secondary alcohol groups on Pt/ γ -Al ₂ O ₃ . | 76 |
| Figure 18 | Sequence of TPDs with poisoning species and methanol as observed by IR spectroscopy. | 79 |
| Figure 19 | IR spectra of adsorbed CO during TPD experiments with Pt _S / γ -Al ₂ O ₃ (~1.1 nm Pt particles) and methanol + di/ketones up to 250 °C. | 83 |
| Figure 20 | IR spectra of adsorbed CO during TPD experiments with Pt _L / γ -Al ₂ O ₃ (~4.6 nm Pt particles) and methanol + di/ketones up to 250 °C. | 86 |
| Figure 21 | Integrals of the ν (C≡O) IR band during poison adsorption and subsequent methanol adsorption from 50 to 250 °C. | 89 |
| Figure 22 | INS of spectra of Pt-bound surface species formed from acetone, 2,3 butanedione, and 3,4 hexanedione. | 92 |
| Figure 23 | Optimized configurations of ketones adsorbed to a Pt(111) slab under vacuum. | 95 |
| Figure 24 | Optimized configurations of diketones adsorbed to a Pt(111) slab under vacuum. | 97 |
| Figure A1 | Lewis acidity of γ -Al ₂ O ₃ and Pt/ γ -Al ₂ O ₃ catalysts | 119 |
| Figure A2 | Full IR spectra of methanol adsorption on γ -Al ₂ O ₃ at various temperatures. | 122 |
| Figure A3 | Residual OH stretching modes on activated γ -Al ₂ O ₃ and the low frequency IR regime of adsorbed methanol on chlorinated γ -Al ₂ O ₃ at different temperatures. | 124 |

| | | |
|-----------|---|-----|
| Figure A4 | Effect of Cl on the CO _L stretching bands after impregnation with HCl. | 125 |
| Figure A5 | IR spectrum of surface species following exposure of R700 to 0.5 mbar H ₂ O vapor at 50 °C. | 125 |
| Figure A6 | IR spectra of temperature-programmed methanol dehydrogenation on R300 and R500 with and without co-adsorbed H ₂ O. | 126 |
| Figure B1 | The simulation supercell for the clean γ -Al ₂ O ₃ . | 127 |
| Figure B2 | Different adsorbate orientations in a γ -Al ₂ O ₃ simulation supercell. | 128 |
| Figure B3 | Infrared spectra of vapor-phase di/ketones. | 129 |
| Figure B4 | Full IR spectra of γ -Al ₂ O ₃ -adsorbed di/ketones. | 131 |
| Figure B5 | IR spectra of acetone adsorption and conversion kinetics on γ -Al ₂ O ₃ at 50 °C. | 132 |
| Figure B6 | IR spectra of TPD of adsorbed H ₂ O on γ -Al ₂ O ₃ . | 133 |
| Figure B7 | Infrared spectra (ν (C=O) region) of γ -Al ₂ O ₃ -adsorbed pyruvaldehyde during TPD experiments from 50 to 250 °C. | 134 |
| Figure B8 | Infrared spectra (ν (C-H) region) of γ -Al ₂ O ₃ -adsorbed 2,3 butanedione during TPD experiments from 50 to 250 °C. | 135 |
| Figure B9 | Infrared spectra (ν (C=O) region) of γ -Al ₂ O ₃ -adsorbed 3-methylcyclopent-2-en-1-one (prepared via ex-situ impregnation) during TPD experiments from 50 to 250 °C. | 136 |
| Figure C1 | DFT simulation supercell for Pt(111). | 138 |
| Figure C2 | Full IR spectra during TPD experiments with PtS/ γ -Al ₂ O ₃ (~1.1 nm Pt particles) with methanol + di/ketones up to 250 °C. | 139 |
| Figure C3 | Full IR spectra during TPD experiments with PtL/ γ -Al ₂ O ₃ (~4.6 nm Pt particles) with methanol + di/ketones up to 250 °C. | 140 |
| Figure C4 | Reference inelastic neutron scattering spectra for some free di/ketone reagents. | 141 |

LIST OF SYMBOLS AND ABBREVIATIONS

Symbols

| | |
|---------------------------------|---|
| A | Integral of the 1440 cm^{-1} IR band attributed to pyridine adsorbed to Lewis acid sites on $\gamma\text{-Al}_2\text{O}_3$ |
| C_w | Concentration of Lewis acid sites |
| C_x | Surface concentration of element X |
| $E_{\text{Adsorbate}}$ | Electronic energy of a di/ketone adsorbate in vacuum |
| $E_{\text{Adsorbate}^*}$ | Electronic energy of an adsorbed di/ketone on Pt(111) |
| $E_{\text{Adsorbed acetone}}$ | Energy of adsorbed acetone on $\gamma\text{-Al}_2\text{O}_3$ |
| $E_{\text{Adsorbed molecule}}$ | DFT-calculated energy of an adsorbed di/ketone on $\gamma\text{-Al}_2\text{O}_3$ |
| E_{Binding} | DFT-calculated binding energy of a di/ketone or methyl group adsorbed to Pt(111) |
| $E_{\text{Gas phase acetone}}$ | Energy of gas phase acetone |
| $E_{\text{Gas phase molecule}}$ | Energy of a gas phase di/ketone |
| $E_{\text{Relative Binding}}$ | DFT-calculated binding energy of an adsorbed di/ketone on $\gamma\text{-Al}_2\text{O}_3$ relative to that of adsorbed acetone |
| E_{Slab} | Electronic energy of the Pt(111) slab |
| I_x | Orbital band integral of element X |
| S | Probed area of catalyst wafer during experiments under high vacuum |
| S_x | Sensitivity factor of element X |
| W | Mass of catalyst wafer in IR beam path during experiments under high vacuum |
| ϵ | Extinction coefficient for pyridine adsorbed to Lewis acid sites of $\gamma\text{-Al}_2\text{O}_3$ |

Abbreviations

| | |
|--|--|
| Acac | Acetylacetate surface species derived from 2,4 pentanedione adsorption on γ -Al ₂ O ₃ |
| APR | Aqueous phase reforming |
| BET | Brunauer-Emmet-Teller theory |
| CO _B | Carbon monoxide adsorbed in a bridging orientation |
| CO _L | Carbon monoxide adsorbed in a linear orientation |
| Com.Cat. | Commercially obtained 5% Pt/ γ -Al ₂ O ₃ catalyst |
| DFT | Density functional theory |
| Hacac | 2,4 pentanedione enol tautomer |
| HV | High vacuum |
| INS | Inelastic neutron scattering |
| IR | Infrared |
| ORNL | Oakridge National Laboratory |
| Pt _L / γ -Al ₂ O ₃ | Pt/ γ -Al ₂ O ₃ with larger Pt particles |
| Pt _S / γ -Al ₂ O ₃ | Pt/ γ -Al ₂ O ₃ with smaller Pt particles |
| R300 | Synthesized 1% Pt/ γ -Al ₂ O ₃ catalyst reduced at 300 °C |
| R500 | Synthesized 1% Pt/ γ -Al ₂ O ₃ catalyst reduced at 500 °C |
| R700 | Synthesized 1% Pt/ γ -Al ₂ O ₃ catalyst reduced at 700 °C |
| SNS | Spallation Neutron Source |
| STEM | Scanning transmission electron microscopy |
| TPD | Temperature-programmed desorption |
| VASP | Vienna Ab initio Stimulation Package |
| XPS | X-ray photoelectron spectroscopy |
| 24PD | 2,4 pentanedione diketo tautomer |

SUMMARY

Hydrogen is an invaluable commodity of the chemical industry and acquiring it from renewable sources is irrefutably essential for establishing a more sustainable future. The (hemi)cellulosic portion of plant-based biomass stores a notable quantity of atomic hydrogen that can be efficiently and economically extracted via aqueous phase reforming (APR) of biomass derivatives. APR is a liquid phase heterogeneous catalytic process that can deconstruct various reagents into light weight gaseous products. The conversion of polyols ($C_xH_{2x+2}O_x$) is of high interest due to the stoichiometric formation of H_2 and CO_2 through the dehydrogenation \rightarrow decarbonylation \rightarrow water-gas shift reaction sequence. Much time and effort has been allocated to engineering research involving transition metal catalyst screening, reaction parameters, and complex reactor design. The chemistry side has been seldom touched in comparison. This includes important catalytic mechanisms such as metal site-sensitivity, solvent effects, and catalyst deactivation. Infrared (IR) spectroscopy is a powerful technique that can be employed to exploit these phenomena by monitoring the surface species on a catalyst. By better understanding the precise surface chemistry of APR constituent reactions in this thesis, future catalyst designs may be tailored to improve the efficiency of APR, and thus renewable hydrogen production.

Chapter 1 briefs the theory behind carbon monoxide adsorption on transition metal catalysts and related surface phenomena. Not only is adsorbed CO an important reaction intermediate in APR, but the IR band attributed to linearly adsorbed CO (CO_L), normally observed within the $1900 - 2100\text{ cm}^{-1}$ range, is extremely sensitive to the catalyst surface, making an in-depth analysis of the band a sufficient approach to studying APR reactions.

The Blyholder model was adapted herein which describes the interaction between CO and metals as a combined mutual exchange of electrons through dative σ -bonding and π -back bonding. The extent of this electron exchange, and thus the features of the CO_L band, can be affected by several factors including the coordination of the adsorbing metal site, co-adsorbed species, catalyst impurities, and adlayer configuration. With the fundamentals of CO adsorption reviewed and capabilities of IR spectroscopy fully understood, in-depth analyses of the CO_L band can be used to form conclusions for the studies herein focused on APR catalytic mechanisms.

Chapter 2 focuses on dehydrogenation, the first constituent reaction of APR. Herein, Pt/ γ - Al_2O_3 catalysts with different Pt particle size distributions were synthesized and characterized to vary the distribution of highly and lowly coordinated metal sites. The average Pt particle size of synthesized catalysts ranged between 1.0 and 1.3 nm while a commercially obtained Pt/ γ - Al_2O_3 catalyst was characterized with an average Pt particle size of 4.6 nm. These catalysts were also used in subsequent chapters. To isolate the dehydrogenation reaction, methanol was used as a reagent given the absence of any C-C bonds. Methanol dehydrogenation was performed within a high vacuum (HV) IR cell with self-supported catalyst wafers. Evolution of the CO_L band was monitored during temperature-programmed desorption (TPD) experiments up to 450 °C and with respect to time during isothermal kinetic experiments at 150 °C with and without co-adsorbed H_2O . Larger band integrals at lower temperatures and asymmetric development of the CO_L band at early exposure strongly suggested that larger Pt particles, or highly coordinated Pt sites, are more active in the dehydrogenation reaction.

Chapter 3 covers the employment of IR spectroscopy to observe the surface chemistry of various ketones and diketones adsorbed to Lewis acidic γ -Al₂O₃. It was crucial to understand the chemistry between these di/ketone reagents and the catalyst support prior to the following study (Chapter 4) which involved di/ketone adsorption on Pt/ γ -Al₂O₃ catalysts. This study looked at the effects of hydroxyl groups (acetone vs di/hydroxyacetone acetone), intramolecular carbonyl distance (α , β , γ -diketones), and alkyl chain length (butanedione vs hexanedione) on reactivity and product selectivity. A custom Python code was used to deconvolute the 1500 – 1800 cm⁻¹ region of which bands are commonly assigned to ν (C=O) and ν (C=C) modes. Aldol self-condensation was observed to be the most common reaction with adsorbed di/ketones (with some exceptions) which involved sequential enolization, condensation, and dehydration into conjugated products as evident by the appearance of broad features around 1500 – 1550 cm⁻¹. Density-functional theory (DFT) was also used to obtain configurations and calculate binding energies of γ -Al₂O₃-adsorbed diketones. Herein, Lewis acid-catalyzed reaction mechanisms of di/ketone reagents were presented and the necessary prerequisite knowledge for the following study was acquired.

Chapter 4 looks to identify a potential Pt deactivation mechanism due to poisoning by strong binding surface species. A reoccurring trend in literature shows that H₂ yields generally decrease with the trend CH₃OH \approx C₂H₆O₂ > C₃H₈O₃ > C₆H₁₄O₆. Given that H₂ decrease starting with glycerol, a 3-carbon reagent, it is possible that the nonselective adsorption by and dehydrogenation of secondary alcohol groups of larger reagents form strong binding ketone poisons. Furthermore, even larger reagents such as sorbitol could potentially form multidentate diketone poisons. The poisoning capability of di/ketones, the

same ones used in the previous chapter, were tested on Pt/ γ -Al₂O₃ with different metal particle sizes. Experiments consisted of two sequential TPD experiments: the first of which involved the di/ketone poison and the second which involved attempted dehydrogenation of methanol on the poisoned catalyst. The shortcoming of the CO_L band integral, compared to that resulting from methanol dehydrogenation on a clean catalyst, was quantified as the extent of poisoning. While the strongest di/ketone poisoned appeared dependent on Pt particle size, larger Pt particles appeared more active in the decarbonylation reaction, the second APR constituent reaction, given the formation of larger CO_L bands during di/ketone TPDs. This also suggested that strong binding alkyl groups resulting from decarbonylation were present on the Pt surface, as evidenced by bands in vibrational spectra obtained with inelastic neutron scattering. Furthermore, DFT was used to model di/ketone adsorbates on Pt(111) and calculate adsorbate binding energies and reaction energies of possible reactions involving methyl groups. Conjugated species on γ -Al₂O₃, identified in the previous chapter, may also play a role in deactivating interfacial sites.

Chapter 5 includes perspectives on what approaches can be taken in future research studies to improve APR catalyst efficiency and poison resistance based on the results of this thesis.

CHAPTER 1. INTRODUCTION

1.1 Hydrogen: Applications and Sources

Hydrogen is one of the most important commodities in the chemical and fuel industries, a climate friendly compound expected to play a key role in the transition from petroleum-based processes to renewable alternatives.¹⁻² It remains an essential element for various processes including biomass upgrading,³ ammonia production,⁴ and Fischer-Tropsch synthesis.⁵ In the current state, however, about 96% of H₂ production relies on the processing of non-renewable resources such as coal, oil, and natural gas; the remainder obtained primarily via H₂O electrolysis.⁶ A promising alternative is the utilization of (hemi)cellulosic biomass as a secure, abundant, and renewable source of H₂.⁷ Commonly known methods include direct pyrolysis and gasification of feedstocks as well as reforming of biomass-derived species such as ethanol.⁸ However, these processes are energy intensive because they require high temperatures to both vaporize components and surpass energy barriers, while hydrogen yields can be limited due to by-product formation.⁹ It is therefore necessary to explore alternative processes to ensure a competitive edge for biorefineries within the future energy industry.

1.2 Aqueous Phase Reforming of Polyols

Aqueous phase reforming (APR) has recently garnered much attention as a feasible catalytic process with unattained potential to extract H₂ directly from biomass-derived oxygenates.¹⁰⁻¹¹ In theory, this catalyzed molecular deconstruction can be performed with many different feedstock reagents to obtain H₂, CO₂, and even light alkanes.¹²⁻¹⁴ Operating

at moderate temperatures (usually 210-250 °C) and continuous flow,¹⁵ APR is notably compatible with conventional biorefinery technology and capable of directly processing the effluent of (hemi)cellulose hydrolysis.¹⁶ They can both be performed in liquid-phase with heterogeneous catalysts at elevated pressures (necessary in APR for preventing H₂O vaporization and easy separation of gas products).¹⁷ The H₂O acts as both a safe, environmentally friendly solvent as well as an oxidation agent and can be recycled. These intriguing benefits have captivated the attention of numerous research groups that have thus engaged in catalyst screening,¹⁸⁻²² optimization,^{14, 23-24} and reactor design.²⁵⁻²⁶ Heterogeneous APR catalysts are often supported transition metals of which the metal identity strongly determines product selectivity. For instance, Pt is well known to demonstrate high selectivity towards hydrogen gas, while Ni preferentially forms alkanes.¹⁴

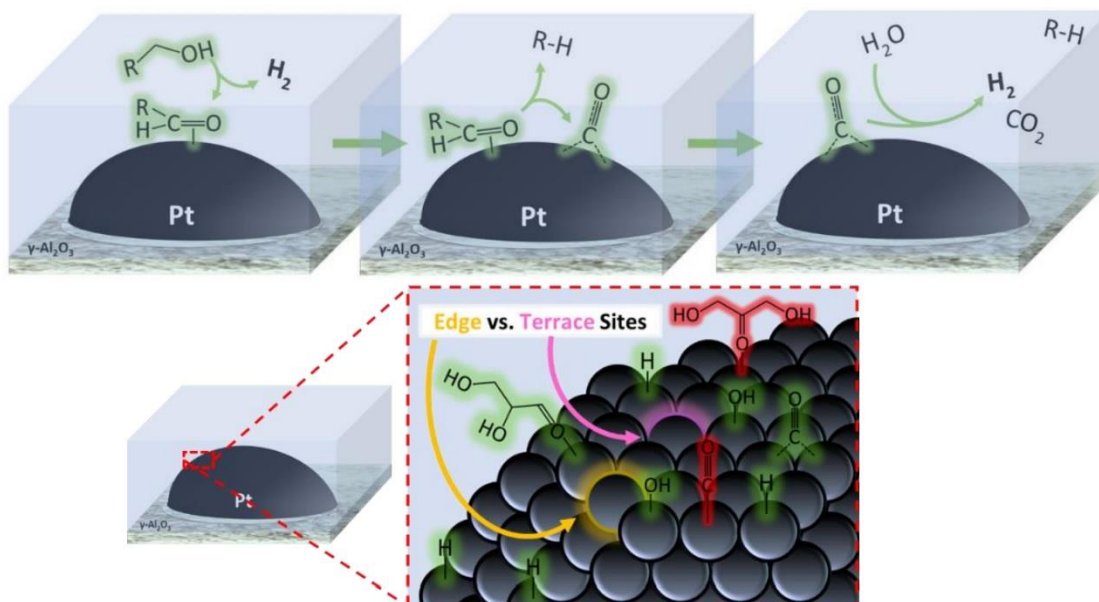
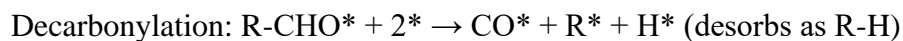
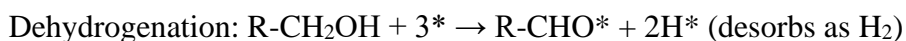


Figure 1. Polyol APR reaction sequence: Dehydrogenation → Decarbonylation → Water-gas shift (top). Surface complexity of the aqueous phase reforming catalyst (bottom).

The conversion of polyol reagents ($C_xH_{2x+2}O_x$) in particular is of great interest due to the theoretical possibility of achieving stoichiometric quantities of H_2 and CO_2 . Not only would this result in higher yields and more efficient production of H_2 , but it would also omit the need for downstream gas separation units necessary to remove alkanes. However, the complete conversion of a polyol reagent occurs through a specific sequence of reactions: Dehydrogenation \rightarrow Decarbonylation \rightarrow Water-gas shift (**Figure 1**). In summary, a polyol reagent dehydrogenates and forms hydrogen and an aldehyde intermediate upon adsorption. Surface hydrogen may associate and desorb as molecular H_2 . The aldehyde intermediate subsequently undergoes decarbonylation to form adsorbed carbon monoxide while the resulting polyol fragment may recirculate back to the adsorption and dehydrogenation step. Adsorbed carbon monoxide is further oxidized by H_2O (catalytically split into OH and H surface species) to produce more H_2 along with CO_2 .

1.3 APR Surface Chemistry

On supported metal catalysts, such as $Pt/\gamma-Al_2O_3$, the constituent reactions take place on open metal sites, depicted as $*$.



Following adsorption and conversion, product surface species must desorb back into the liquid phase to make these metal sites available again for further utilization. This is an essential function of catalytic materials that are employed over long periods of time.

From a chemistry point of view, variance in metal particle size reflects a varying distribution of edge and terrace sites will ultimately effect reaction yields and efficiency. Large Pt particles possess crystal facets that accommodate a large fraction of highly coordinated (high N) Pt atoms, commonly referred to as terrace sites. On the contrary, small Pt particles fall short of this quality and accommodate more exposed, lowly coordinated (low N) Pt atoms labeled as edges, corners, etc. These classified sites possess distinguishable electronic and steric characteristics and may exhibit different catalytic activities. While altering metal particle size undoubtedly changes the distribution of edges and terraces, each constituent reaction of APR may exhibit contingency on different metal sites and unique surface chemistry. Dehydrogenation may potentially display a kinetic preference for lowly coordinated metal, while the decarbonylation reaction may favor highly coordinated metal. It is therefore essential to isolate the individual steps necessary to gain a true understanding of the entire APR mechanism. In addition to the distribution of metal sites, a plethora of chemical species further complicates the catalyst surface (**Figure 1**). Adsorbed hydrogen and carbon monoxide are expected to be direct results of dehydrogenation and decarbonylation, respectively. These species are dominant during the conversion of small oxygenates such as methanol and ethylene glycol. However, larger oxygenates such as glycerol or sorbitol are contemplated to bind to metal sites with a greater diversity of resulting surface species. Aldehyde intermediates form adsorption by primary alcohol groups are capable of subsequent decarbonylation in the desired APR

pathway.²⁷ On the other hand, adsorption by secondary OH groups or simultaneous adsorption by multiple OH groups result in byproduct carbonyl species. Some of these additional species, yet to be confirmed, are suspected of causing the decrease in H₂ yields witnessed when converting oxygenates of increasing size; i.e. poisoning the catalyst. Huber et al. revealed a decrease in H₂ yield with increasing size of the feed molecule in the order ethylene glycol > glycerol > sorbitol.²⁸ More recently, a major decrease in short-term activity, specifically in reference to the formation of adsorbed CO (spectroscopically observed), was recently observed with the trend: glycerol > sorbitol > glucose.²⁹ Similar to the APR constituent reactions, surface species derived from large oxygenates are expected to behave differently depending on the adsorbing metal site. For instance, a dihydroxyacetone intermediate formed from glycerol may bind more strongly to, or act as a stronger poison on, Pt edge sites compared to terrace sites. It will therefore be important to probe the surface of well-characterized materials while performing both desired and side reactions with different reagents suitable for isolating the corresponding kinetics.

1.4 Infrared Spectroscopy and Adsorbed Carbon Monoxide

Infrared (IR) spectroscopy is a powerful analytical technique that has proven its practicality in numerous fields over the past several decades.³⁰ For chemistry research, it can reveal the vibrational modes, and therefore functional groups, of virtually any organic chemical that exhibits dipole moments.³¹ This can also include those of surface species adsorbed to catalytic materials such as the intermediates and products of a reaction. In particular, many strives have been made to develop methods and improve quality of IR spectra of surface species during *in-situ* APR and other pressurized liquid-phase

reactions.³²⁻³³ The most effective approach today involves coating a cylindrical internal reflection element (IRE) with a thin catalyst layer to circumvent both pressure gradients that are detrimental to the IRE along with the dominating presence of IR bands attributed to the solvent phase.³⁴ These developments have allowed researchers to study the overall effectiveness of various catalysts in practical APR conditions; i.e. elevated temperatures and pressures. However, traditional experimental studies involving the spectral probing of reactions under vacuum conditions has proven sufficient for studying catalytic fundamentals and mechanisms. In the context of APR, due to many of the mechanisms behind dehydrogenation, decarbonylation, and Pt deactivation often being overlooked, experiments under vacuum could suffice herein. This would involve the adsorption of small partial pressures of a reagent to a prepared catalyst with and without the presence of co-adsorbed water and subsequent analysis of IR bands attributed to essential intermediates and products.

Adsorbed carbon monoxide is an essential intermediate in APR, resulting from the dehydrogenation of small polyols such as methanol or the decarbonylation of larger $C_{\geq 3}$ polyols.²⁹ Adsorbed CO on Pt exhibits a strong presence in the IR spectrum, with the linearly adsorbed species (CO_L) often observed in the $1900 - 2100\text{ cm}^{-1}$ region.³⁵ The corresponding band integral can be used to gauge the extent of conversion for any reaction that produces adsorbed CO. For example, a CO_L band integral that grows with increasing temperature during a reaction suggests that higher conversion is achieved at higher temperatures. Furthermore, both the chemical and electronic nature of adsorbed CO_L is extremely sensitive to the surrounding environment on a catalyst surface. Historical studies including one by Hollins reveals how several factors such as, but not limited to, metal site

coordination, co-adsorbed species, and surface impurities can shift the stretching frequency, also depicted as $\nu(\text{C}\equiv\text{O})$ herein.³⁶ Therefore, the CO_L band observed during experiments consisting of reagent adsorption and reaction could be deconvoluted to exploit CO species on different metal sites and in different environments. This strategy would offer much information of regarding active sites and solvent effects in APR constituent reactions.

1.5 Objectives and Outline

The focus of this work is allocated to better understanding the catalytic mechanisms of APR constituent reactions. This can be achieved by observing the respective surface chemistry on $\text{Pt}/\gamma\text{-Al}_2\text{O}_3$ catalysts with various average metal particle sizes using IR spectroscopy. Chapter 2 highlighted the particle size-dependency as well as the effects of co-adsorbed H_2O on methanol dehydrogenation throughout temperature-programmed desorption and isothermal kinetic experiments with analytical emphasis on IR bands affiliated with adsorbed CO in the $1750 - 2100\text{ cm}^{-1}$ region. Chapter 3 involved the adsorption of various di/ketones on $\gamma\text{-Al}_2\text{O}_3$ with deconvolution of features observed in the $1500 - 1800\text{ cm}^{-1}$ to identify products formed from acid-base catalysis. This served as a prerequisite for the following study. Chapter 4 covered the poisoning effects of pre-adsorbed di/ketones and derivative species on $\text{Pt}/\gamma\text{-Al}_2\text{O}_3$ catalysts during methanol dehydrogenation as well as the metal particle-size dependency of decarbonylation activity. The experimental work in this chapter was accompanied by configurations and energy calculations obtained via density functional theory to establish trends and descriptors for Pt poisoning efficacy. Finally, Chapter 5 briefs the main conclusions from this work and discusses potential directions for future work based on the results presented herein.

CHAPTER 2. THE DEHYDROGENATION REACTION

2.1 Introduction

The first step of the desired reaction sequence is dehydrogenation, which involves breaking C-H and O-H bonds until a catalytically stable intermediate or product is reached.^{10, 37} Because APR activity is known to be influenced by metal particle size, the dehydrogenation of oxygenates is likely to exhibit an observable dependency as well. Structure sensitivity has been reported for dehydrogenation reactions involving various types of alcohols (aryl, alkyl, etc.).³⁸⁻⁴¹ For example, the turnover frequency of benzyl alcohol dehydrogenation on Au/hydrotalcite catalysts increased from ~ 0.08 to ~ 0.23 s⁻¹ as the average Au particle size was decreased from between 4 and 12 to 2.1 nm.³⁸ It was proposed that metal atoms with low coordination numbers (e.g., edge and corner sites) are much more active towards alcohol dehydrogenation than those of high coordination (terrace sites) for this particular reaction.

To best isolate the dehydrogenation reaction in a way that is practical for advancing mechanistic knowledge of APR, methanol can be utilized given that it can dehydrogenate but not undergo decarbonylation or side reactions that are prevalent during APR. In a recent computational study, we showed differences in the thermodynamics of C-H and O-H bond cleavage for methanol adsorbed on a Pt(111) terrace and at the interface between a small Pt cluster and a Lewis acidic Al₂O₃ support.⁴² It was determined that Pt terrace sites are generally more active in C-H cleavage while those that are undercoordinated and located at the Pt/Al₂O₃ interface are more active in O-H cleavage. For the overall dehydrogenation reaction, an experimental approach can further support these findings and provide a better

understanding of the particle size effect on the kinetics. However, the dehydrogenation of oxygenates in APR comes with additional complexities. In addition to structural sensitivity, the presence of interfacial H₂O cannot be ignored. As a co-adsorbate, H₂O can affect the electronic structure of surrounding metal atoms, compete for surface sites, and solvate adsorbed intermediates or transition states and thus influence cleavage of C-H and O-H bonds.⁴³⁻⁴⁴

To gain fundamental insight into the APR mechanism, methanol conversion on Pt/ γ -Al₂O₃ catalysts in high vacuum (HV) was probed by infrared spectroscopy to isolate the dehydrogenation reaction. Pt particle sizes were varied to adjust the ratio of metal sites with different coordination. The features of IR bands (i.e., shapes, integrals, frequencies) corresponding to the adsorbed CO product provided much information during temperature-dependent and time-resolved experiments regarding the activity of different metal sites along with the effects of co-adsorbed water.

2.2 Materials and Methods

2.2.1 Catalyst Synthesis

1% Pt/ γ -Al₂O₃ was synthesized by wet impregnation. The γ -Al₂O₃ powder (Alfa Aesar 99.97%) was continuously stirred as a 20 mL aqueous solution of dissolved chloroplatinic acid hydrate, H₂PtCl₆ (Sigma-Aldrich ≥ 99.9 trace metals basis), was added in increments with drying and stirring in between. The water for synthesis and experiments was pretreated with a Purelab Classic Elga LabWater deionizer. The impregnated γ -Al₂O₃ powder was then calcined at 500 °C for 4 h in air prior to reduction at (300, 500, or 700 °C for 3 h in 7% (v/v) H₂/Ar. Synthesized samples were named in accordance with their

reduction temperatures: R300, R500, and R700. The results of the synthesized catalyst were also compared to that of a 5% Pt/ γ -Al₂O₃ commercial catalyst (Sigma-Aldrich #205974)

2.2.2 Catalyst Characterization

An aberration-corrected Hitachi HD 2700 scanning transmission electron microscope (STEM) was used to image supported Pt particles. The resulting high-angle annular dark-field images were acquired with an electron beam convergent angle of 27 mrad and a detector collection angle of 70-370 mrad. Average Pt particle sizes and Pt particle size distributions were determined by manual measurements of 300 – 500 particles per sample.

A Thermo-Scientific Scanning X-ray photoelectron spectrometer (XPS) was used to calculate the surface composition of Pt/ γ -Al₂O₃ catalysts. Samples were placed under vacuum with pressure below 4.5×10^{-7} mbar. The excitation source utilized focused monochromatic Aluminum K-Alpha X-rays (1.486 keV) with an incident angle of 60 ° normal to the sample. Due to the overlapping of the Pt 4f band by the Al 2p band, surface compositions were calculated with a metal-free basis through manual integrations. Surface compositions were calculated using sensitivity factors of 0.537, 2.93, and 2.285 for the Al 2p, O 1s, and Cl 2p bands,⁴⁵ respectively, along with **Equation (1)**:

$$C_x = \frac{I_x/S_x}{\sum_i I_i/S_i} \quad (1)$$

Where C, I, and S are the surface concentration, orbital band integral, and sensitivity factor of element X, respectively. The carbon peak was centered at 284.4 eV.

A Micromeritics ASAP 2020 analyzer was used for N₂ physisorption and surface area measurements. All samples were initially degassed at 200 °C for 6 hr. The surface area was determined based on the BET method.⁴⁶

2.2.3 *Pyridine Adsorption*

The Lewis acidity of the catalysts was measured through temperature-programmed desorption of pyridine followed by IR spectroscopy. A Thermo Scientific Nicolet iS10 spectrometer was used to observe pyridine adsorption on catalyst wafers within a HV chamber with the same parameters as the methanol adsorption experiments. Catalyst wafers were activated at 450 °C for 1 h prior to the incremental dosing of pyridine vapor at 150 °C until the pressure equilibrated at ~0.1 mbar. The HV chamber was evacuated and the same temperature program used for methanol experiments was performed. The strength of acid sites was assessed based on the temperature at which they can retain pyridine under HV. The concentration of Lewis acid sites was calculated with **Equation (2)**:

$$C_w = \frac{S \times A}{\varepsilon \times W} \quad (2)$$

Where S is the circular area of the catalyst wafer probed by IR spectroscopy, A is the integral of the 1440 cm⁻¹ band resulting from pyridine adsorption on γ -Al₂O₃ Lewis acid sites, ε is an extinction coefficient of 1.71 cm/ μ mol used for γ -Al₂O₃,⁴⁷ W is the weight of the probed area, and C_w is the concentration of Lewis acid sites.

2.2.4 *Infrared Spectroscopy*

IR spectroscopy experiments were conducted using a Thermo Scientific Nicolet 8700 FT-IR spectrometer with an MCT/A detector. All spectral data was acquired and

processed using Thermo Scientific Omnic software. Infrared spectra were obtained with 64 scans using an aperture of 75, optical velocity of 1.8988, and resolution of 1.928 cm⁻¹. Catalyst powders were hydraulically pressed into thin wafers that were placed in a HV chamber with ZnSe windows. Once HV conditions were reached, the catalyst wafer was activated at 450 °C (10 °C/min) for 1 h prior to measuring a spectrum of the pretreated catalyst. The catalyst was then exposed to 0.5 mbar of methanol (VWR International ≥99.8%) vapor at 50 °C and allowed to equilibrate. For experiments involving methanol adsorption on hydrated catalyst surfaces, the catalyst was exposed to 0.5 mbar of DI water vapor and allowed to equilibrate before dosing methanol. Following another evacuation, the saturated catalyst was then sequentially exposed to temperatures of 150, 250, 350, and 450 °C (10 °C/min) with natural cooling in between to obtain all scans at 50 °C. The spectrum of the dry catalyst surface was subtracted from those with H₂O- and methanol-derived surface species.

2.3 Results

2.3.1 Catalyst Characterization

All Pt/ γ -Al₂O₃ catalysts were characterized to illustrate the impact of various synthesis procedures. The BET surface areas of all catalysts were comparable between 63 and 71 m²/g, and no significant changes were witnessed with respect to reduction temperature (**Table 1**). Calculated Lewis acidities (**Figure A1**) showed a consistent decrease in acid site concentrations with respect to temperature between different samples. The Lewis acidity of bare γ -Al₂O₃ gradually declined from 104 μ mol/g at 150 °C to 35

$\mu\text{mol/g}$ at 450 °C. Those of the Pt/ $\gamma\text{-Al}_2\text{O}_3$ remained consistently lower ($\sim 10 - 30 \mu\text{mol/g}$) due to the obstruction of acid sites (coordinatively unsaturated Al^{3+} sites⁴⁸) by Pt particles. STEM micrograms (**Figure 2**) verified the increased average particle size with increasing reduction temperature (**Table 1**). Not only do the micrograms reveal high dispersion of Pt nanoparticles across the $\gamma\text{-Al}_2\text{O}_3$ surface (for R500 and the commercial catalyst in Figures 1a and 1c, respectively), but also the presence of some single Pt atoms on R300. Overall, Pt particles on in-house synthesized 1% Pt/ $\gamma\text{-Al}_2\text{O}_3$ catalysts possessed average diameters of 0.5 - 2 nm. These small particles innately possess a large fraction of lowly coordinated Pt sites. On the contrary, the 5% Pt/ $\gamma\text{-Al}_2\text{O}_3$ commercial catalyst exhibited a much wider distribution of Pt particle sizes from about 2 - 7 nm and an average size that was 3-5 times larger than those of the synthesized samples. Thus, this material contained a large fraction of highly coordinated Pt sites, or terrace sites.

Table 1. Characterization data for $\gamma\text{-Al}_2\text{O}_3$ and all Pt/ $\gamma\text{-Al}_2\text{O}_3$ catalysts.

| Sample | $\gamma\text{-Al}_2\text{O}_3$ | Synthesized 1% Pt/ $\gamma\text{-Al}_2\text{O}_3$ | | | Pt/ $\gamma\text{-Al}_2\text{O}_3$ com. cat. |
|--|--------------------------------|---|--------|--------|---|
| | | R300 | R500 | R700 | |
| Average Pt particle size (nm) | - | 1.0 | 1.1 | 1.3 | 4.6 |
| BET Surface Area (m^2/g) | 54 | 63 | 71 | 66 | 70 |
| Cl % (metal free basis) | 0 % | 0.64 % | 0.52 % | 0.00 % | 0.00 % |
| Actual Pt loading (by wt.) | - | 0.84 % | | | 3.62 % |

The residual chlorine content from the utilization of H_2PtCl_6 during wet impregnation was measured by XPS on a metal-free basis (**Table 1**). Thus, these atomic

percentages should only be considered as a trend between synthesized catalysts. As expected, the residual chlorine content declined with increasing reduction temperature; from 0.64 % at 300 °C to 0 % at 700 °C.

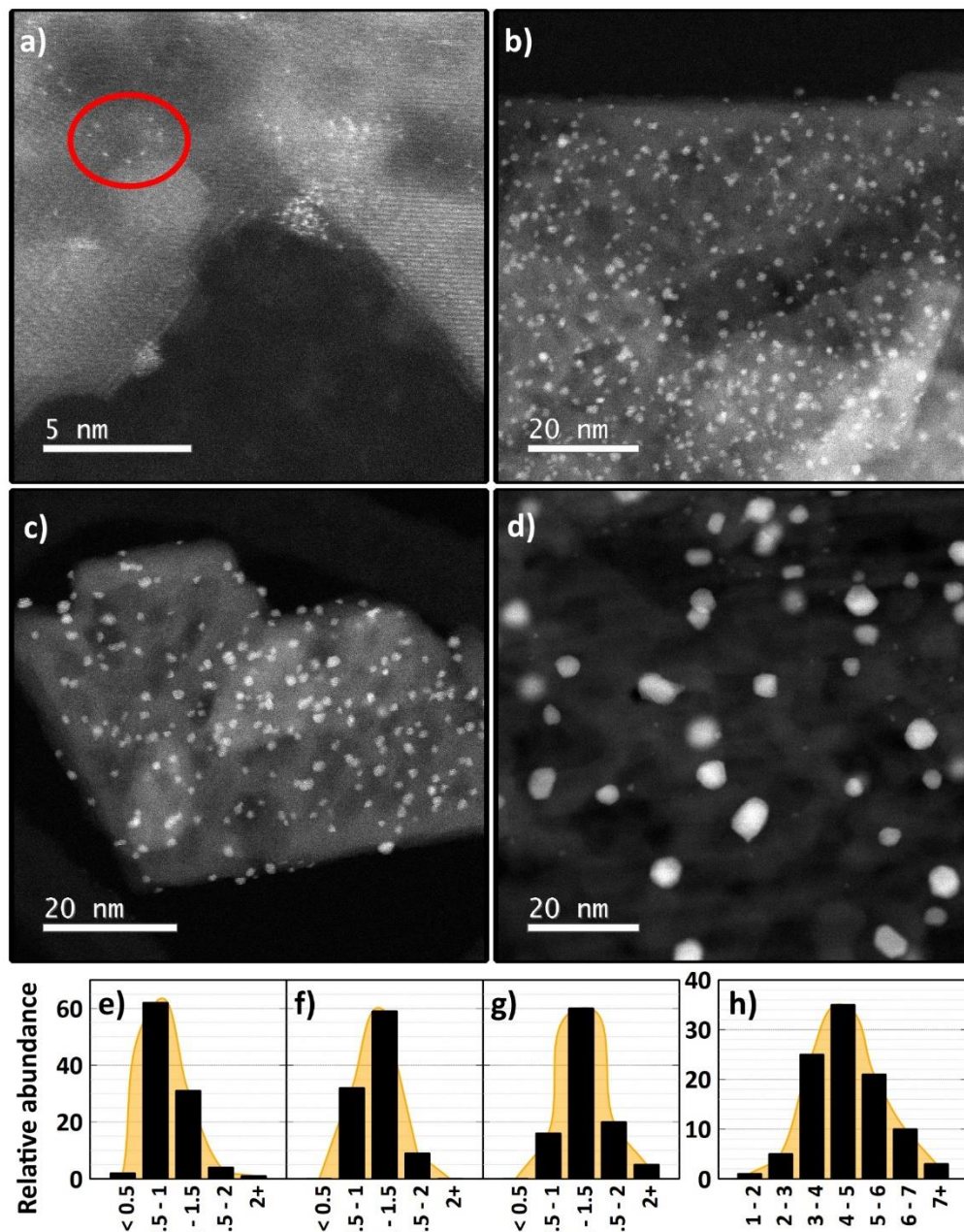


Figure 2. STEM micrograms of Pt/Al₂O₃ catalysts. **a)** R300 with a group of single Pt atoms (red oval), **b)** R500, **c)** R700, and **d)** the commercial catalyst. Particle size distributions of **e)** R300, **f)** R500, **g)** R700, and **h)** the commercial catalyst.

2.3.2 Formation of Surface Species from Methanol Adsorption

The adsorption of methanol on $\gamma\text{-Al}_2\text{O}_3$ resulted in the emergence of several IR bands (**Figure A2** for $\gamma\text{-Al}_2\text{O}_3$ and **Figure A3** for chlorinated $\gamma\text{-Al}_2\text{O}_3$). These bands are assigned based on previous work by Busca et al.⁴⁹ A broad band at $\sim 3000\text{-}3500\text{ cm}^{-1}$ represented the $\nu(\text{O-H})$ modes of hydrogen bonding OH groups from adsorbed methanol and the alumina support. This is accompanied by a group of higher frequency negative bands at 3675 , 3732 , and 3766 cm^{-1} that represent the non-hydrogen bonding surface hydroxyl groups of $\gamma\text{-Al}_2\text{O}_3$ prior to methanol adsorption.⁴⁹ A large band at 1095 cm^{-1} was accompanied by smaller high and low frequency shoulders centered at 1190 and 1034 cm^{-1} , respectively. These bands were associated with $\nu(\text{C-O})$ modes of different methanol-derived surface species. Two medium bands with multiple shoulders appeared centralized at 2954 and 2818 cm^{-1} . Much of this contribution is due to the asymmetric and symmetric $\nu(\text{CH}_x)$ modes of different species. Weak bands conglomerated at 1476 and 1420 cm^{-1} were due to CH_x deformations.

The same bands were seen during methanol adsorption on $\text{Pt}/\gamma\text{-Al}_2\text{O}_3$ catalysts (**Figure 3**). The presence of Pt particles during methanol adsorption resulted in an additional strong band centered at $2048\text{-}2080\text{ cm}^{-1}$ and a much weaker broad band at $1700\text{-}1850\text{ cm}^{-1}$. These bands were assigned to the stretching modes of CO bound to Pt in the linear (CO_L) and bridging (CO_B) coordinations, respectively.⁵⁰ The former species typically represents “one-fold” binding, while the latter typically represents two- or three-fold binding. Formation of adsorbed carbon monoxide species indicates complete dehydrogenation of methanol. Increased temperatures resulted in increased integrals associated with CO with concomitant decreases in the bands affiliated with other

methanol-derived species on γ -Al₂O₃, indicating higher conversions were achieved at higher temperatures.

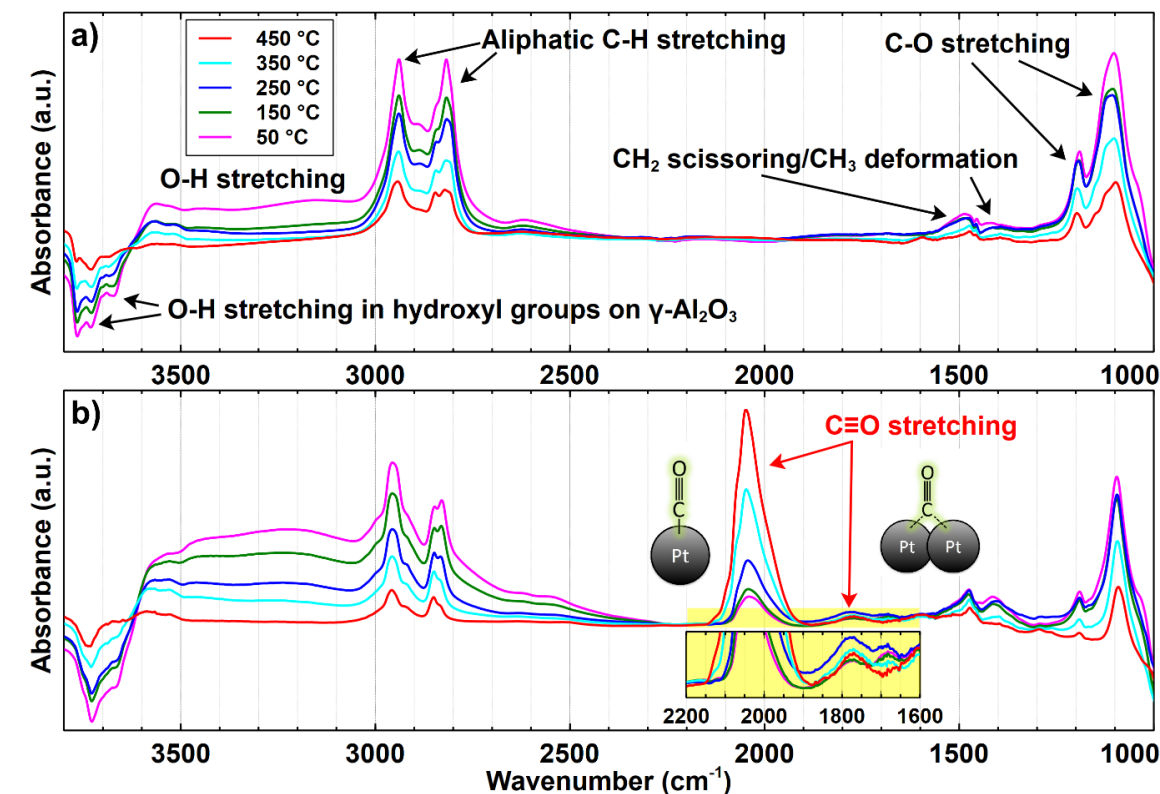


Figure 3. Infrared spectra of adsorbed methanol **a)** γ -Al₂O₃ and **b)** Pt/ γ -Al₂O₃ catalysts (R500) under HV with major vibrational modes labeled. Temperature labels refer to reaction temperature, but all spectra were obtained at 50 °C after allowing the system to cool in ambient air.

2.3.3 Influence of Pt Particle Size

The temperature-dependent evolution of the CO_L stretching band varied between different Pt/ γ -Al₂O₃ samples with different metal particle size distributions (**Figure 4**). These bands maintained a notable broadness throughout the whole temperature range, suggesting that the metal sites exhibit a wide range of coordination and interactions with

other elements on the catalyst surface.⁵¹⁻⁵² Distinct features were present within the entire range of 1900 – 2150 cm⁻¹.

For all synthesized Pt/ γ -Al₂O₃ samples, the highest intensity was observed within the narrow range of 2048 – 2052 cm⁻¹. For the commercial catalyst, the band centered at 2079 cm⁻¹ dominated the region. Each spectrum consisted of a broad low-frequency shoulder that extended as low as 1900 cm⁻¹. The relative intensity of this shoulder became less significant as the Pt particle size increased, suggesting these particular metal sites became less common as metal particles sintered together. We attribute this broad feature to CO_L adsorbed near the Pt/ γ -Al₂O₃ interface with a weaker C \equiv O bond due to interactions with Lewis acid sites.^{42, 53}

The bands for the synthesized Pt/ γ -Al₂O₃ samples possessed high-frequency shoulders. The shoulder at 2071-2074 cm⁻¹ appeared at 250 °C for R300 and as low as 50 °C for R500 and R700. This particular mode appears to correspond to the primary CO_L band of the commercial catalyst, centered at 2079 cm⁻¹. While this band is also associated with CO_L on metal sites, we attributed this slight increase in $\nu(\text{C}\equiv\text{O})$ frequency to dipole-dipole coupling between adjacent adsorbed CO_L species.⁵⁴ An additional high frequency shoulder was observed at 2100 cm⁻¹ for the R300 and R500 samples. This was more evident for the CO_L band for R300 and was completely absent for the spectra of R700 and the commercial catalyst. One possible assignment for these particular bands is CO adsorbed on Pt sites that are partially oxidized (Pt ^{δ +}) due to residual Cl left behind by the H₂PtCl₆ synthesis precursor. Cl was completely removed from the surface during reduction at 700 °C as confirmed by XPS, which may explain the absence of the band on spectra for the R700 sample. To further support this assignment, the same methanol dehydrogenation

experiment was performed on a sample of R700 that was dosed with HCl to achieve 5 wt. % Cl (**Figure A4**). Not only did the high frequency shoulder emerge with similar intensity as that on R300, but the entire CO_L band blue-shifted by about 30 cm^{-1} . Another possible contribution to these high-frequency bands is CO adsorption on isolated Pt atoms, an assignment made in other studies.⁵⁵⁻⁵⁶ Single metal atoms could engage in charge transfer with Lewis acidic supports and become slightly oxidized, thus resulting in higher $\nu(\text{C}\equiv\text{O})$ frequencies.⁵⁷ While the STEM micrograms revealed the occasional single Pt atom (**Figure 2**), we expect these atoms to sinter with higher reduction temperatures which also explain the disappearance of the band on the spectra for R700. Each of these assignments are further discussed and justified later.

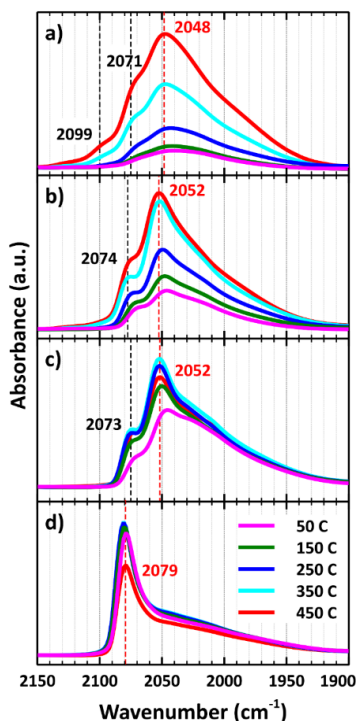


Figure 4. CO_L stretching bands in infrared spectra obtained during temperature-programmed conversion of methanol adsorbed on $\text{Pt}/\gamma\text{-Al}_2\text{O}_3$: **a)** R300, **b)** R500, **c)** R700, **d)** commercial catalyst. Absorption band magnitudes are normalized for direct comparison.

Changes to the $\nu(\text{C}\equiv\text{O})_{\text{L}}$ frequency with increasing reaction temperature were observed for each Pt/ γ - Al_2O_3 sample (**Figure 5**). For R300, the $\nu(\text{C}\equiv\text{O})$ band remained low at $\sim 2042\text{ cm}^{-1}$ until the temperature reached $350\text{ }^\circ\text{C}$ when it shifted to $2047\text{--}2048\text{ cm}^{-1}$. The $\nu(\text{C}\equiv\text{O})$ frequency of CO on R500 exhibited a more linear trend, starting at 2046 cm^{-1} at $50\text{ }^\circ\text{C}$ and approaching 2052 cm^{-1} at $450\text{ }^\circ\text{C}$. Until $350\text{ }^\circ\text{C}$, the $\nu(\text{C}\equiv\text{O})_{\text{L}}$ frequency for R700 remained about 2 cm^{-1} higher than that for R500, but it also plateaued at 2052 cm^{-1} above $250\text{ }^\circ\text{C}$. The $\nu(\text{C}\equiv\text{O})$ frequency for CO_{L} adsorbed on the commercial catalyst remained at $2080 \pm 1\text{ cm}^{-1}$ for the whole experiment which is well above that of the synthesized samples (note the y axis break in **Figure 5**).

The integrals of the cumulative CO_{L} bands (i.e., $1900 - 2150\text{ cm}^{-1}$) were obtained at each reaction temperature and plotted as normalized fractions with respect to the maximum area obtained for the respective catalyst sample (**Figure 5**). At $50\text{ }^\circ\text{C}$, R300 achieved only 11% of its maximum observed integral. In contrast, the CO_{L} band integrals at $50\text{ }^\circ\text{C}$ for R500, R700 and the commercial catalyst reached 26, 70, and 90% of their maximum areas, respectively. This suggests that larger Pt particles, or highly coordinated Pt atoms, are more active in methanol dehydrogenation at lower temperatures. The R700 and commercial catalyst reached their maximum CO_{L} integrals at $350\text{ }^\circ\text{C}$, while those with smaller Pt particles required $450\text{ }^\circ\text{C}$.

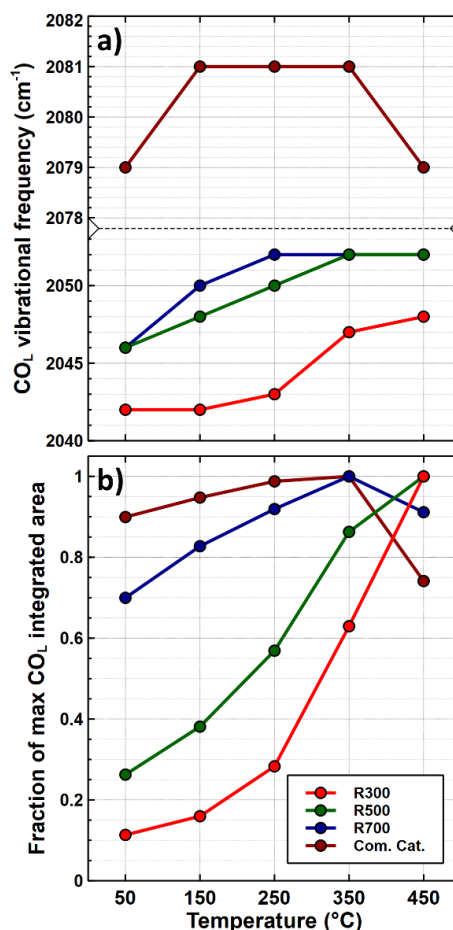


Figure 5. Spectroscopic data for methanol adsorption on various Pt/γ-Al₂O₃ catalysts. Changes in **a)** vibrational frequency and **b)** integrals of the CO_L stretching vibrational mode with increasing reaction temperature. The error for CO_L vibrational frequencies is within ± 3 cm⁻¹.

2.3.4 Effects of co-adsorbed H₂O on Methanol Dehydrogenation

Methanol adsorption experiments were also conducted following exposure of Pt/γ-Al₂O₃ catalysts to 0.5 mbar of water vapor. The adsorption of H₂O resulted in an intensive, broad band within the 2570 – 3660 cm⁻¹ range due to stretching vibrations of hydrogen bonding OH groups, while the scissoring deformation mode of H₂O was observed as a medium band at 1646 cm⁻¹ (**Figure A5**). The spectrum of the hydrated catalyst was subtracted from presented spectra to isolate methanol-derived surface species. H₂O-derived

species, including physisorbed molecular H₂O within multilayers and surface hydroxyls resulting from dissociative chemisorption, are expected to desorb as the temperature is increased.

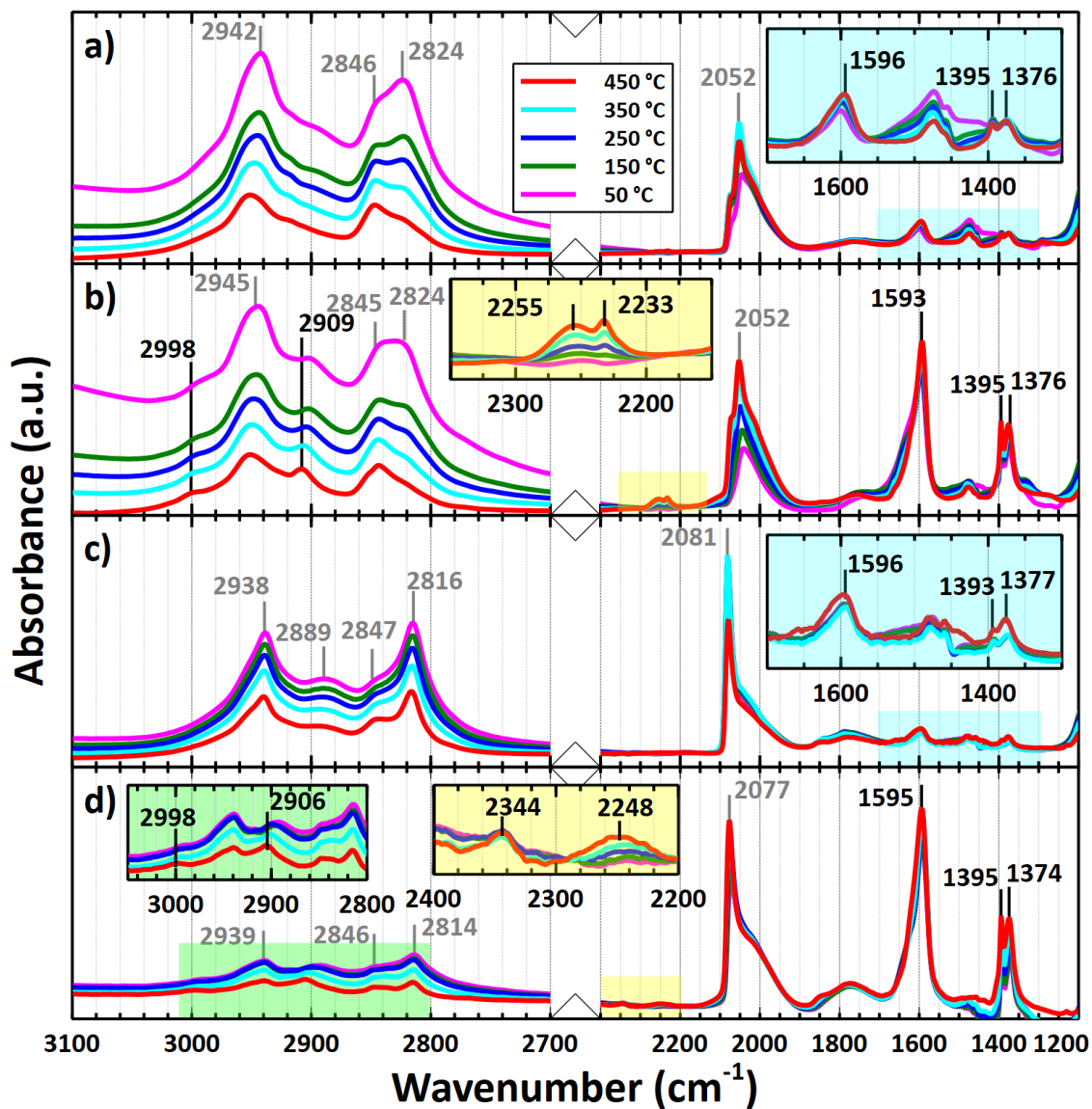


Figure 6. IR spectra of temperature-programmed methanol dehydrogenation on Pt/ γ -Al₂O₃ catalysts. **a)** methanol on R700, **b)** methanol/H₂O on R700, **c)** methanol on the commercial catalyst, and **d)** methanol/H₂O on the commercial catalyst. Bands with black frequencies are associated with the vibrational modes of a formate species while bands with gray frequencies were assigned to those of species previously identified on dry Pt/ γ -Al₂O₃.

The same bands in the 1900 – 2150 (CO_L) and 1700 – 1850 cm^{-1} (CO_B) regions emerged over hydrated $\text{Pt}/\gamma\text{-Al}_2\text{O}_3$ and dry $\text{Pt}/\gamma\text{-Al}_2\text{O}_3$ during the adsorption of methanol (**Figure 6**), demonstrating that methanol dehydrogenation was still achieved in the presence of pre-adsorbed water. However, for R700 and the commercial catalyst, a few key differences were noted. First, the relative magnitude of the CO_B band was larger. As a surface species, water is expected to donate electron density to the metal hence weakening the $\text{C}\equiv\text{O}$ bond (vide infra) enough to facilitate the conversion of some CO_L species to CO_B .^{32, 58} This effect was more pronounced on the commercial catalyst than R700, suggesting that it is easier for adsorbed CO to bind as a bridging species on larger Pt particles.

In addition, a strong band at 1593 – 1595 cm^{-1} was observed in the IR spectra of species on R700 and the commercial catalyst. This represents O-C-O asymmetric stretching mode of a formate species.⁵⁹ This is accompanied by additional bands at about 2900 – 2909, 1395, and 1374 – 1376 cm^{-1} representing the C-H stretching, symmetric O-C-O stretching, and O-C-H in plane bending modes of formates⁶⁰. The weak, broad feature centered at 2998 cm^{-1} is believed to arise from the combination of multiple -C-H and =C-H stretching modes in this species.⁶⁰ At 250 °C, a weak doublet appeared at 2200 – 2400 cm^{-1} and was identified as a $\nu_\text{as}(\text{C}=\text{O})$ mode of adsorbed carbon dioxide.⁶¹ This doublet continued to grow slightly with increasing temperature up to 450 °C. The spectra of methanol-derived surface species on moisturized catalysts with small Pt particles, R300 and R500 (**Figure A6**), showed only a weak asymmetric O-C-O stretching band at 1593 cm^{-1} as low as 150 °C. There was no evidence of adsorbed carbon dioxide on these samples.

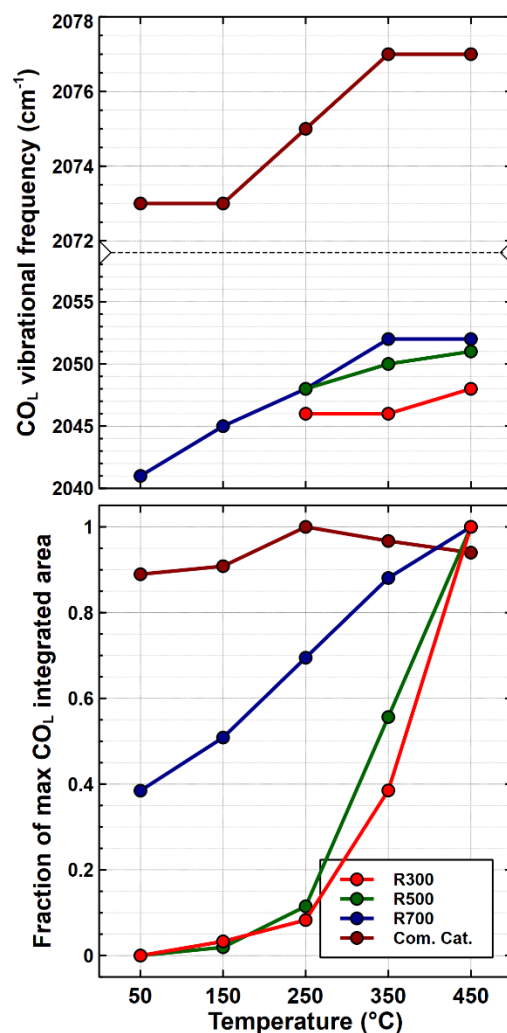


Figure 7. Position and fractional peak of the CO_L stretching peak after methanol adsorption on various hydrated Pt/ γ -Al₂O₃ catalysts. **a)** vibrational frequency and **b)** integrals of the CO_L stretching vibrational mode with increasing temperature. The error for CO_L vibrational frequencies is within ± 3 cm⁻¹.

The vibrational frequencies and integrals of the CO_L stretching band during methanol dehydrogenation on the Pt/ γ -Al₂O₃ catalysts (**Figure 7**) provided insight into the effects of water. As in the experiments without the presence of water, the frequencies increased with temperature. Frequencies were not obtained at 50 and 150 °C for R300 and R500 because there was no evidence of CO formation. By 450 °C, their CO_L frequencies were 2048 and 2051 cm⁻¹, respectively. Below 150 °C in HV, co-adsorbed water decreased

the frequencies of CO_L on larger Pt particles by 5 – 8 cm⁻¹, in agreement with previous results.⁶² In fact, this decrease was consistent amongst every synthesized Pt/ γ -Al₂O₃ sample below 250 °C. The frequencies lined up with those of dry experiments around 350 and 450 °C when much of the H₂O had desorbed.

In contrast to the lack of CO formation on R300 and R500 at 150 °C and below, the fractional integrals for R700 and the commercial catalyst at 50 °C were 38 and 89 %, respectively. The integral of CO peaks on R300 and R500 demonstrated an exponential conversion trend, reaching their maximum conversion at 450 °C when most of the pre-adsorbed H₂O had presumably desorbed. That of R700 was comparatively linear while that of the commercial catalyst was maximized at 250 °C and decreased as the temperature was further increased. While adsorbed CO is a likely source for production of the formate species, consumption of the intermediate on catalysts with large Pt particles did not seem to drastically change the frequency or integral trends.

2.3.5 *Rates of CO Formation*

The time-resolved intensities of CO_L and CO_B stretching bands on R500 and the commercial catalyst were studied in the presence of 0.5 mbar of methanol vapor at 150 °C (**Figure 8**). While these Pt particles possess a wide variety of different metal sites, time resolved CO formation can reveal where methanol dehydrogenation occurs preferentially and how quickly the coverage of different Pt particles reaches equilibrium.

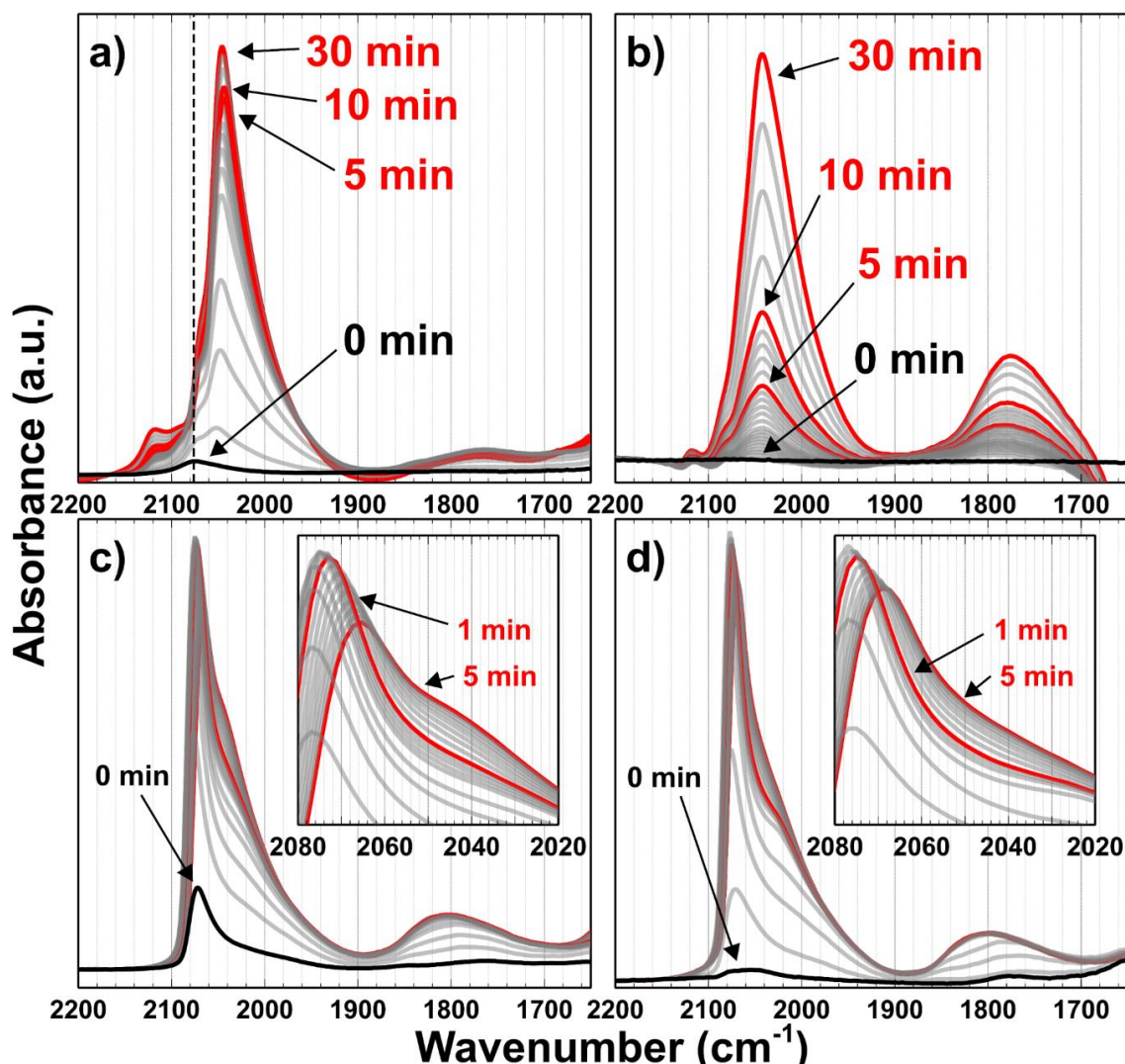


Figure 8. CO stretching bands during methanol dehydrogenation on **a)** R500, **b)** R500 pre-exposed to H₂O vapor, **c)** the commercial catalyst, and **d)** the commercial catalyst pre-exposed to H₂O vapor at 150 °C. Scans were taken as soon as the catalyst was exposed to methanol (black spectra), at time checkpoints once 0.5 mbar of methanol vapor was achieved (red spectra) and time intervals in between checkpoints (gray spectra).

The time for small Pt particles to reach equilibrium dehydrogenation of methanol, or saturation by CO, was about 30 minutes. The CO_L frequency started at 2076 cm⁻¹ and ended at 2047 cm⁻¹ after 30 min. This rate was very slow compared to that of large Pt particles on the commercial catalyst, which seemingly achieved saturation within the first

minute and showed an original CO_L band at 2072 cm⁻¹. In addition, the frequency of the CO_L band on this sample shifted to 2066 cm⁻¹ after 5 min, while the relative intensity of the low frequency shoulder increased slightly. This supports the kinetic preference of methanol to dehydrogenate on highly coordinated Pt sites over lowly coordinated ones.

For small Pt particles, the presence of water resulted in a remarkable amplification of the CO_B stretching mode. The growth of this band appeared to be synchronized with that of the CO_L with both saturating around the same time. In addition, water appeared to impede methanol dehydrogenation on smaller Pt particles given the differences in observed CO_L integrals at similar times, most notable during the first 10 min. After 5 min, the integral of the CO_L peak for small, dry Pt particles was about 81% of the value at saturation. For the small Pt particles pre-exposed to water, the corresponding area was only 20 % of its saturated value.

2.4 Discussion

2.4.1 Interpretation of Adsorbed CO Spectra

Vibrational modes of adsorbed CO strongly depend on the environment. The vibrational species of CO_L and CO_B at 2048-2080 and 1700-1850 cm⁻¹, respectively, are much lower than that of gaseous CO at 2143 cm⁻¹,⁶³ indicating strong interactions with Pt. The CO_L species is characterized primarily by strong dative σ -bonds in which electrons from the CO HOMO are donated to the adsorbing Pt atom, while the CO_B species involves a more extensive degree of π back bonding from the metal to the CO antibonding LUMO

(and can include two- and threefold coordinate sites on Pt terraces).^{29, 64-66} The vibrational frequency of CO on Pt depends on a combination of electronic (metal atom coordination, oxidation state)^{36, 51, 55, 67} and chemical effects (co-adsorbates, solvation).^{32, 58}

Adsorbed CO is notably sensitive to the coordination of the adsorbing metal atom. It is generally accepted that CO on Pt atoms of higher coordination exhibit higher frequencies and thus stronger C≡O bonds.³⁶ This accounts for the main area of the CO_L band centered around 2050 cm⁻¹. The large, low-frequency shoulder, extending as low as 1900 cm⁻¹, is unique to CO adsorbed to lowly coordinated metal sites anchored to Lewis acidic supports. In the specific case with Pt/γ-Al₂O₃, it is theorized that the bonding electrons of CO adsorbed near the metal-support interface interact with neighboring Lewis acid sites, thus weakening the CO bond and lowering the $\nu(\text{C}\equiv\text{O})$ frequency.⁵³ This assignment was confirmed by our recent computational study.⁴²

Methanol dehydrogenation resulted in a large $\nu(\text{C}\equiv\text{O})$ band at 2079 cm⁻¹ on large Pt particles (**Figure 4**). This strong band was likely related to the high frequency shoulder centered at 2071 – 2074 cm⁻¹ seen on the smaller Pt particles. This suggests that an adsorbed CO species of distinct characteristics forms more readily on larger Pt particles, and exhibits limited coverage on smaller particles. We associated this band with the stretching mode of adsorbed CO surrounded by adjacent CO species. When an agglomeration of CO species vibrate in-phase with each other, they engage in dipole-dipole coupling because the orbitals of neighboring CO species interact in a way which further polarizes and strengthens the C≡O bond, enlarges the band integral, and increases the stretching frequency.⁶⁸ These “CO islands” can more easily form on larger Pt particles that

possess larger terraces, hence the stronger 2079 cm^{-1} band seen during methanol dehydrogenation on the commercial catalyst.

The small high frequency shoulders seen above 2100 cm^{-1} on R300 and R500 are attributed to adsorbed CO on slightly oxidized Pt sites ($\text{Pt}^{\delta+}$) either from proximity to residual surface Cl (from the H_2PtCl_6 precursor) or isolation as single Pt atoms. After deliberately dosing R700, which contained no Cl according to XPS (**Table 1**), with 5 wt. % HCl, the high frequency shoulder appeared during methanol dehydrogenation (**Figure A4**). This suggests that some Pt sites were partially oxidized, leading to decreased π -back bonding to adsorbed CO, a stronger $\text{C}\equiv\text{O}$ bond, and a higher stretching frequency. We believe that the 30 cm^{-1} shift of the entire CO_L peak, also observed in a previous study,⁶⁹ was due to an electron withdrawing effect due to adsorbed Cl near Pt sites. Another contributing factor may be CO bonded to Pt single atoms as noted by other studies.^{55, 70} These atoms may possess decreased electron density due to direct electron exchange with the support.⁷⁰ The extent of π -back bonding to CO would be reduced, justifying the presence of a high frequency shoulder of the CO_L stretching band. However, the significance of the contribution of this latter species to the high frequency CO_L stretching band remains to be quantified.

2.4.2 Pt Particle Size Effects on Dehydrogenation Activity

The present IR spectra of adsorbed CO formed by methanol dehydrogenation give insight into the reactivity of active sites (**Figure 3**). The prominent $\text{C}\equiv\text{O}$ stretching modes for all catalysts with Pt particle sizes as small as 0.5 nm and as large as 7+ nm (**Table 1**) showed that methanol dehydrogenation may proceed on a variety of metal sites. However,

corroborating trends between Pt particle size and certain features of the CO_L band imply that highly coordinated Pt sites are preferred for dehydrogenation. For instance, larger CO_L band integrals (i.e., higher conversions) were observed on catalysts with larger Pt particles at lower temperatures (**Figure 5**). However, the differences in $\nu(\text{C}\equiv\text{O})$ integrals with respect to Pt particle size become less significant with increasing metal particle size. At 50 °C, a 132% difference was observed between R300 and R500 (average Pt particle sizes of 1.0 and 1.1, respectively), while only a 29% difference was noted between R700 and the commercial catalyst (average Pt particle sizes of 1.3 and 4.6 nm, respectively). This suggests that Pt particles larger than those in this study would perhaps dehydrogenate methanol more readily, but not to a significant extent.

2.4.3 *Inter-adsorbate Interactions*

The interactions between neighboring surface species, whether similar or different, has been shown to have a strong influence surface species involved in catalytic systems, such as CO on Pt(111) crystals.⁷¹⁻⁷² In general, the distribution of CO across the surface, and therefore the nature of adsorbed CO bands, is coverage-dependent. For instance, Krebs and Lüth observed an initial CO_L band centered at 2068 cm⁻¹ while probing extremely low CO coverages on Pt(111).⁵⁰ Upon achieving higher (but still low) coverages, the gradual diminishment of this band was proposed to be connected to the rise of a strong band of higher frequency (2079 – 2095 cm⁻¹), which remained unchanged when the CO exposure was increased further. Because this band appeared independently, as opposed to a steady shift of the initial band, it was assigned to the CO_L stretching mode of adsorbed CO involved in dipole-dipole coupling. The uniformity of the Pt(111) single crystal supports the interpretation that this was indeed a coverage effect rather than a kinetic effect due to

preferential CO formation of a specific type of site. The same coupling phenomenon seen on Pt single crystals can also occur on Pt nanoparticles.

While increasing CO coverage leads to observable dipole-dipole coupling, it also results in repulsion between species that are directly adjacent.⁷³⁻⁷⁴ Repulsion between adjacent CO species is strongest on Pt terrace sites where the repulsion energy between two adjacent CO species on neighboring Pt atoms (2.77 Å apart) is ~0.05 eV.⁷⁵ This results in a lower activation energy for desorption and even the reconstruction or division of large metal terraces and particles.⁷⁶⁻⁸⁰ This could explain the decreased CO_L band integral observed for R700 and the Pt/γ-Al₂O₃ commercial catalyst at higher temperatures (**Figure 4 and Figure 5**). Because the decrease in the 2079 cm⁻¹ band for the commercial catalyst was not matched to an observable increase in the band around 2050 cm⁻¹, we attribute the smaller CO_L integrals to desorption rather than migration of adsorbed CO to metal sites of lower coordination.

Time-resolved experiments can provide deeper insight into the most preferred metal sites for dehydrogenation and CO binding. When R500 was first exposed to methanol vapor, the only peak present in the ν(C≡O) region was located at 2076 cm⁻¹ which aligns with the primary CO_L band of the commercial Pt/γ-Al₂O₃ (**Figure 8**). At such a low coverage, this early band development matches that in previous studies,⁵⁰ yet appears to be distinct from the primary band observed in the 2046 – 2052 cm⁻¹ range at equilibrium. With this there are two possible interpretations. (1) The formation of CO_L starts on highly coordinated Pt sites. Once these sites are occupied, the band at 2047 cm⁻¹ becomes dominant shortly after, indicating that subsequently formed CO resides on Pt sites with lower coordination. The largest Pt particles seen on R500 were within the 1.5 – 2 nm, ~10%

of the size distribution (**Table 1**), which are still capable of establishing small Pt terraces and thus CO islands. (2) Following methanol dehydrogenation, adsorbed CO_L is initially clustered together with a high $\nu(\text{C}\equiv\text{O})$ frequency of 2076 cm⁻¹ (compared the primary 2046 cm⁻¹ frequency that dominates the spectrum shortly after) resulting in dipole-dipole coupling at low conversion and coverage. Due to the tilting of adsorbed CO on the undercoordinated sites of small Pt particles, we would expect the magnitude of dipole-dipole coupling to be much weaker and have little contribution to the 2076 cm⁻¹ shoulder. Since CO islands with pronounced dipole-dipole coupling form more easily on larger Pt terraces, it is again suggested that highly coordinated Pt sites are more active methanol dehydrogenation.

Fewer studies have focused on the specific inter-adsorbate forces between adsorbed CO and hydrogen, which is to be expected based on the 4:1 ratio of H*:CO* from complete dehydrogenation of methanol. Cheah et al. suggested that repulsion between adjacent CO* and H* is somewhat stronger than that of CO*-CO*. ⁸¹ The repulsion energy between CO* and H* on adjacent Pt sites (2.77 Å) can be ~0.11 eV on a Pt(111) surface, ⁸² compared to that of ~0.05 eV for CO*-CO* repulsion. ⁷⁵ On Pt/ γ -Al₂O₃, the two species are either uniformly distributed across the surface or segregated into their own islands. However, given the larger repulsion between CO and H than for CO and CO or H and H, a possible explanation is that the dehydrogenation of methanol on terrace sites is followed by the segregation of these species into their own separate islands. Given the initial 2075 cm⁻¹ band seen during early exposure of R500 to methanol vapor (**Figure 8**), we can expect the initial formation of CO islands to occur on higher coordinate Pt where dehydrogenation also takes place more readily. Concomitantly, surface hydrogen would be pushed outwards

towards the nanoparticle edges. There it would either remain bound or leave the metal surface by associative desorption on lowly coordinated Pt⁸³⁻⁸⁶ or reaction with adsorbed oxygen to form H₂O. To a small extent, hydrogen could spillover onto the γ -Al₂O₃ support, especially if the support contains defects or contaminants.⁸⁷⁻⁸⁹ Any of these phenomena would free up sites for methanol conversion and hence CO formation. As the Pt particles become saturated with CO, they will no longer be able to accommodate further surface species and dehydrogenation activity will slow dramatically. This stagnation can be alleviated by the consumption of adsorbed CO through either desorption, which occurs more readily on larger Pt particles as previously discussed, or the WGS reaction.^{42, 90}

2.4.4 *Effects of Co-adsorbed H₂O*

As a solvent for oxygenates and an essential reagent, water is the by far the most abundant component in APR reactors. Consequently, the influence of water on the evolution of relevant intermediate species can have a significant impact on dehydrogenation activity.⁴³ This may include promoting effects, such as the solvation of surface intermediates or transition states. On the contrary, competitive adsorption can block metal sites needed for the conversion of oxygenates.

Adsorption of water occurred on all Pt/ γ -Al₂O₃ samples as shown by a strong broad O-H stretching band at 3000 – 3500 cm⁻¹ and a medium H-O-H scissoring deformation band centered at 1646 cm⁻¹ (**Figure A5**). The Lewis acid sites of γ -Al₂O₃ have a particularly strong affinity to water.⁹¹ At increased temperatures, formation of a boehmite phase with decreased acidity is expected unless the alumina is stabilized.⁹¹⁻⁹⁶

With co-adsorbed water present, the initial rate of methanol dehydrogenation over R500 (**Figure 8b**) was reduced significantly. It took about 5 min for discernable, yet still weak, CO bands to appear while CO formation on the commercial catalyst seemed virtually unaffected (**Figure 8d**). This suggests that the presence of co-adsorbed water is detrimental to the dehydrogenation reaction on small Pt particles, or uncoordinated Pt sites. We believe this to be in part due to hindered adsorption of methanol to sites currently occupied by H₂O. It is known that H₂O has a higher binding energy on Pt sites with lower coordination.⁹⁷ We expect this to also hold true for the small Pt particles of R500.

As a ligand, water is expected to increase the electron density of nearby metal centers and chemical nature of adjacent CO.^{32, 58} This would improve the back bonding into the CO π^* LUMO, thus decreasing the $\nu(\text{C}\equiv\text{O})$ frequency. In addition, a decrease in the catalyst acidity due to the partial hydration of $\gamma\text{-Al}_2\text{O}_3$ into boehmite might decrease the Fermi level of supported Pt atoms.⁹⁸ This effect increases the availability of electrons near the d-band edge. These phenomena simultaneously improves the ability for Pt to back donate into the CO π^* molecular orbital, thus reducing the C \equiv O bond strength.⁹⁹ This is reflected by a red shift of the $\nu(\text{C}\equiv\text{O})$ band;³² more so on R700 and the commercial catalyst which demonstrated methanol conversion at low temperatures with (2045 and 2073 cm⁻¹, respectively, at 150 °C) and without adsorbed water (2050 and 2081 cm⁻¹, respectively, at 150 °C). This effect, seen here under UHV conditions, is further amplified during APR using liquid flow as previously witnessed.^{29, 66} Solvation of adsorbed CO by H₂O is also possible because APR occurs in bulk water. Solvation involves intermolecular interactions between the surface species and the solvent that can ultimately affect the energetics of the reaction; oxidation via the water-gas shift reaction in this case. For adsorbed CO, multiple

studies claimed that the red shift of CO stretching bands is evidence for the solvation of adsorbed CO.^{32, 58, 100} This is most evident on small Pt particles (**Figure 8a,b**) where solvation by H₂O may also contribute to differences in the CO_B band integral on a hydrated catalyst surface. The CO_B frequency range was about 1730 – 1880 and 1700 – 1850 cm⁻¹ for dry and hydrated R500, respectively. We suspect a combination of both electronic and chemical effects cause these changes in the CO bands.

While the H₂O-induced promotion of CO_B, the active intermediate in the WGS reaction, was evident only on small Pt particles, we speculate that this would not outweigh the consequences of decreased dehydrogenation rates and that larger Pt particles may still prove to be more active for the overall APR reaction.

2.5 Conclusion

Renewable hydrogen production via aqueous phase reforming (APR) is initiated by alcohol dehydrogenation of cellulosic biomass-derived oxygenates. The catalysis fundamentals behind this reaction are isolated by observing methanol conversion on Pt/ γ -Al₂O₃ using infrared spectroscopy under high vacuum with and without co-adsorbed H₂O. Evolution of the resulting CO stretching bands, linear CO (CO_L) at 1920 – 2140 cm⁻¹ and bridging CO (CO_B) at 1750 – 1800 cm⁻¹, are deconvoluted to determine the preferred surface environment for high dehydrogenation activity. The kinetic experiments in which large Pt particles achieved equilibrium conversion within a minute while small Pt particles required about 30 minutes suggest that terrace sites are more active for complete dehydrogenation of methanol than undercoordinated sites. Larger $\nu(\text{C}\equiv\text{O})$ bands were also

observed for the catalyst with larger Pt particles as low as 50 °C in temperature-programmed experiments. Even on smaller Pt particles, methanol appears to dehydrogenate on the metal sites of highest coordination first. The presence of water amplifies the presence of CO_B but impedes the rate of methanol dehydrogenation on small Pt particles below 250 °C perhaps due to strongly bound water on lowly coordinated Pt, especially near the metal/support interface. Continuing efforts in studying the catalysis fundamentals of aqueous phase reforming will permit improved reaction efficiency and acquisition of renewable hydrogen.

CHAPTER 3. SURFACE CHEMISTRY OF DI/KETONES ON LEWIS ACIDIC γ - Al_2O_3

3.1 Introduction

Ketones are an important class of organic reactants that are essential to the chemical industry. They serve as important precursors for the manufacturing of synthetic polymers,¹⁰¹⁻¹⁰² enantiopure alcohols,¹⁰³ imines/amines,¹⁰⁴ and more. Diketones have also been utilized to synthesize specific compounds with high regio, diastereo, and enantioselectivity.¹⁰⁵⁻¹⁰⁶ While ketones and diketones may be acquired through a variety of sources and synthesis processes, it is likely that heterogeneous acid-base catalysts, typically metal oxides, are involved in some stage of their production or conversion. Therefore, it is important to understand the surface reactions of di/ketones on metal oxides and how the exact structure of the reactant affects reactivity and the final products.

Many metal oxide catalysts exhibit Lewis acidity, which allows these materials to chemically adsorb both gas- and liquid-phase reactants. Lewis acidic γ - Al_2O_3 in particular has been extensively studied in regards to its microstructure, surface behavior, and role as a catalyst or support.¹⁰⁷⁻¹⁰⁸ It is commonly utilized as a support for metal particles for a number of reactions in refineries and more sustainable chemical processes, including the Fischer-Tropsch process¹⁰⁹ and aqueous phase reforming.¹⁰ γ - Al_2O_3 is also used as an acid catalyst for some processes including alcohol dehydration and the Claus process for desulfurization of natural gas.¹¹⁰⁻¹¹¹ Because these reactions are strongly tied to the

petrochemical and biorefinery industries, of which many di/ketones originate, better understanding the interactions between di/ketones and γ -Al₂O₃ is essential.

Acetone is the simplest of ketones and is historically the most commonly used ketone for deciphering how molecules with carbonyl groups bind and react on different surfaces including those of metallic single crystals and various metal oxide materials.¹¹²⁻¹¹⁷ It is activated on Lewis acidic oxides, such as γ -Al₂O₃, to produce mesityl oxide through sequential enolization, aldol self-condensation and dehydration reactions.¹¹⁸ However, the reactivity trends and surface phenomena of ketones, and certainly diketones, of varying characteristics (size, types of functional groups, distance between functional groups, etc.) have yet to be rationalized in a single study.

Several types of spectroscopy have been employed to probe the adsorption and surface chemistry of ketones, particularly acetone, on surfaces. For instance, infrared (IR) spectroscopy was used by Hanson et al. to observe the Lewis acid-catalyzed transformation of adsorbed acetone into its enol tautomer on γ -Al₂O₃.¹¹⁹ It was also deduced in the same study that the enol species was responsible for initiating oligomerization with a nearby ketone species through a nucleophilic attack to form diacetone alcohol, an intermediate in mesityl oxide production. Qi et al. utilized nuclear magnetic resonance (NMR) spectroscopy to probe the activation of acetone on framework Sn-sites of Sn- β zeolites in the Meerwein-Ponndorf-Verley-Oppenauer reaction.¹²⁰ Furthermore, Senanayake et al. used both X-ray photoelectron spectroscopy (XPS) and near-edge X-ray adsorption fine structure spectroscopy (NEXAFS) to demonstrate the different binding orientations (η_1 or dioxypropylene) of acetone adsorbed on oxidized and reduced CeO₂ films.¹²¹ Conner et al. used attenuation total reflection IR spectroscopy and a direct comparison of vibrational

frequencies to show that acetylacetone binds to a TiO_2 surface very similarly to that of an acetylacetone ligand in a Ti-based coordination complex.¹²² These and many other studies have demonstrated the versatility and powerful nature of spectroscopy in revealing the surface chemistry of ketone functional groups on oxide surfaces. For theory-driven research, density functional theory has proven useful in calculating ketone adsorption parameters on metal oxide surfaces.¹²³ Some examples include adsorption energies and bond lengths of acetone on ZnO for sensing applications and activation energies for acetone and aldol condensation intermediates adsorbed to different sites on TiO_2 surfaces.¹²⁴⁻¹²⁵ While some di/ketone chemistry on oxide surfaces has been studied with experiments or theory, studies including both approaches are much less common.

In this study, IR spectroscopy was used to observe surface reactions on $\gamma\text{-Al}_2\text{O}_3$. Adsorbed species included acetone and more complex di/ketone species that vary based on size, presence of alcohol groups, and distance between C=O groups. Temperature-programmed reaction/desorption experiments under high vacuum tracked the progression of Lewis acid site-catalyzed reactions on dry $\gamma\text{-Al}_2\text{O}_3$ as well as the general binding strength of surface species up to 250 °C. Deconvolution of the $\nu(\text{C=O})/\nu(\text{C=C})$ region of the IR spectra ($\sim 1450 - 1800 \text{ cm}^{-1}$) revealed the vibrational modes of various intermediates and products formed from surface reactions. Configurations and relative binding energies for adsorbed diketones were acquired via density functional theory.

3.2 Materials and Methods

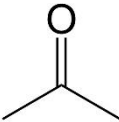
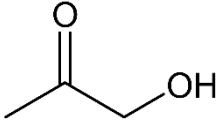
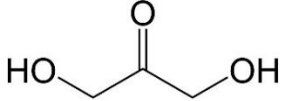
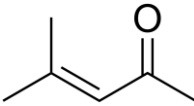
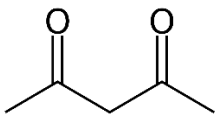
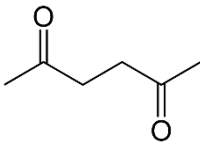
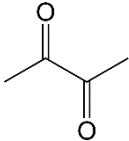
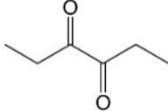
3.2.1 Experimental

Powdered γ -Al₂O₃ (Alfa Aesar 99.97%) was used as the adsorbent material. All the di/ketone reagents used in this study are listed in **Table 2** with Lewis structures and vendor information.

Adsorption of volatile di/ketones (every reagent listed in **Table 2** except DHA and 25HD) was performed under high vacuum (HV) with hydraulically pressed self-supporting wafers comprised of ~10 – 20 mg of γ -Al₂O₃ powder. The wafers were first activated under HV at 450 °C (10 °C/min) for 1 h to desorb residual water and other contaminants. IR spectra were acquired using a Thermo Scientific Nicolet 8700 FT-IR spectrometer that contained an MCT-A detector. Each spectrum collected was an average of 64 scans, each taken with an optical velocity of 1.8988 and a resolution of 1.928 cm⁻¹. After obtaining a spectrum for activated γ -Al₂O₃, the wafer was exposed to ~0.5 mbar of the di/ketone vapor at 50 °C for ~15 min. This would result in the formation of various IR bands attributed to both strongly chemisorbed surface species as well as weakly physisorbed species with liquid-like characteristics that make up multilayers. The chamber was then evacuated to achieve HV conditions prior to beginning the temperature-programmed desorption (TPD). This would cause a notable decrease in the intensity of bands associated with physisorbed species., suggesting that some desorption took place and that chemisorbed species dominated the surface. Herein, the wafer temperature was ramped (10 °C/min) to 100, 150, 200, and 250 °C. After each temperature was maintained for ~15 min, the wafer was allowed to cool naturally to 50 °C, so that all spectra in the TPD experiments were obtained

at the same temperature. The spectrum of activated γ -Al₂O₃ was subtracted from other spectra obtained throughout the TPD experiments to isolate absorbance bands that corresponded to surface species derived from di/ketone adsorption and reactions. All IR spectroscopy data was processed with Thermo Scientific Omnic software.

Table 2. Di/Ketone reagents adsorbed to γ -Al₂O₃.

| Reagent name | Lewis structure | Notes | Vendor information |
|------------------|---|--------------------------------------|---------------------------------------|
| Acetone |  | Simplest ketone | Alfa-Aesar, HPLC Grade 99.5+% |
| Hydroxyacetone |  | Ketone with 1 neighboring OH group | Alfa Aesar, 95% |
| Dihydroxyacetone |  | Ketone with 2 neighboring OH groups | Sigma-Aldrich (for synthesis) |
| Mesityl Oxide |  | Forms from acetone self condensation | Sigma-Aldrich, ≥97.0% (for synthesis) |
| 2,4-pentanedione |  | β-diketone | Sigma-Aldrich, ReagentPlus® ≥99% |
| 2,5-hexanedione |  | γ-diketone | Sigma-Aldrich, ≥98% |
| 2,3-butanedione |  | Small α-diketone | Sigma-Aldrich, 97% |
| 3,4-hexanedione |  | Large α-diketone | Sigma-Aldrich, ≥95% |

The adsorption of non-volatile di/ketones (DHA and 25HD) was also probed under HV. However, a different approach for adsorption was necessary given the insufficient vapor pressures. About 50 mg of γ -Al₂O₃ was impregnated with 2,5 hexanedione or a 1% (w/w) aqueous solution of dihydroxyacetone until the sample appeared saturated. The sample was then maintained under vacuum over night. The sample was ground into a powder that was pressed into a self-supporting wafer and positioned within the same HV IR cell. The wafer was allowed to sit in HV at ambient temperature for 2 h to remove physisorbed species prior to the aforementioned TPD experiment procedures, excluding the initial activation at 450 °C.

Features in the acquired IR spectra were deconvoluted using a custom Python code.¹²⁶ An exponential baseline was calculated while the band shape was assumed to exhibit a PseudoVoigt profile (i.e. a combination of 50 % Gaussian and 50 % Lorentzian characteristics).

3.2.2 Computational

The γ -Al₂O₃ surface was built by cleaving a (100) surface facet from the bulk structure of a γ -Al₂O₃ obtained from Digne,¹²⁷ which has a space group of P21/m and calculated lattice parameters of $a = 5.6$ Å, $b = 8.4$ Å and $c = 8.1$ Å and angles of $\alpha = \beta = \gamma = 90^\circ$. The simulation supercell (**Figure B1**) is a $2 \times 2 \times 2$ expansion of the unit cell with the surface in the c direction and is periodic with dimensions of $a = 16.2$ Å, $b = 16.8$ Å and $c = 35.5$ Å and $\alpha = \beta = \gamma = 90^\circ$. 25 Å of vacuum space are included between vertical images. Gas phase molecules were simulated in a box with dimensions $20 \times 20.1 \times 20.2$ Å.

DFT calculations were performed using the Vienna Ab initio Simulation Package (VASP)¹²⁸⁻¹³² using PAW pseudopotentials¹³³⁻¹³⁴ to an energy cutoff of 400 eV and the PBE exchange correlation functional.¹³⁵ D3 dispersion with Becke-Jonson damping¹³⁶⁻¹³⁷ was included, spin polarization was turned on, and dipole corrections were applied in the direction normal to the surface. The first Brillouin zones were sampled using $3 \times 3 \times 1$ Monkhorst–Pack Gamma-centered k-point meshes¹³⁸ in the case of alumina slab structures and $1 \times 1 \times 1$ k-point meshes in the case of gas molecules. Electronic structures were calculated self-consistently until the difference in energy between subsequent iterations was no larger than 10^{-6} eV. Geometries were considered converged when the magnitudes of the forces on all atoms fell below 0.03 eV/Å in geometry optimizations. Acetone was used as a common energy reference which also provided insight to the influence of sterics for diketone binding energies. The binding energies were calculated and referenced to adsorbed acetone according to **Equation (3)**:

$$\begin{aligned} E_{\text{Relative Binding}} = & E_{\text{Adsorbed molecule*}} - E_{\text{Gas phase molecule}} - \\ & E_{\text{Adsorbed acetone}} - E_{\text{Gas phase acetone}} \end{aligned} \quad (3)$$

Where $E_{\text{Adsorbed molecule*}}$ is the DFT-calculated energy of the adsorbed species, $E_{\text{Adsorbed acetone}}$ is the energy of adsorbed acetone, $E_{\text{Gas phase molecule}}$ is the energy of the gas phase molecule, and $E_{\text{Gas phase acetone}}$ is the energy of gas phase acetone. The different adsorbed molecule structures were generated from an initial configuration based on the gas phase molecule geometry. Adsorption into both tetrahedral and octahedral sites was tested. Different orientations of the adsorbate with respect to the surfaces were tested; specifically,

horizontal, tilted, and vertical molecule orientations were tested (**Figure B2**). The structures reported herein are those that give the lowest energies.

3.3 Results

The same batch of γ -Al₂O₃ used herein was characterized in a previous study, exhibiting a BET surface area of 63 m²/g and a Lewis acid site concentration of 72 μ mol/g that could retain adsorbed pyridine at 250 °C.¹³⁹ IR spectra were first acquired for low pressures of vapor phase di/ketones that exhibited sufficient volatility for a strong signal (**Figure B3**) and general vibrational mode assignments for distinct IR bands below 1800 cm⁻¹ in the IR spectra of the free molecules are listed in **Table B1**. This excludes dihydroxyacetone and 2,5 hexanedione. The full IR spectra of γ -Al₂O₃-adsorbed di/ketones are presented in **Figure B4**. Features representing various molecular vibrational modes were observed in the 1000 – 4000 cm⁻¹ range. This includes aliphatic C-H stretching, C=O stretching, CH_x deformation, and C-O stretching modes typically found within 2700 – 3000, 1550 – 1900, 1150 – 1500, and 1000 – 1300 cm⁻¹, respectively.³¹

Bands attributed to γ -Al₂O₃-adsorbed species generally exhibit increased broadness due to adsorption to Al³⁺ sites with a wide variety of coordination and acidity. Theoretically, overtone bands for ν (C=O) and ν (C=C) vibrational modes could be observed in the 3200 – 3500 cm⁻¹ region, exhibiting around twice the frequency of their respective fundamental bands. However, given the presence of a large, broad feature in the region attributed to hydrogen bonding and the significant diversity of surface species in most experiments, no apparent overtone bands attributed to particular surface species were

observed. Therefore, spectral deconvolution was conducted only for the $\sim 1500 - 1800 \text{ cm}^{-1}$ region. The IR spectrum of activated $\gamma\text{-Al}_2\text{O}_3$ contained small bands at 3765 and 3727 cm^{-1} associated with surface hydroxyl groups on tetrahedrally and octahedrally coordinated Al^{3+} sites, respectively.¹⁴⁰ These bands diminished rapidly during the adsorption of di/ketones. This suggested that di/ketones either displaced or perturbed (via hydrogen bonding) surface hydroxyls, the latter resulting in broadening and a shift to lower frequencies. However, this distinction could not be made based on the experimental evidence. The large, broad feature ($2750 - 3750 \text{ cm}^{-1}$) attributed to hydrogen bonding hydroxyl species was observed during the adsorption of each di/ketone, suggesting a notable extent of hydrogen bonding in each experiment due to surface and interadsorbate interactions between a wide variety of species. Thus, this region was not deconvoluted.

3.3.1 Mesityl Oxide and Acetone

Mesityl oxide adsorption on $\gamma\text{-Al}_2\text{O}_3$ (**Figure 9a**) gave rise to a strong feature within the $1500 - 1750 \text{ cm}^{-1}$ region. While the IR spectrum of the free vapor phase molecule (**Figure B3a**) contained two strong, distinct features centered at about 1704 and 1634 cm^{-1} for the $\nu(\text{C}=\text{O})$ and $\nu(\text{C}=\text{C})$ modes, respectively, the broadness in this region exhibited during adsorption suggests that there may be distinct surface species or perhaps the same species adsorbed to different sites. It was previously shown that $\nu(\text{C}=\text{O})$ and $\nu(\text{C}=\text{C})$ frequencies of mesityl oxide on zeolites are generally higher when adsorbed to Lewis acid sites as opposed to surface hydroxyl groups.¹⁴¹ As sites become decreasingly Lewis acidic, the shifts of both IR bands are expected to be nearly equivalent given the conjugation within the $\text{C}=\text{C}-\text{C}=\text{O}$ system.¹⁴² These conclusions also imply that the conjugated isomer is dominant on the $\gamma\text{-Al}_2\text{O}_3$ surface with little, if any, contributions from the non-conjugated

isomesityl isomer that ordinarily makes up about 10% of a solution.¹⁴³ Thus, the 1500 – 1750 cm^{-1} feature was deconvoluted into 4 main bands at 1670, 1625, 1599, 1570 representing $\nu(\text{C}=\text{O})$ on Lewis sites, $\nu(\text{C}=\text{O})$ on hydroxyl groups, $\nu(\text{C}=\text{C})$ on Lewis sites, and $\nu(\text{C}=\text{C})$ on hydroxyl groups (**Figure 9a**), respectively. The weaker high frequency contribution centered at 1700 cm^{-1} is likely due to a weakly physisorbed species.¹⁴¹ These, and all other assignments (**Table 3**), were made under the assumption that all adsorbed species retained the conjugated isomeric structure.

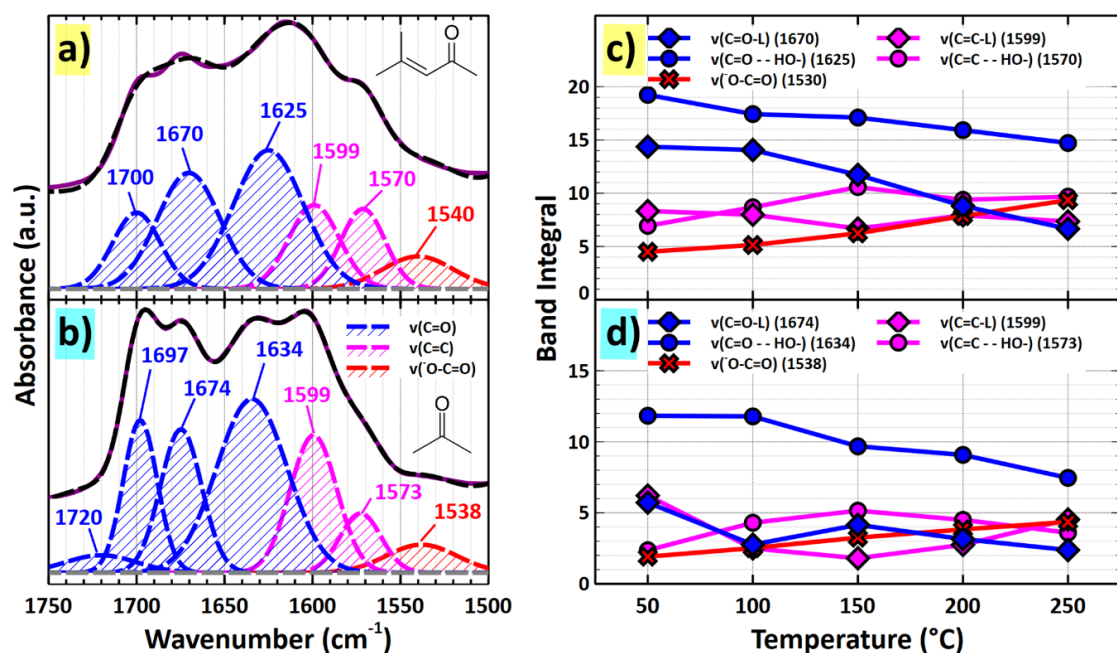
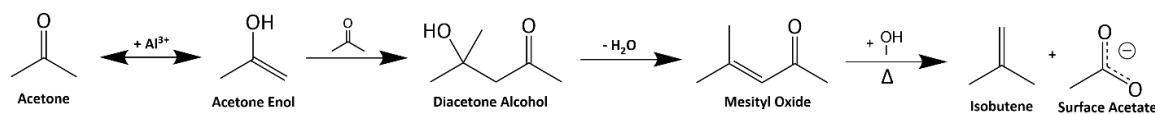


Figure 9. Deconvolution of the 1500 – 1750 cm^{-1} region of IR spectra for adsorbed **a)** mesityl oxide and **b)** acetone at 50 $^{\circ}\text{C}$ and **c,d)** corresponding temperature-dependent band integrals up to 250 $^{\circ}\text{C}$. Mesityl oxide and acetone-related data is highlighted in yellow and light blue, respectively.

The adsorption of acetone (**Figure 9b**) presents a very similar set of spectra as that of mesityl oxide. It is well known that strong Lewis acid sites, such as those on $\gamma\text{-Al}_2\text{O}_3$, facilitate the aldol condensation of acetone into diacetone alcohol.¹⁴⁴ This intermediate then undergoes dehydration to form mesityl oxide (**Scheme 1**). While a further extent of

aldol condensation to form phorone, isophorone, and mesitylene products is possible,¹⁴⁵ no IR bands affiliated with these species were observed. All general assignments for IR bands observed below 1800 cm⁻¹ during mesityl oxide and acetone adsorption are listed in **Table 3**.



Scheme 1. Acetone and mesityl oxide reactions on $\gamma\text{-Al}_2\text{O}_3$ up to 250 °C under HV.

The region of 1500 – 1750 cm⁻¹ was deconvoluted to acquire individual IR bands for $\nu(\text{C}=\text{O})$ and $\nu(\text{C}=\text{C})$ modes (**Figure 9a,b**). Bands associated with physisorbed mesityl oxide (1700 cm⁻¹) and acetone (1720 and 1697 cm⁻¹) were present at 50 °C but decreased in intensity with increasing temperature. When comparing the remainder of the deconvoluted region, individual bands associated with adsorbed mesityl oxide share similar frequencies to those observed during acetone adsorption. This may suggest that $\gamma\text{-Al}_2\text{O}_3$ converts a significant fraction of adsorbed acetone into mesityl oxide even at a temperature as low as 50 °C. Because no IR bands associated with the acetone enol tautomer nor the diacetone alcohol intermediate were detected, it also implies that the reaction occurs faster than the accumulation of the IR spectra. Results from an additional 10 min kinetics experiment corroborated this theory (**Figure B5**). The exposure of $\gamma\text{-Al}_2\text{O}_3$ to acetone vapor instantaneously resulted in a large band at 1700 cm⁻¹ which grew for 30 s. At this point, the band began displaying a severe decrease in intensity up to 10 min at which the system was evacuated. Bands associated with adsorbed mesityl oxide concomitantly grew and became dominant. It is therefore suggested that the surface coverage on $\gamma\text{-Al}_2\text{O}_3$ is dominated by mesityl oxide even during acetone adsorption.

Table 3. IR band assignments for acetone and mesityl oxide adsorption on γ -Al₂O₃ under HV at 50 – 250 °C. Arrows depict frequency shifts at higher temperatures.

| General vibrational mode | Acetone Adsorption | | | | Mesityl Oxide Adsorption | | |
|--------------------------|--------------------|---------------|---------|------------------------|--------------------------|---------|------------------------|
| | Acetone | Mesityl Oxide | Acetate | Notes | Mesityl Oxide | Acetate | Notes |
| $\nu(\text{C=O})$ | 1720 | | | Physisorbed acetone | | | |
| | 1697 → 1692 | | | Physisorbed acetone | 1700 | | Physisorbed MSO |
| | | 1675 → 1670 | | MSO on Lewis acid site | 1670 | | MSO on Lewis acid site |
| | | 1634 → 1625 | | H-bonded MSO | 1625 | | H-bonded MSO |
| $\nu(\text{C=C})$ | | 1599 → 1595 | | MSO on Lewis acid site | 1599 → 1596 | | MSO on Lewis acid site |
| | | 1573 | | H-bonded MSO | 1570 | | H-bonded MSO |
| $\nu(\text{O-C=O})$ | | 1538 | 1538 | MSO-derived acetate | | 1540 | MSO-derived acetate |
| $\delta(\text{CH})$ | | 1477 | 1477 | | | 1475 | |
| | | 1453 → 1457 | | | 1452 → 1455 | | |
| | | 1427 → 1424 | | | 1421 | | |
| | 1378 → 1387 | | | | 1385 → 1388 | | |
| | 1363 → 1365 | | | | 1364 → 1366 | | |
| | | 1332 → 1335 | | | 1323 → 1331 | | |
| | | 1320 → 1310 | | | 1311 | | |
| $\pi(\text{CH})$ | | 1287 | | | 1284 → 1281 | | |
| | | 1264 | | | 1258 | | |
| | 1234 → 1229 | | | | 1230 → 1238 | | |
| | | 1200 | | | 1208 → 1214 | | |
| | | 1193 | | | 1191 | | |
| | 1171 | | | | | | |
| | | 1151 | | | 1147 | | |

Changes in band integrals within the 1500 – 1750 cm⁻¹ region after heating to different temperatures reflect the conversion of surface species (**Figure 9c,d**). For instance, as the temperature increased, the band integrals for $\nu(\text{C=O})$ modes appeared to decrease, while those of $\nu(\text{C=C})$ modes remained relatively constant. This could be associated with the growth of the small band at 1538 – 1540 cm⁻¹ during both mesityl oxide and acetone adsorption. We attribute this band to the $\nu(\text{O-C=O})$ mode of a surface acetate formed along with isobutene during the fragmentation of mesityl oxide (**Scheme 1**), typically initiated via a nucleophilic attack of the carbonyl carbon by the hydroxyl group of an adjacent

enol.¹⁴¹ We would expect any isobutene produced to desorb from the surface given low temperatures previously reported to be required to observe any notable adsorption in the IR spectrum.¹⁴⁶ Although small, the band grew somewhat in size as the temperature increased, signifying a higher extent of conversion.

3.3.2 *Hydroxyacetone*

Upon hydroxyacetone adsorption to γ -Al₂O₃, a dominant band emerged at 1718 cm⁻¹ and was assigned to the $\nu(\text{C}=\text{O})$ mode of the adsorbed species. This band was accompanied by a low frequency shoulder and a tailing feature that extended as low as 1500 cm⁻¹, which required deconvolution (**Figure 10a**) and integration of the bands (**Figure 10b**). The 1718 cm⁻¹ band remained dominant but steadily decreased with increasing temperature up to 250 °C, suggesting there may be desorption or a possible a surface reaction. The slight countering growth of bands at 1675, 1645, 1588, and 1531 cm⁻¹ implied that not only did a reaction occur, but there were multiple distinct products that likely exhibited alkene characteristics.

Hydroxyacetone tautomerization could in principle result in a combination of two different enol products.¹⁴⁷ The cleavage of a C-H bond on the hydroxyl or methyl carbons initializes formation of prop-1-ene-1,2 diol and prop-2-ene-1,2 diol, respectively.¹⁴⁸ These surface species will simply be referred to as enediols. The $\nu(\text{C}=\text{C})$ modes of the enediols were assigned to the 1675 and 1645 cm⁻¹ bands. Given their lack of intramolecular conjugation, they should accommodate the higher frequency $\nu(\text{C}=\text{C})$ bands. In addition, the 1,2 enediol should exhibit a higher $\nu(\text{C}=\text{C})$ frequency because it possesses two hydroxyl groups directly attached to the alkene group as opposed to only one on the 2,3

enediol.³¹ Therefore, the 1675 and 1645 cm^{-1} bands were assigned to the 1,2 and 2,3 enediols, respectively.

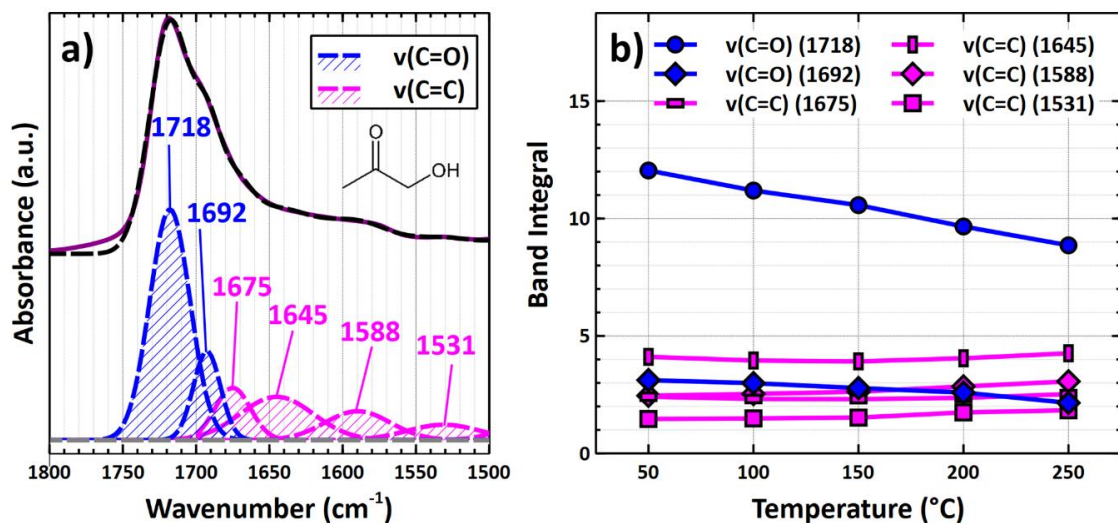
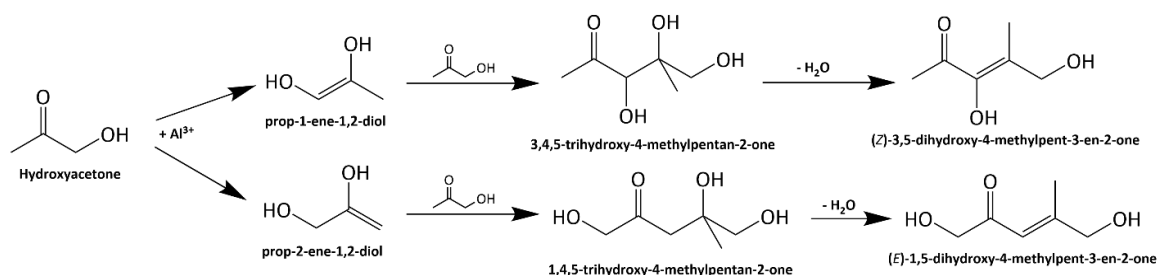


Figure 10. a) Deconvolution of the 1500 – 1800 cm^{-1} region of the IR spectrum of adsorbed hydroxyacetone on $\gamma\text{-Al}_2\text{O}_3$ at 50 °C. b) Corresponding temperature-dependent band integrals up to 250 °C.



Scheme 2. Hydroxyacetone reactions on $\gamma\text{-Al}_2\text{O}_3$ up to 250 °C under HV.

The remaining bands at 1692, 1588, and 1531 cm^{-1} were assigned to species formed from aldol condensation of adsorbed hydroxyacetone. We attributed the 1692 cm^{-1} band to a $\nu(\text{C=O})$ mode and because of its lower frequency (in comparison to 1718 cm^{-1}), it was likely associated with a conjugated surface species. The bands at 1588 and 1531 cm^{-1} were thus assigned to two different $\nu(\text{C=C})$ modes. With two different enediols on the $\gamma\text{-Al}_2\text{O}_3$,

there should be two different aldol condensation products formed upon reaction with molecular hydroxyacetone. The nucleophilic attack of the carbonyl should produce a dimeric intermediate that is dehydrated to form the final conjugated product (**Scheme 2**). Therefore, conversion of the 1,2 and 2,3 enediols should produce 3,5 dihydroxy-4-methylpent-3-en-2-one (35DH) and 1,5 dihydroxy-4-methylpent-3-en-2-one (15DH), respectively. There were likely two $\nu(\text{C}=\text{C})$ bands given that the hydroxyl groups are located on different carbon atoms. Similar to the enediols, we suspect the 35DH product will exhibit a higher $\nu(\text{C}=\text{C})$ frequency since both hydroxyl groups are directly bonded to the alkene group. As a result, we assigned the 1588 and 1531 cm^{-1} bands to the 35DH and 15DH condensation products, respectively.

Table 4. IR band assignments for hydroxyacetone adsorption on $\gamma\text{-Al}_2\text{O}_3$ under HV at 50 – 250 °C. Arrows depict frequency shifts at higher temperatures.

| General vibrational mode | Hydroxyacetone | 1,2 enediol | 2,3 enediol | 3,5 dihydroxy condensation product | 1,5 dihydroxy condensation product | Notes |
|--------------------------|----------------|-------------|-------------|------------------------------------|------------------------------------|---|
| $\nu(\text{C}=\text{O})$ | 1718 | | | | | |
| | | | | 1692 | | May also include 1,5 dihydroxy condensation product |
| $\nu(\text{C}=\text{C})$ | | 1675 | | | | |
| | | | 1645 | | | |
| | | | | 1588 | | |
| | | | | | 1531 | |
| $\delta(\text{CH})$ | | | | 1456 | | |
| | 1425 | | | | | |
| | | | | 1375 | | |
| | 1357 | | | | | |
| $\pi(\text{CH})$ | | | | 1333 | | |
| | 1270 → 1265 | | | | | |
| | | | | 1232 | | |
| | 1219 | | | | | |
| | 1194 | | | | | |
| | 1172 | | | | | |
| | 1155 | | | | | |

3.3.3 Dihydroxyacetone

Because the adsorption of dihydroxyacetone was performed ex-situ in the aqueous phase, contributions from γ -Al₂O₃ were not subtracted from the IR spectra (**Figure 11**). Although this made deconvolution of the mid IR region more difficult, notable features in the $\nu(\text{C}=\text{O})$ region were still identified. In addition, a separate TPD experiment with H₂O adsorbed to γ -Al₂O₃ was performed (**Figure B6**) to isolate the spectral contributions from small amounts of co-adsorbed H₂O. The main band of interest located within the 1630 – 1650 cm⁻¹ region was attributed the $\delta(\text{HOH})$ mode of molecular H₂O.

The large feature at 1728 cm⁻¹ was associated with the $\nu(\text{C}=\text{O})$ mode of adsorbed dihydroxyacetone. While this band remained dominant, it did exhibit a slight decrease in intensity up to 250 °C. This development was perhaps related to an equal enlargement of low frequency bands at 1630 and 1592 cm⁻¹ and the appearance of a new high-frequency shoulder at 1770 cm⁻¹, each of which suggest a surface reaction occurred. The bands at 1630 and 1592 cm⁻¹ were assigned to the $\nu(\text{C}=\text{O})$ modes of the aldehyde and ketone group, respectively, of adsorbed pyruvaldehyde. Dihydroxyacetone conversion into pyruvaldehyde has been previously demonstrated on Lewis acidic materials.¹⁴⁹⁻¹⁵⁰ This was confirmed by a separate TPD experiment in which pyruvaldehyde was adsorbed on γ -Al₂O₃ (**Figure B7**). Herein, the same bands at 1630 and 1592 cm⁻¹ were present and remained stable up to 250 °C. The high frequency shoulder that extended as high as ~1775 cm⁻¹ that accompanied these bands may explain the development of the small feature identified herein at 1770 cm⁻¹. This tail is believed to represent the partial strengthening of (C=O) bonds of adsorbed pyruvaldehyde species that are more distant from surface hydroxyls and adsorbed H₂O. On γ -Al₂O₃, dehydration of dihydroxyacetone into pyruvaldehyde appears

to be the dominant reaction (**Scheme 3**) with no observable evidence of enolization and condensation.

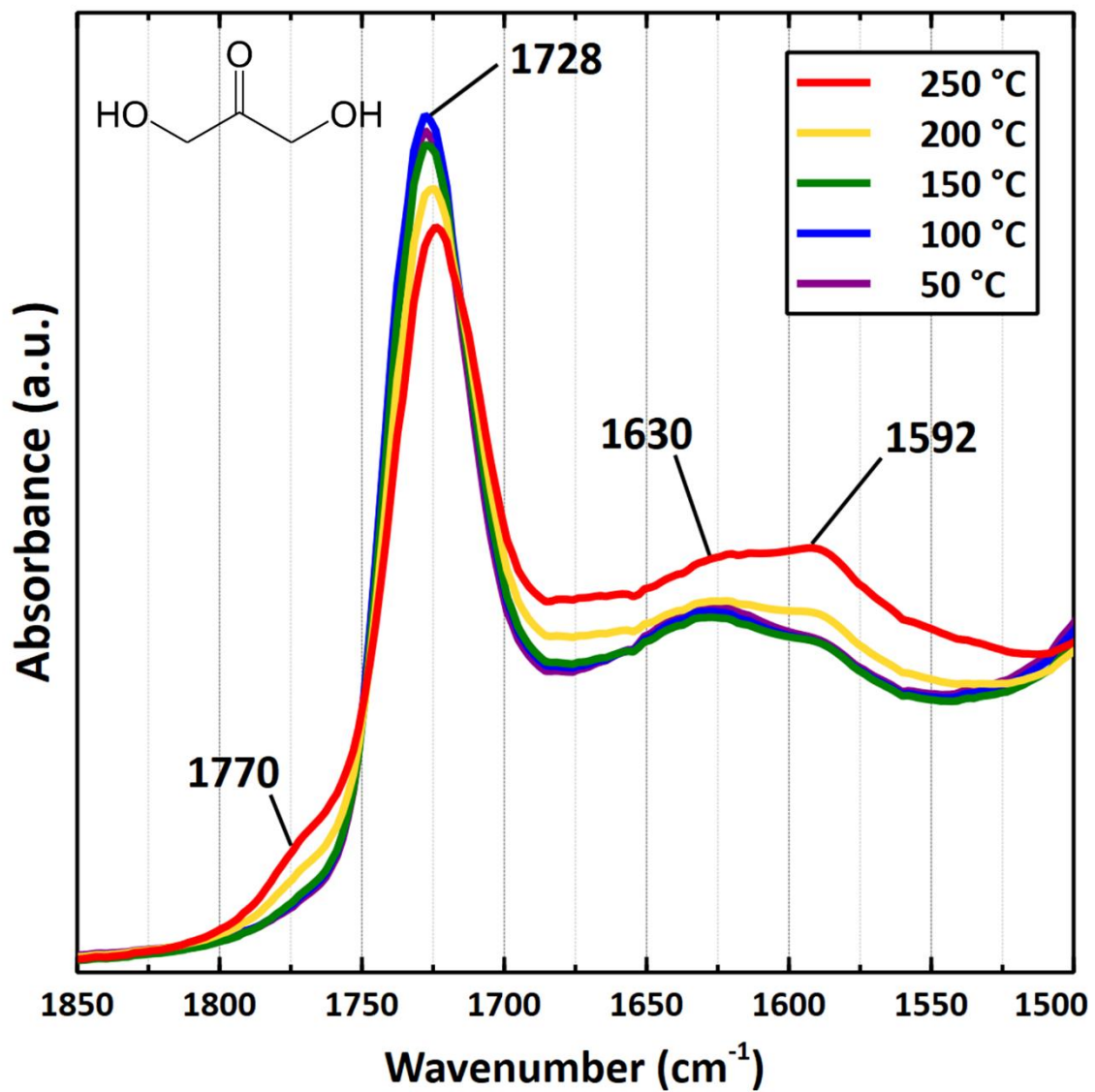
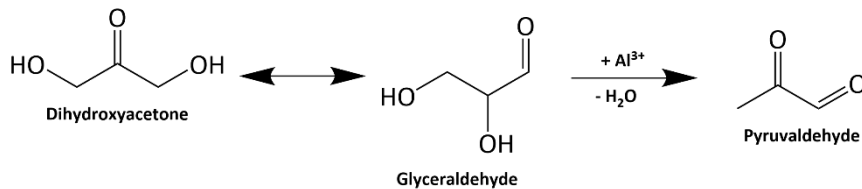


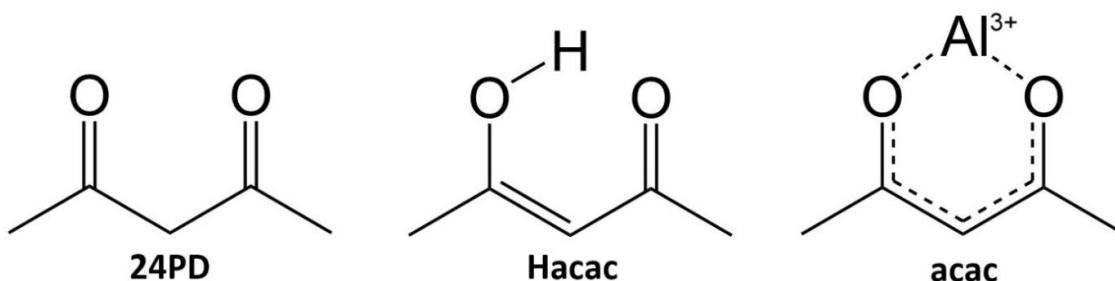
Figure 11. Infrared spectra ($\nu(\text{C}=\text{O})$ region) of surface species formed from dihydroxyacetone on $\gamma\text{-Al}_2\text{O}_3$ (prepared in the aqueous phase) during TPD experiments from 50 to 250 °C.



Scheme 3. Suggested reactions of dihydroxyacetone on γ -Al₂O₃.

3.3.4 2,4 Pentanedione

2,4 pentanedione, the enol tautomer, and the chelating ligand are illustrated in **Scheme 4** and are herein referred to as 24PD, Hacac, and acac, respectively, throughout interpretation of IR spectra during adsorption. Temprado et al. reported that the enol tautomer accounts for 81 mol% in a pure liquid phase at ambient temperature and contemplated a higher fraction in the pure vapor phase due to its greater volatility than that of the keto tautomer.¹⁵¹ This was reflected by the dominating $\nu(\text{C}=\text{O})$ band at 1637 cm⁻¹ in the vapor phase spectrum (**Figure B3d**) and must be strongly considered during the interpretation of the IR spectra of the adsorbed species.



Scheme 4. Nomenclature for species derived from 2,4 pentanedione.

The deconvoluted IR spectra of 24PD/Hacac (**Figure 12a**) showed various individual features within the region of 1500 – 1750 cm⁻¹, including dominant bands centered at 1597 and 1533 cm⁻¹. $\nu(\text{C}=\text{O})$ bands with lower frequencies within the 1500 –

1600 cm^{-1} are typically characteristic of carbonyl groups with bond orders of ~ 1.5 due to mesomerism and strong binding.³¹ In addition, the 1300 – 1750 cm^{-1} region remained largely unchanged up to 250 °C, suggesting the surface species were extremely stable. Therefore, we assigned the 1597, 1533, and several other bands below 1750 cm^{-1} (**Table 5**) to an $\text{Al}(\text{acac})_x$ surface species that dominated coverage on $\gamma\text{-Al}_2\text{O}_3$.¹⁵²⁻¹⁵⁴

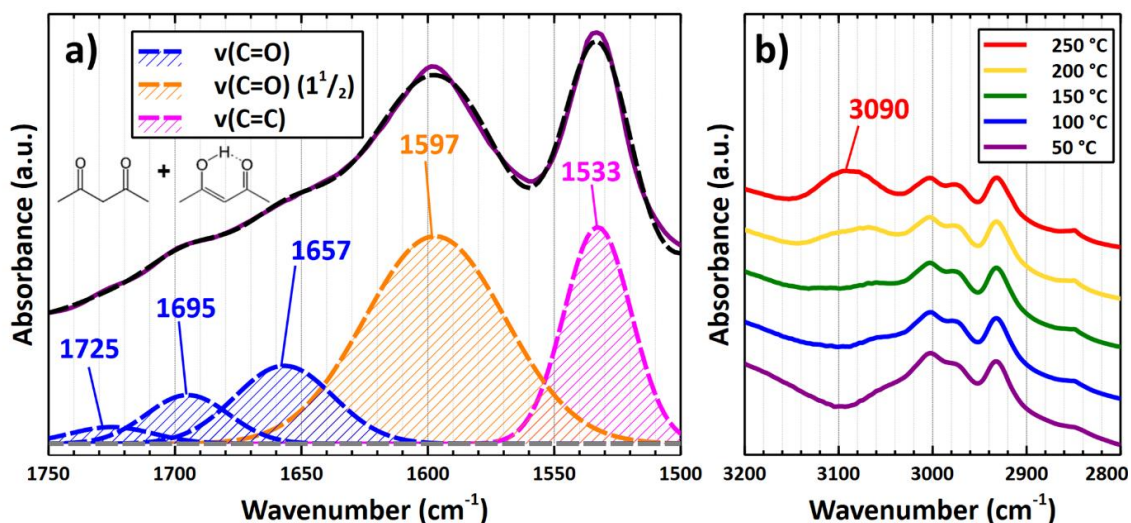


Figure 12. a) Deconvolution of the 1500 – 1750 cm^{-1} region of the IR spectrum of adsorbed 24PD/Hacac on $\gamma\text{-Al}_2\text{O}_3$ at 50 °C. b) Development of the $\nu(\text{CH})$ stretching region during the TPD experiment.

While they exhibited notable thermal stability, adsorbed Hacac/acac species were not entirely resistant to surface-catalyzed reactions. For instance, Kytökiivi et al. noticed the emergence of small IR bands at 1330 and 1055 cm^{-1} during the adsorption of 24PD/Hacac on $\gamma\text{-Al}_2\text{O}_3$ at 200 °C and claimed that these are affiliated with an acetate species resulting from molecular fragmentation, perhaps due to interactions with surface hydroxyls or co-adsorbed H_2O .¹⁵² These same bands, although small, were observed herein (1329 and 1055 cm^{-1}) at temperatures as low as 50 °C with slight growth up to 250 °C. The frequency of 1329 cm^{-1} is consistent with the $\nu(\text{O}=\text{C}-\text{O})$ mode of acetic acid.³¹ In this case,

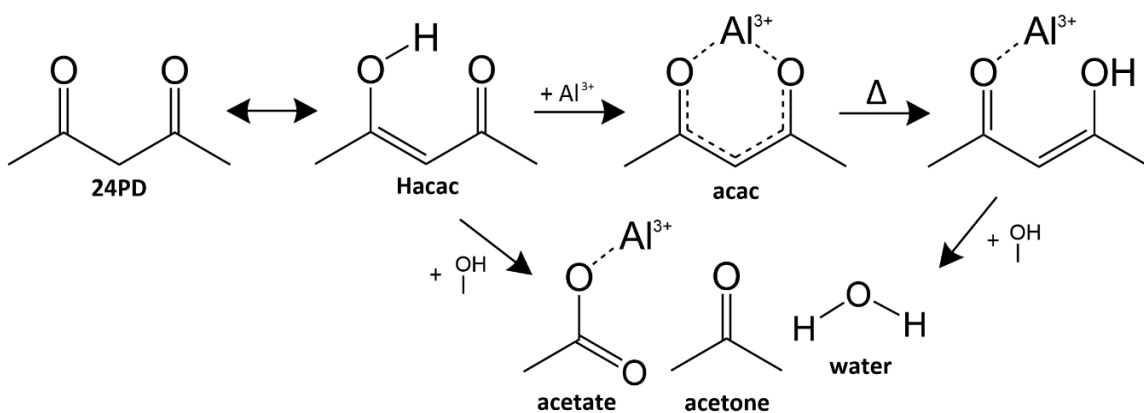
the formation of a surface acetate on γ -Al₂O₃ via Hacac/acac fragmentation should be concomitant with acetone production (**Scheme 5**).

Table 5. IR band assignments for 2,4 pentanedione adsorption on γ -Al₂O₃ under HV at 50 – 250 °C. Arrows depict frequency shifts at higher temperatures.

| General vibrational mode | 2,4 pentanedione or Hacac | Acac (as Al(acac) _x) | Acetic acid | Notes |
|--------------------------|---------------------------|----------------------------------|-------------|-----------------------------------|
| $\nu(\text{C=O})$ | 1725 | | | Could also be physisorbed acetone |
| | 1695 | | | Could also be physisorbed acetone |
| | 1657 | | | |
| $\nu(\text{C=O})$ | | 1597 | | Bond order of ~1.5 |
| $\nu(\text{C=C})$ | | 1533 | | |
| $\delta(\text{CH}_x)$ | | 1455 | | |
| | | 1396 | | |
| | | 1362 \rightarrow 1360 | | |
| $\nu(\text{O=C-O})$ | | | 1329 | |
| $\nu(\text{C-CH}_3)$ | | 1293 \rightarrow 1296 | | |
| | 1250 | | | |
| $\pi(\text{CH}_3)$ | | 1192 | | |
| $\nu(\text{C-O})$ | | | 1055 | |
| $\rho(\text{CH}_3)$ | | 1025 | | |

While little temperature-dependency was seen in the low frequency region, a notable observation was made in the $\nu(\text{CH})$ region between 2800 and 3200 cm⁻¹ (**Figure 12b**). From 50 to 150 °C, there were multiple bands within 2900 – 3050 cm⁻¹ that remained constant. A band at 3090 cm⁻¹ emerged at 200 °C and grew further at 250 °C. This band is assigned to the $\nu(\text{CH})$ mode of an olefinic surface species.³¹ While the free Hacac molecule is olefinic, the bidentate acac ligand of Al(acac)_x is mesomeric and therefore demonstrates less of this characteristic due to electron delocalization. Given the unchanged low frequency absorbance, we believe the emergence of this band at 3090 cm⁻¹ is due to the transition of a bidentate acac surface species to a monodentate Hacac species in which the

C=C-H bonds are much more stable (**Scheme 5**). This may be the first step in the thermal decomposition mechanism of $\text{Al}(\text{acac})_3$ and the creation of a surface species that perhaps may subsequently react with surface hydroxyl groups or another monodentate Hacac species to form acetates and 3,5-dimethylphenol, respectively; the latter product requiring higher temperatures ($> 300\text{ }^\circ\text{C}$) than those used in this study.¹⁵⁵⁻¹⁵⁶



Scheme 5. 24PD/Hacac reactions on $\gamma\text{-Al}_2\text{O}_3$ up to $250\text{ }^\circ\text{C}$ under HV.

3.3.5 2,3 Butanedione and 3,4 Hexanedione

α -Diketones such as 2,3 butanedione and 3,4 hexanedione contain two adjacent carbonyl groups. Up to $250\text{ }^\circ\text{C}$, the IR spectra of surface species from these molecules (**Figure B4f and Figure B4g, respectively**) shared similar features in the $1600 - 1800\text{ cm}^{-1}$ region representing both $\nu(\text{C=O})$ and $\nu(\text{C=C})$ modes. However, major changes in band integrals were seen for those within the IR spectra of adsorbed 2,3 butanedione, while those of adsorbed 3,4 hexanedione demonstrated remained almost unchanged in the $50 - 250\text{ }^\circ\text{C}$ temperature range. Band deconvolution was therefore necessary to isolate different species and rationalize the surface chemistry.

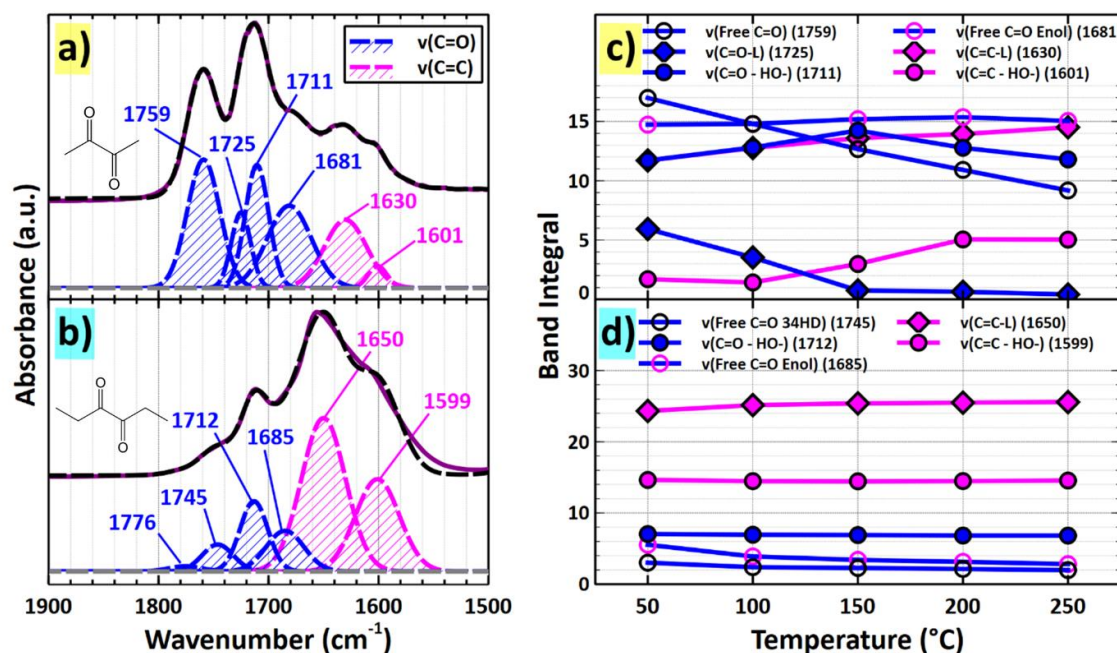


Figure 13. Deconvolution of the 1500 – 1800 cm^{-1} region of the IR spectrum of adsorbed **a)** 2,3 butanedione and **b)** 3,4 hexanedione on $\gamma\text{-Al}_2\text{O}_3$ at 50 $^{\circ}\text{C}$ and **c,d)** corresponding temperature-dependent band integrals up to 250 $^{\circ}\text{C}$. 2,3 Butanedione and 3,4 hexanedione- related data is highlighted in yellow and light blue, respectively.

For vapor-phase 2,3 butanedione, one band at 1729 cm^{-1} represented the asymmetric $\text{v}(\text{C}=\text{O})$ mode of the free molecule (**Figure B3e**).¹⁵⁷ While adsorbed on $\gamma\text{-Al}_2\text{O}_3$, there was a large, dominating band at $\sim 1712 \text{ cm}^{-1}$ with shoulders, while a slightly smaller higher frequency band was observed at 1759 cm^{-1} . When comparing these frequencies with those of the vapor-phase spectrum, the bands of the adsorbed species suggest that one carbonyl group was elongated and weakened, while the other was contracted and strengthened, respectively. This suggests that the band at 1759 cm^{-1} represents the $\text{v}(\text{C}=\text{O})$ mode of the free carbonyl group of 2,3 butanedione adsorbed in a monodentate orientation. The sharpness of this band, at least at lower temperatures, could corroborate this assignment, especially when compared directly to broader bands assigned to vibrational modes that more strongly interact with the $\gamma\text{-Al}_2\text{O}_3$ surface. A similar

conclusion was made in a study regarding diketone adsorption on SiO₂ submerged in a CCl₄ solution.¹⁵⁸ In addition, multiple individual bands appeared to contribute to the band at 1712 cm⁻¹, which suggests that the carbonyl was bound to various distinct surface sites. The deconvoluted bands at 1725 and 1711 cm⁻¹ (**Figure 13a**) are assigned to the $\nu(\text{C=O})$ modes of 2,3 butanedione bound to Lewis acid sites and surface hydroxyl groups, respectively. Similar conclusions were made with mesityl oxide, another stable ketone species, as shown above and in another study.¹⁴²

Individual bands were also observed within the 1600 – 1700 cm⁻¹ region, suggesting that a species with a C=C bond had formed. These individual features are assigned to an enol surface species derived from 2,3 butanedione on Lewis acid sites. Herein, a distinct band for the free carbonyl group was identified at 1681 cm⁻¹, a much lower frequency perhaps due to a conjugated interaction with the vinyl C=C bond. Unlike acetone, 2,3 butanedione did not immediately undergo enolization during adsorption at 50 °C, but rather the decrease in band integrals associated with the diketone species (**Figure 13c**) may suggest that the acid-catalyzed tautomerization reaction occurred more readily at higher temperatures. However, the band integrals of enol bands remained relatively constant during the TPD.

Similar deconvolution results and conclusions were made for 3,4 hexanedione, the larger α -diketone. The $\nu(\text{C=O})$ modes for the free carbonyl and the carbonyl bound to surface hydroxyls were centered at 1745 and 1712 cm⁻¹, respectively. The most noticeable differences between the spectra of adsorbed 3,4 hexanedione and those of 2,3 butanedione were the dominating band at 1650 cm⁻¹ (**Figure 13b**), the lack of temperature-dependency for the band integrals (**Figure 13d**), and the lack of changes in the 1480 – 1580 cm⁻¹ region

at higher temperatures. The dominating band at 1650 cm^{-1} was attributed to the $\nu(\text{C}=\text{C})$ mode of the enol species adsorbed to Lewis acid sites while the smaller band at 1685 cm^{-1} was associated with the free conjugated carbonyl of this species. This suggested that 3,4 hexanedione enolized much more readily compared to 2,3 butanedione.

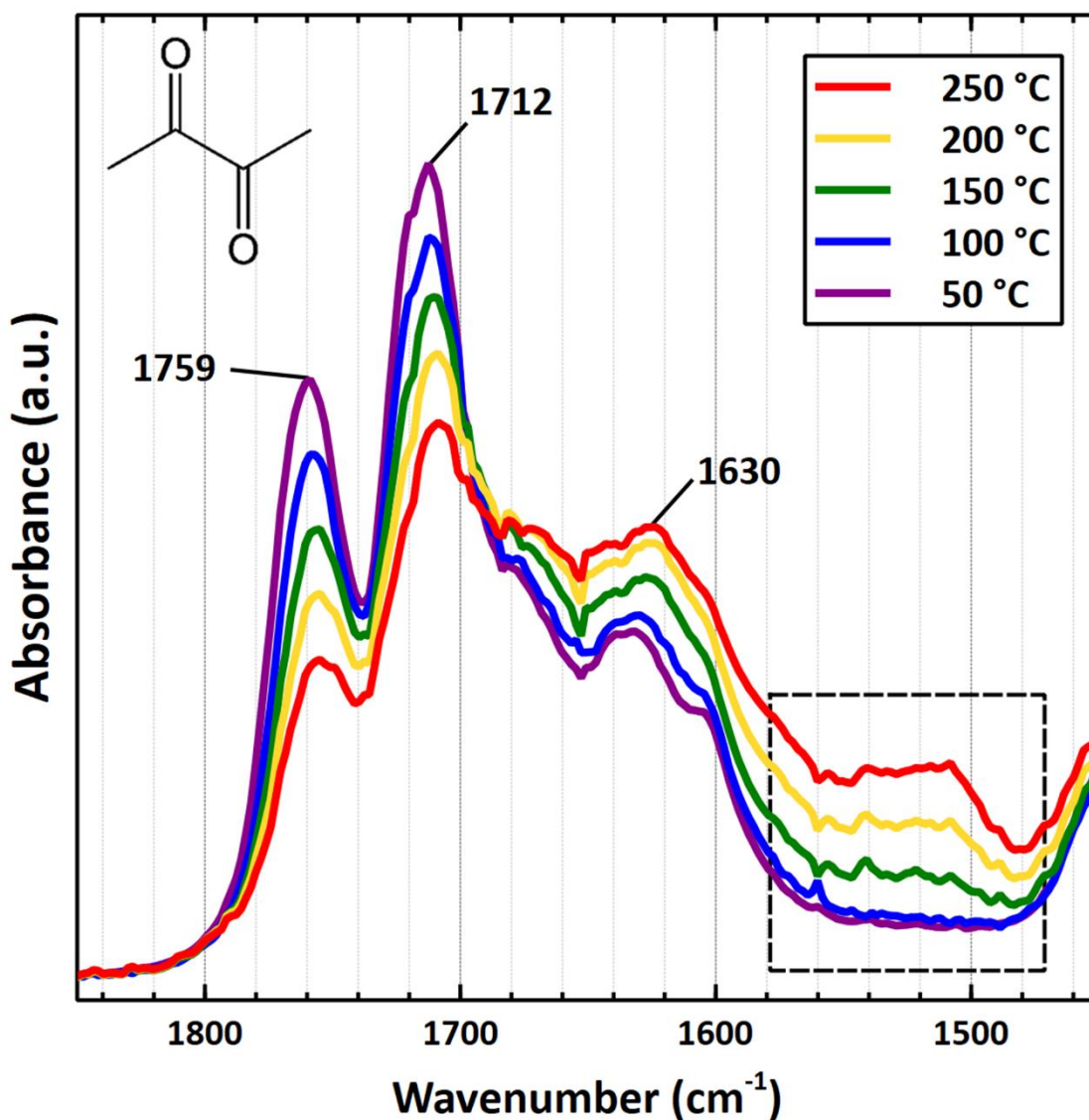
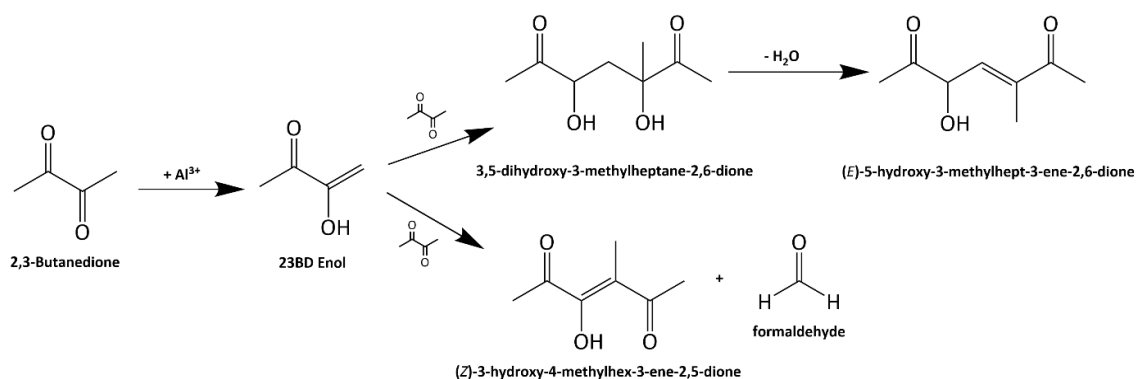


Figure 14. Mid-IR spectrum region of 2,3 butanedione adsorbed on $\gamma\text{-Al}_2\text{O}_3$. The temperature-dependent development of convoluted features associated with a conjugated product is outlined by the dashed box.

The nature of adsorbed 2,3 butanedione suggests that the species giving rise to the 1480 – 1580 cm^{-1} feature is formed in surface reactions involving C=O and C=C bonds. This broad feature grew as temperature was increased up to 250 °C (**Figure 14**) and likely contains a conjugated system. In addition, the $\nu(\text{C-H})$ region (**Figure B8**) included two bands at 2985 and 2937 cm^{-1} that are attributable to asymmetric and symmetric $\nu(\text{C-H})$ modes of adsorbed species, respectively. Aside from a slight decrease in intensity, these bands exhibited no change up to 250°C. There were also no new bands emerging in this region. These observations suggest that the conjugated products formed from 2,3 butanedione possess CH_x groups like those of the reagent. Thus, it is likely that either aldol condensation or carbonyl-olefin metathesis may have occurred (**Scheme 6**). Aldol condensation would perhaps involve a reaction between the 2,3 butanedione diketone and enol tautomers to form a 3,5-dihydroxy-3-methylheptane-2,6-dione intermediate. As with the previously discussed condensation reaction pathways, the intermediate herein may readily dehydrate to form a final 5-hydroxy-3-methylhept-3-ene-2,6-dione product. It may also be possible that the diketone and enol may interact via a carbonyl olefin exchange.¹⁵⁹ The corresponding chain propagation step would result in a 3-hydroxy-4-methylhex-3-ene-2,5-dione. In principle, this species could undergo further exchanges with adsorbed 2,3 butanedione to form elongated, conjugated polymers which could explain the broadness of the 1480—1580 cm^{-1} feature. There was no development in the 1480-1580 cm^{-1} region for adsorbed 3,4 hexanedione, implying that the respective enol does not subsequently react on $\gamma\text{-Al}_2\text{O}_3$.



Scheme 6. 2,3 Butanedione reactions on $\gamma\text{-Al}_2\text{O}_3$ up to 250 °C under HV.

Table 6. IR band assignments for 2,3 butanedione and 3,4 hexanedione adsorption on $\gamma\text{-Al}_2\text{O}_3$ under HV at 50 – 250 °C. Arrows depict frequency shifts at higher temperatures.

| General Vibrational Mode | 2,3 Butanedione Adsorption | | | 3,4 Hexanedione Adsorption | | |
|--------------------------|----------------------------|--------------|---------------------------------------|----------------------------|--------------|------------------------------|
| | 2,3 Butanedione | C=C Products | Notes | 3,4 Hexanedione | C=C Products | Notes |
| $\nu(\text{C}=\text{O})$ | | | | 1776 | | Physisorbed 34HD |
| | 1759 → 1755 | | Free C=O of bound 23BD | | | |
| | | | | 1745 | | Free C=O of bound 34HD |
| | 1725 → 1729 | | 23BD on Lewis Acid site | | | |
| | 1711 | | H-bonded 23BD | | 1712 | H-bonded 34HD |
| | | 1681 → 1676 | Free C=O of 23BD enol | | 1685 | Free C=O of 34HD Enol |
| $\nu(\text{C}=\text{C})$ | | | | | 1650 | 34HD Enol on Lewis Acid site |
| | | 1630 | 23BD enol on Lewis Acid site | | | |
| | | 1600 | H-bonded 23BD Enol | | 1599 | H-bonded 34HD Enol |
| | | 1480 – 1580 | Conjugated product (not deconvoluted) | | | |
| $\delta(\text{CH})$ | | 1445 | | | 1450 | |
| | 1425 → 1418 | | | | | |
| | 1405 | | | | 1408 | |
| | 1374 | | | | 1381 | |
| | 1357 | | | | 1358 | |

| | | | | | | |
|---------------|----------------|--|--|--|----------------|--|
| | | | | | 1358 | |
| | 1345 | | | | | |
| | | | | | 1336 | |
| | | | | | 1279 → 1282 | |
| | 1225 | | | | 1232 | |
| | 1198 | | | | 1192 | |
| v(C-O) | 1183 | | | | | |
| | 1157 → 1163 | | | | 1150 | |
| | 1135 | | | | 1128 | |
| | 1113 | | | | | |
| | 1083 | | | | | |

3.3.6 2,5 Hexanedione

The IR spectra of γ -Al₂O₃-adsorbed 2,5 hexanedione (**Figure 15**) showed notable absorbance within the 1500 – 1800 cm⁻¹ range. While the lack of temperature-dependent development may suggest that no reactions occurred with increasing temperature, the positions of the bands at 1632 and 1585 cm⁻¹ suggest that the γ -diketone was quite reactive on γ -Al₂O₃ even at 50 °C and was almost entirely converted into a new, conjugated product with a v(C=C) mode. The band at 1705 cm⁻¹, which decreased with increasing temperature, was assigned to the v(C=O) mode of small amounts of weakly adsorbed or unconverted 2,5 hexanedione. The diminishing of this band was attributed to further conversion or desorption.

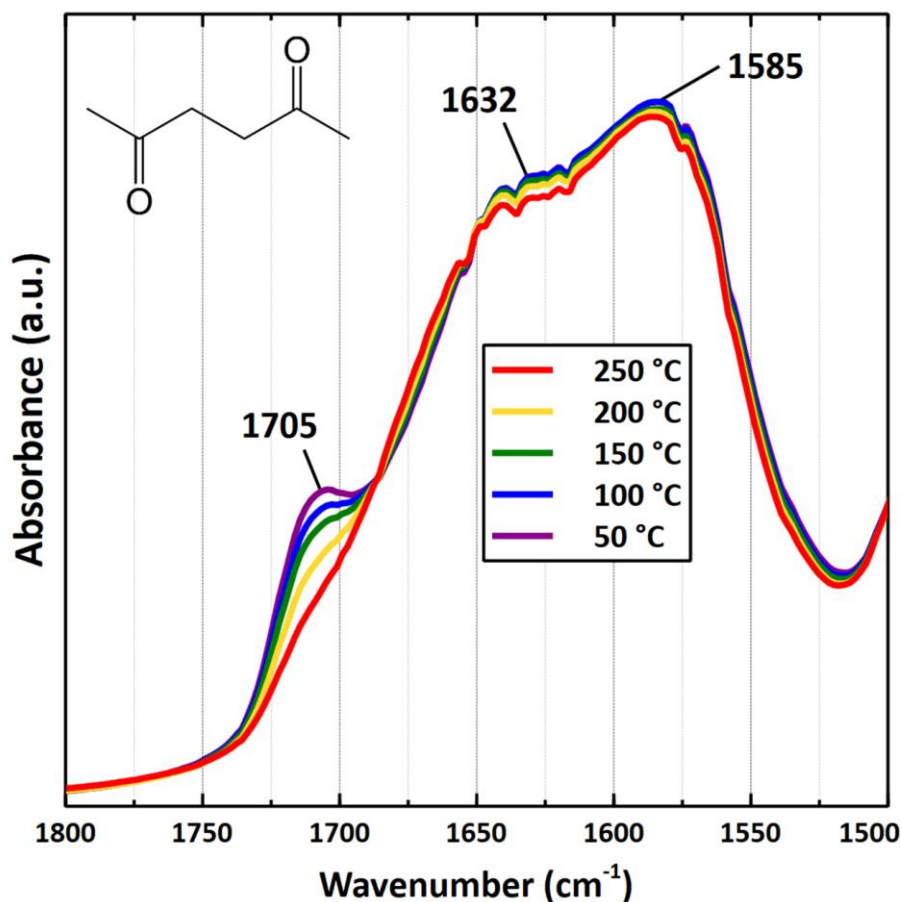
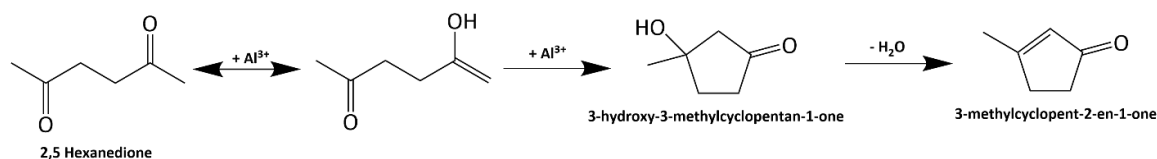


Figure 15. Infrared spectra ($\nu(\text{C}=\text{O})$ region) of 2,5 hexanedione adsorbed on $\gamma\text{-Al}_2\text{O}_3$ (prepared via ex-situ impregnation) during TPD experiments from 50 to 250 °C.

The presence of a conjugated product suggested that an aldol reaction occurred with the γ -diketone. However, given the insufficient vapor pressure of the diketone and immobility of the chemisorbed enol, it is highly improbable that reactions occurred between the diketone and enol tautomers as previously observed with the other di/ketones. Therefore, the spectra appear to reflect a product formed by an intramolecular aldol condensation in which the alkene group on one side of the surface enol performed a nucleophilic attack on the free carbonyl on the opposing side (**Scheme 7**). Following sequential dehydration, this would result in 3-methylcyclopent-2-en-1-one (3M2CP). To

corroborate this, a separate TPD experiment was performed with 3M2CP in which the reagent was impregnated ex-situ on γ -Al₂O₃ (**Figure B9**). Because the IR spectra are very similar throughout the whole 1000 – 2000 cm⁻¹ region, we concluded that 3M2CP is the most abundant surface species with aldol condensation as the dominating surface reaction.



Scheme 7. Reactions of 2,5 Hexanedione on γ -Al₂O₃.

3.3.7 Density Functional Theory

The lowest energy configurations for adsorbed diketone species provide insight into how these molecules bind to a γ -Al₂O₃ surface (**Figure 16**). Our results indicate that each of the diketones, regardless of the positioning of the carbonyl groups, bind to an Al^{3+} site via a carbonyl oxygen atom. The calculated $\text{Al}^{3+}\text{-O}=\text{C}$ angles (**Table B2**) are suggestive of σ -bonding. Other studies that focused on interactions between carbonyls and Lewis acids showed that σ -bonds form via donation of oxygen lone pairs.¹⁶⁰ Each diketone appears bound as a monodentate species, in which the second carbonyl vector is angled away from the surface. This corroborates the IR spectra interpretation of adsorbed 2,3 butanedione, the only diketone that seemingly avoided enolization at low temperatures, in which two different $\nu(\text{C}=\text{O})$ modes, one free and one bound, were identified. It is difficult to say the same for the other diketones given their propensity to convert almost completely as low as 50 °C.

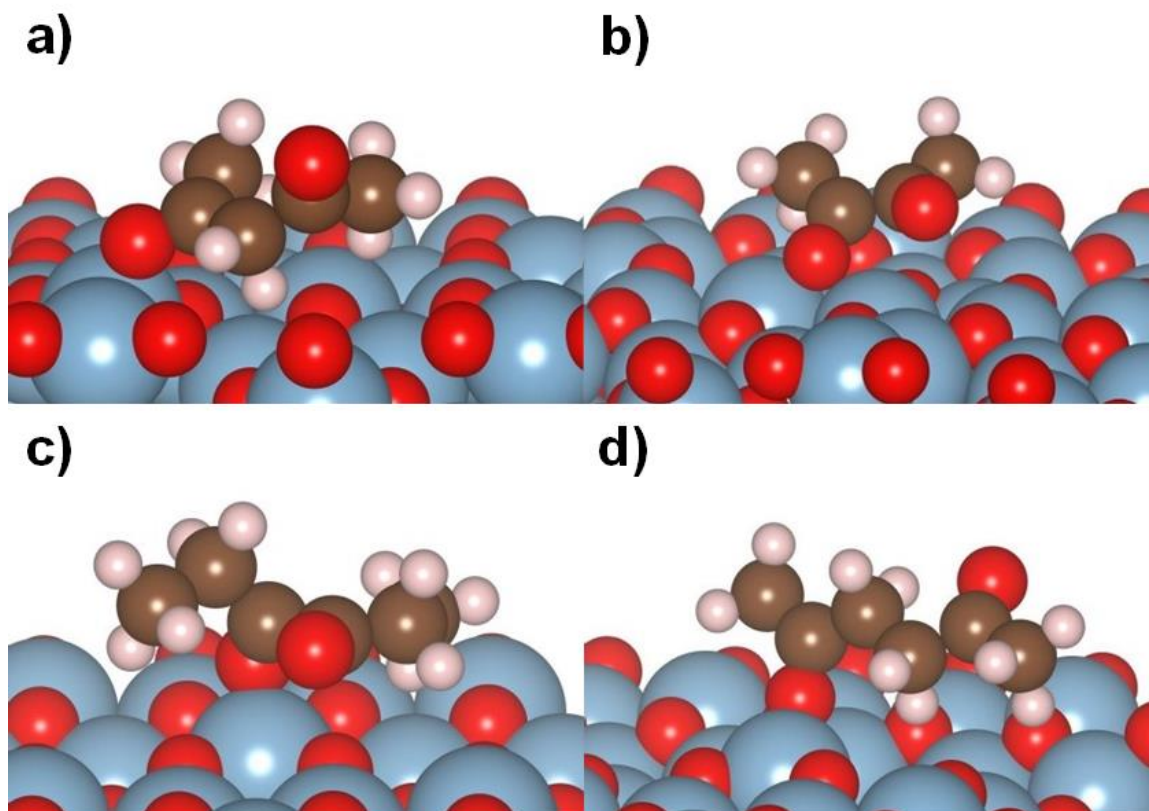


Figure 16. Lowest energy configurations of γ - Al_2O_3 -adsorbed **a)** 2,4 pentanedione, **b)** 2,3 butanedione, **c)** 3,4 hexanedione, **d)** 2,5 hexanedione. Configurations obtained by collaborators from Clemson University.

The lowest binding energies for diketones adsorbed to γ - Al_2O_3 were calculated with respect to that of adsorbed acetone (**Table 7**). Binding energies specific to either tetrahedrally or octahedrally coordinated Al^{3+} are presented in **Table B3**. In this convention negative numbers mean stronger binding energy than acetone and positive numbers mean weaker binding energy than acetone. Relative binding energies were lower for each diketone when adsorbed to tetrahedrally coordinated sites, with the exception of 2,3 butanedione. However, in the case of 2,3 butanedione the difference in binding energies for the different sites was only 0.07 eV, suggesting that binding in both tetrahedral and octahedral sites is possible. The energetic preference for adsorption to tetrahedrally

coordinated sites could be due to the enhanced Lewis acidity of these sites, compared to that of octahedral sites,¹⁶¹⁻¹⁶² increased exposure (reduced steric hinderance),¹⁶³ and electrostatic repulsion between surface oxygen and diketone alkyl chains. The α -diketones exhibited the highest relative binding energies of +0.44 and +0.26 eV for 2,3 butanedione and 3,4 hexanedione, respectively, suggesting that diketones bind less strongly to γ -Al₂O₃ when the carbonyls are directly adjacent. Adsorbed 2,5 hexanedione had a lower relative binding energy of -0.26 eV while adsorbed 2,4 pentanedione was even lower at -0.64 eV, suggesting the latter binds the strongest. However, the latter calculation does not account for the instantaneous mesomerism observed in the IR spectrum which is perhaps an essential step for stabilizing the surface species. While van der Waals interactions could explain some of the observed differences in binding energy, their contribution is expected to be < 0.1 eV for organic adsorbates on inorganic oxide surfaces.¹⁶⁴ Ultimately there was no clear trend between intramolecular carbonyl distance and binding energies of the adsorbed species. However, the 0.18 eV difference in binding energies between 2,3 butanedione and 3,4 hexanedione suggests the longer alkyl groups of the latter α -diketone are responsible for weakening the bond with γ -Al₂O₃. This is possibly due to the additional sterics of longer alkyl groups along with their greater repulsion from the oxide surface. The Al-O bond distances and Al-O=C bond angles (**Table B2**) were also obtained from the configurations but presented no apparent trends.

Table 7. DFT-calculated binding energies for γ -Al₂O₃-adsorbed diketones, relative to that of acetone. Calculations performed by collaborators from Clemson University.

| Adsorbate | E _{Relative Binding} (eV) |
|------------------|------------------------------------|
| Acetone | 0 |
| 2,4 Pentanedione | -0.64 |
| 2,3 Butanedione | 0.44 |

| | |
|-----------------|-------|
| 3,4 Hexanedione | 0.26 |
| 2,5 Hexanedione | -0.26 |

3.4 Discussion

The surface chemistry of molecules with multiple functional groups is determined by complex tradeoffs between possible surface interactions of different parts of the molecule.^{43, 165-166} The set of di/ketones in this study is chosen to isolate the influence of different structural features on its surface reactions on the Lewis acid sites of γ -Al₂O₃. While reaction pathways were proposed herein for adsorbed di/ketones, further analytical techniques would be required to assess the exact selectivity of the different products as well as potential by-products that were not observed in the IR spectra. The following sections will highlight the roles of hydroxyl groups, length of sorbate alkyl chains, the intramolecular carbonyl distance of diketones and speculations regarding solvent effects by co-adsorbed water.

Acetone is the ideal benchmark ketone reactant given its structural symmetry and simplicity and therefore served as an adequate basis for comparison when studying the adsorption of reactions of more complex di/ketones. Aldol condensation of acetone into mesityl has been studied extensively on Lewis acidic materials.^{118, 141-142, 167} It is also widely accepted that the alkene group of the enol tautomer performs a nucleophilic attack on the carbonyl of a nearby ketone.¹⁶⁸ However, there was little presence of acetone and no observable evidence of its enol tautomer on γ -Al₂O₃ as low as 50 °C. Rather, the deconvoluted IR spectra suggested that mesityl oxide was largely present and that aldol condensation occurs very readily with the simple ketone reagent.

3.4.1 *Steric and Electronic Effects of Hydroxyl Groups*

The presence of hydroxyl groups adds additional complexity to surface reactions of ketones. Upon adsorption, hydroxyacetone demonstrated more stability and resistance to the reaction. Increasing temperatures up to 250 °C seemed to initiate some extent of aldol condensation given by decreasing intensity of the 1718 cm⁻¹ hydroxyacetone $\nu(\text{C=O})$ band and emergence of 1692, 1588, and 1531 cm⁻¹ bands assigned to the $\nu(\text{C=O})$ of both 35DH and 15DH, $\nu(\text{C=C})$ of 35DH, and $\nu(\text{C=C})$ of 15DH, respectively. In acidic environments, hydroxyacetone enolization into the prop-1-ene-1,2 diol intermediate should be more prevalent given the greater inclination for C-H bond cleavage to occur on the hydroxyl carbon.¹⁴⁸ Therefore, the 35HD condensation product should be prevalent on the surface compared to the 15DH alternative as seen on another study regarding hydroxyacetone adsorption on $\gamma\text{-Al}_2\text{O}_3$. This is corroborated by a consistently larger $\nu(\text{C=C})$ band integral for the former species at all temperatures up to 250 °C. Nevertheless, hydroxyacetone remained the dominant surface species according to the strong 1718 cm⁻¹ $\nu(\text{C=O})$ band suggesting that alcohol groups adjacent to the carbonyl group hinder enolization.

As electron donors, alcohol groups should also prove obstructive for the condensation step. By increasing the overall electron density around the carbonyl group, the ketone should be consequentially shielded from a nucleophilic attack by an enol. While this was partially overcome at higher temperature, no aldol condensation was observed during the adsorption of dihydroxyacetone. This may be partially due to insufficient

enolization activity. The molecular enetriol has been observed to act more as an intermediate in the interconversion of dihydroxyacetone and glyceraldehyde; however only in basic (triethylamine) solutions.¹⁶⁹ However, relevant literature also suggests that other competing reactions may occur more readily on γ -Al₂O₃. For instance, it is known that Lewis acids can catalyze the dehydration of dihydroxyacetone (once isomerized into glyceraldehyde or via dimeric intermediate) into pyruvaldehyde,^{150, 170} which was observed as a surface species in the IR spectra herein. At temperatures of 50 – 250 °C, the carbonyl group of dihydroxyacetone seemed completely shielded, thus allowing the formation of pyruvic acid to dominate. At temperatures higher than 250 °C, greater conversion of adsorbed dihydroxyacetone into pyruvaldehyde is expected.

The IR spectra herein have suggest that acetone, hydroxyacetone, and dihydroxyacetone can each react on the Lewis acid sites of γ -Al₂O₃ at low temperatures. The contribution of aldol self-condensation reactions, however, becomes less as the carbonyl group becomes surrounded by adjacent hydroxyl groups due to electronic shielding effects, competing reactions, and stricter reaction conditions.

3.4.2 *Influence of Alkyl Group Length*

While potential mechanisms have been identified herein for the surface chemistry of 2,3 butanedione on γ -Al₂O₃, there remains the question of why the same aldol condensation or metathesis reactions do not appear to occur with 3,4 hexanedione. The dominant, unchanging band at 1650 cm⁻¹ suggests that the larger adsorbed α -diketone tautomerizes much more readily than the smaller one at a temperature as low as 50 °C. Yet, there were no absorbance bands within the 1480 – 1580 cm⁻¹ region of this spectrum to

suggest the formation of a conjugated product nor did they appear as the temperature is increased to 250 °C. There could be a couple of reasons for the lack of reactivity by adsorbed 3,4 hexanedione. Firstly, 3,4 hexanedione is expected to form a trisubstituted alkene group upon enolization, while 2,3 butanedione forms a vinylidene alkene group. The $\nu(\text{C}=\text{C})$ frequencies of these bonds are generally similar and difficult to distinguish in adsorption spectra.³¹ However, previous theoretical studies have illustrated trends in the free energy of hydrogenation to show that trisubstituted alkenes are generally more stable than vinylidene alkenes.¹⁷¹ This trend should still hold true even with the adjacent electron-withdrawing oxygen atom interacting with a Lewis acid site. Therefore, the trisubstituted alkene of the 3,4 hexanedione is expected to be less reactive towards aldol condensation or metathesis. Secondly, sterics may also play a critical role in the kinetic resistance of the larger α -diketone. Not only should less of the bulkier molecule adsorb to the same surface area, but the ethyl groups of 3,4 hexanedione, as opposed to the methyl groups of 2,3 butanedione, may sterically obstruct the nucleophilic attack on one surface enol by another. As a result of both alkene stability and ethyl group sterics, larger aliphatic α -diketones may readily enolize upon adsorption to $\gamma\text{-Al}_2\text{O}_3$ yet resist further steps of the aldol condensation reaction pathway.

3.4.3 Intramolecular interactions of carbonyl groups and their effect on the formation of surface species

The IR spectra of surface species from each diketone in this study demonstrated unique surface reactions on $\gamma\text{-Al}_2\text{O}_3$: intermolecular aldol condensation of 2,3 butanedione, enolization of 3,4 hexanedione, mesomerism of 2,4 pentanedione, and intramolecular aldol

condensation of 2,5 hexanedione. Given this diversity of surface phenomena, it is difficult to establish trends based on the spectroscopic evidence alone.

Low energy configurations in DFT models (**Figure 16**) revealed that the α -, β -, and γ -diketones bind to γ - Al_2O_3 via the oxygen atom of one carbonyl group. Regardless of intramolecular carbonyl distance, the other carbonyl points away from the surface and does not engage in a strong interaction. For diketones, it was shown that the two carbonyls exhibit intramolecular repulsion and that this interaction decreases significantly with increasing distance between the functional groups, although still present in γ -diketones.¹⁷²⁻
¹⁷³ As shown with various α -dicarbonyls, this intramolecular repulsion results in the trans-conformation being highly dominant over the cis-conformation for the free molecules.¹⁵⁷ For 2,3 butanedione, the only diketone to resist immediate reaction upon adsorption to γ - Al_2O_3 , both the DFT conformation and IR spectra suggested that with one carbonyl group immobilized and bound to the surface, the other will point away from the surface; not necessarily forming a perfect trans-conformation. In a similar study involving the adsorption of aliphatic diketones, Cross and Rochester interpreted their IR spectrum of SiO_2 -adsorbed 2,5 hexanedione as evidence of a bidentate surface species.¹⁵⁸ However, the adsorption was performed in CCl_4 solutions and a less acidic SiO_2 surface would perhaps exhibit less repulsion against the alkyl groups of adsorbed di/ketones.

3.4.4 *Impact of an Aqueous Phase*

The presence of large quantities of water, inherent to many biomass conversion processes, is expected to have an effect on the discussed surface reactions on γ - Al_2O_3 . Firstly, γ - Al_2O_3 transforms into a hydrated boehmite (AlOOH) phase with severely reduced

surface area and Lewis acidity under liquid water at 200 °C.⁹¹ In theory, this should decrease the di/ketone adsorption capacity of the catalyst support and impede enolization. Surface hydroxyls and adsorbed H₂O are very stable on Al₂O₃ surfaces at high temperatures and pressures and are unlikely to be displaced by most of the di/ketones studied herein, because they are less prone to forming multidentate surface species that could outcompete water for surface sites. Polyols, however, have shown potential in stabilizing γ -Al₂O₃ surfaces under hot, pressurized aqueous environments via formation of a protective adlayer.⁹¹ Studying the reactions observed herein under the aqueous phase and improving the hydrothermal stability of γ -Al₂O₃ with chelating, mesomeric diketones, such as 2,4 pentanedione and potentially other β -diketones, may be of interest for future studies.

3.5 Conclusion

Understanding the reactions and trends of adsorbed di/ketones on Lewis acidic materials such as γ -Al₂O₃ is essential for the chemical industry. Deconvolution and interpretation of IR bands of the $\nu(\text{C}=\text{O})$ and $\nu(\text{C}=\text{C})$ modes of adsorbed species revealed aldol condensation to be the most common surface reaction and as well as the effects of adjacent hydroxyl groups and the molecular size. Hydroxyl groups adjacent to the carbonyl group act as electron shields against nucleophilic attacks necessary for C-C bond formation. This was overcome with higher temperatures (up to 250 °C) for adsorbed hydroxyacetone, while isomerization dominated at all temperatures for adsorbed dihydroxyacetone. While 2,3 butanedione showed enolization and aldol condensation activity with increasing temperatures, the larger α -diketone, 3,4 hexanedione, formed a

stable enol likely due to the increased steric hinderance of larger alkyl groups as well as the greater thermodynamic stability of the trisubstituted C=C bond of the respective enol. Other unique surface phenomena were observed for 2,4 pentanedione (mesomerism) and 2,5 hexanedione (intramolecular aldol condensation), making it difficult to establish trends based on experimental data. DFT calculations suggested stable diketone surface species bind to γ -Al₂O₃ in a monodentate orientation with one carbonyl bound to the surface and one pointing away from the surface. Adsorbed species with relative binding energies on the lower side of this range (acetone and 2,5 hexanedione) should be expected to undergo the full aldol condensation mechanism more readily. This study has improved understanding of di/ketone surface chemistry on Lewis-acidic materials which may facilitate progress in various fields from prebiotic chemistry to sustainable industrial chemistry.

CHAPTER 4. PT CATALYST POISONING BY DI/KETONES

4.1 Introduction

The strive towards a more sustainable future is contingent on the industrialization of renewable hydrogen. While it remains essential for several major production processes including those of fertilizers, electronics, and fuel, the vast majority of hydrogen is still acquired from fossil-based sources.¹⁷⁴⁻¹⁷⁶ This pressing concern continues to incentivize researchers in the discovery and optimization of alternative methods for sustainable hydrogen production.

Biomass is an appealing source of hydrogen, and aqueous phase reforming (APR) is a heterogeneously catalyzed process that can extract this hydrogen from biomass-derived oxygenates dissolved in water.¹⁰ In principle, the conversion of $C_xH_{2x+2}O_x$ reagents (glycerol, sorbitol, etc.) can result in high yields of H_2 and CO_2 . This process is often conducted at temperatures of 180 – 250 °C, which is much lower than the temperatures required for pyrolysis and gasification while enough to facilitate the water-gas shift.¹⁷⁷ The gas products are easily separated from the bulk H_2O phase which can be recycled to reduce energy and material waste.

The transformation of oxygenates (polyols with C:O ratio of 1:1) in liquid H_2O was first studied by Dumesic et al. in 2002 while employing a Pt/Al_2O_3 catalyst.¹⁰ The authors contemplated a wide array of possible reactions and chemical intermediates given the acquired mixture of H_2 , CO_2 , and various alkanes. They proposed that the dehydrogenation → decarbonylation → water-gas shift reaction sequence is most efficient for maximizing

H₂ formation. Since then, numerous catalysts have been designed and tested in APR to improve product yields and tailor the selectivity between H₂ and alkanes.^{15, 178} Today, it is widely acknowledged that supported Pt catalysts are most suitable for H₂ production given the efficiency in C-H and C-C bond cleaving over this metal.¹⁷⁹⁻¹⁸⁰ This contrasts with other commonly utilized metals like Pd and Ni which also exhibit tendencies to break C-O bonds, thus resulting in alkane formation and decreased H₂ yields.¹⁸¹ However, a severe decrease in APR activity is commonly witnessed during the attempted conversion of larger oxygenates, even on Pt catalysts.^{10, 14, 29} For APR of polyols specifically, H₂ yields follow the general trend of CH₃OH > C₂H₆O₂ > C₃H₈O₃ > C₆H₁₄O₆. This phenomenon is believed to originate from the formation of byproduct surface species that ultimately deactivate the catalyst.

There are recent studies by Davis et al. which focused on polyol oxidation in aqueous environments and the underlying causes of catalyst deactivation over supported Pt catalysts.¹⁸²⁻¹⁸³ It was shown that acetone, mesityl oxide (resulting from aldol condensation of acetone), and 2,4-pentanedione severely decreased the oxidation activity of the catalysts depending on the system pH. Because exposure to 2,4-pentanediol did not result in any decreases in conversion rates, it was deduced that ketone-based species were responsible for deactivation of supported Pt catalysts through strong binding to the metal.

The mechanism for the APR of larger oxygenates is very complicated given the presence of numerous functional groups and possible side reactions. However, it is believed that the reaction pathway for H₂ and CO₂ production involves the decarbonylation of aldehyde intermediates formed from the dehydrogenation of primary (1°) alcohol groups.^{24, 27, 184} Alternatively, ketone species may be formed in APR by the non-selective

adsorption and dehydrogenation of secondary (2°) alcohol groups found on larger oxygenates starting with glycerol (**Figure 17a**). Ketones are expected to decarbonylate less readily given increased steric hinderance and the additional energy input required to cleave twice as many C-C bonds in comparison to aldehydes.¹⁸⁵⁻¹⁸⁷ The formation of these species is more likely to happen with larger oxygenates with higher $2^\circ:1^\circ$ alcohol group ratios.

Furthermore, larger polyol or sugar reagents could even form diketone species (**Figure 17b**). For oxygenates as sizable as sorbitol, these diketone species could potentially exhibit the additional complication of varying proximities between the carbonyl groups. They can be adjacent (α diketone) or split by one or two carbon atoms (β or γ diketones, respectively). While interactions of simple ketones, such as acetone, with metal surfaces have been extensively probed, similar studies with diketones are seldom conducted, although it is known that simultaneous surface interactions of multiple functional groups can play a significant role in catalytic conversion of oxygenates.⁴³

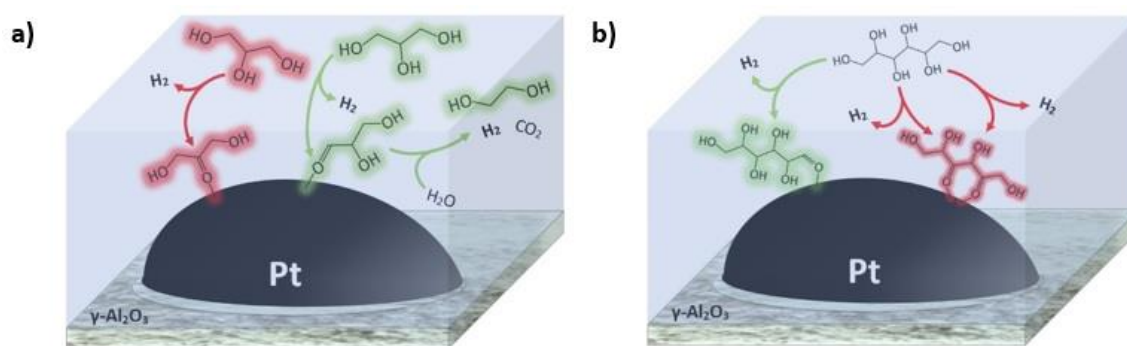


Figure 17. Illustrations of theorized catalyst poisons that may result from the non-selective adsorption and dehydrogenation of secondary alcohol groups on Pt/ γ -Al₂O₃: **a)** ketone intermediate from glycerol and **b)** β -diketone intermediate from sorbitol.

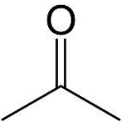
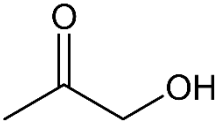
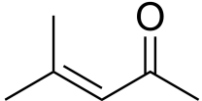
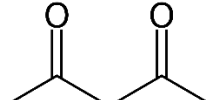
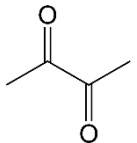
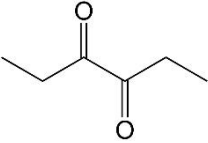
Herein, we use infrared (IR) spectroscopy and inelastic neutron scattering (INS) coupled with density-functional theory (DFT) to study the adsorption of ketones and diketones on Pt/ γ -Al₂O₃ surfaces. The extent of catalyst poisoning and the responsible surface species depend on the Pt particle size due to varying decarbonylation activity and site proximity to the γ -Al₂O₃ support which facilitated the formation of conjugated byproducts. While potential Pt poisoning surface species have been identified and understanding of di/ketone decarbonylation has been furthered, perspectives are provided for improving Pt catalyst durability and longevity in Apr applications.

4.2 Materials and Methods

4.2.1 Materials

A 1% Pt/ γ -Al₂O₃ catalyst with an average Pt particle size of 1.1 nm (σ = 0.4 nm), measured with transmission electron micrographs, was synthesized via wet impregnation with a H₂PtCl₆ (Sigma-Aldrich $\geq 99.9\%$ trace metal basis) precursor and γ -Al₂O₃ (Alfa Aesar 99.97%). This was intentionally made to possess smaller particles and is referred to as Pt_S/ γ -Al₂O₃. For comparison, a commercially obtained 5% Pt/ γ -Al₂O₃ catalyst (Sigma Aldrich #205974) with an average Pt particle size of ~ 4.6 nm (σ = 1.2 nm) was used. This sample is referred to as Pt_L/ γ -Al₂O₃ given its larger metal particle size. The BET surface areas of both catalysts along with the Lewis acidity of the γ -Al₂O₃ were previously calculated through N₂ and pyridine adsorption respectively.¹³⁹ Catalysts were reduced at 500 °C in 7% H₂/He (v/v) for 2 hr prior to experiments. A variety of organic reagents suspected of poisoning Pt were used herein (**Table 8**).

Table 8. Ketone and diketone reagents used.

| Reagent name | Lewis structure | Notes | Vendor information |
|------------------|---|--|---------------------------------------|
| Acetone |  | Smallest ketone | Alfa-Aesar, HPLC Grade 99.5+% |
| Hydroxyacetone |  | Ketone with neighboring OH group | Alfa Aesar, 95% |
| Mesityl Oxide |  | Forms from acetone self condensation, confirmed Pt poison ^α | Sigma-Aldrich, ≥97.0% (for synthesis) |
| 2,4-pentanedione |  | β-diketone, confirmed Pt poison ^α | Sigma-Aldrich, ReagentPlus® ≥99% |
| 2,3-butanedione |  | Small α-diketone | Sigma-Aldrich, 97% |
| 3,4-hexanedione |  | Large α-diketone | Sigma-Aldrich, ≥95% |

^αFrom ref. 182-183

4.2.2 Infrared spectroscopy

Catalyst powders were hydraulically pressed into self-supporting wafers that were positioned within a high vacuum ($< 4.5 \times 10^{-7}$ mbar) chamber with ZnSe windows. IR spectra were acquired using a Thermo Scientific Nicolet 8700 FT-IR spectrometer and analyzed with Thermo Scientific Omnic software. Each spectrum was an average of 64 scans collected with a resolution of 1.928 cm^{-1} , an optical velocity of 1.8988, and an aperture of 75. Wafers were activated under high vacuum at 450°C ($10^\circ\text{C}/\text{min}$) for 1 hr.

Each experiment consisted of two sequential temperature-programmed desorptions (TPD) under high vacuum (**Figure 18**). The activated catalyst wafers were first exposed to 0.5 mbar of the poisoning oxygenate vapor for 10 min at 50 °C. Following evacuation of the chamber, the temperature was increased to 100, 150, 200, and 250 °C (10 °C/min). The poisoned wafer was then exposed to 0.5 mbar of methanol (VWR International $\geq 99.8\%$) vapor for 15 min. The chamber was once again evacuated and the aforementioned TPD was repeated. For experiments with moisturized catalysts, H₂O (McMaster-Carr, 100% Distilled) vapor was dosed incrementally until the chamber reached an equilibrium pressure of 0.5 mbar at 50 °C prior to dosing of both the respective poison and methanol.

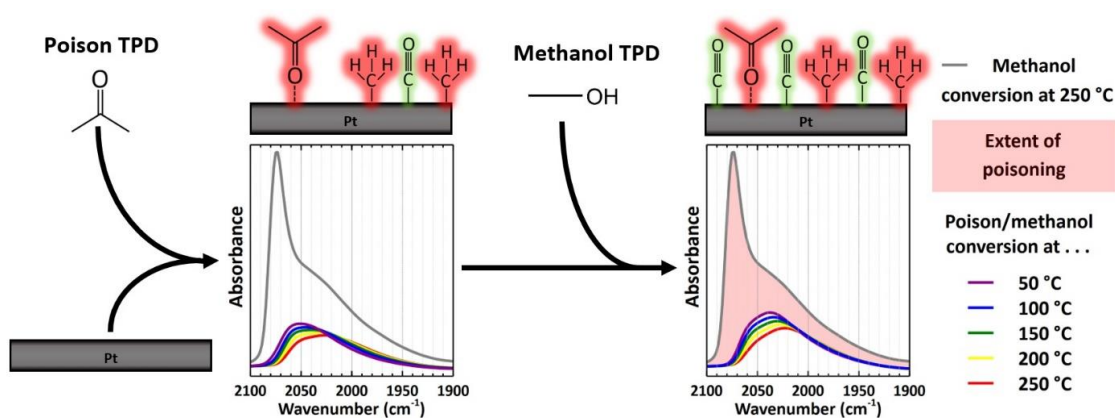


Figure 18. Sequence of TPDs with poisoning species and methanol as observed by IR spectroscopy.

4.2.3 Inelastic neutron scattering

A Pt sponge (Sigma Aldrich, $\geq 99.9\%$ trace metal basis) was employed for inelastic neutron scattering (INS) experiments to isolate and observe metal-bound surface species. The sponge was first reduced with 10% (v/v) H₂/He at 250 °C for 1 hr. BET isotherms⁴⁶ were collected via N₂ physisorption using a Micromeritics Gemini VII analyzer after

degassing at 250 °C for 2 hr. Based on the measured $\sim 36 \text{ m}^2/\text{g}$ surface area, 1.5 g of the Pt sponge were packed into an aluminum vessel within a dry helium glove box. Under HV at 250 °C, the sponge was exposed to small amounts of di/ketone vapor ($\sim 0.5 \text{ mbar}$) for 15 min. The vessel was then again evacuated to remove any physisorbed species.

The VISION vibrational spectrometer at the Oak Ridge National Laboratory (ORNL) Spallation Neutron Source (SNS) ¹⁸⁸ was used to perform INS experiments and observe the vibrational modes of Pt-adsorbed surface species at low energies ($< 500 \text{ cm}^{-1}$). The instrument determined the incident neutron energy with time-of-flight scattering using a series of 13 curved, pyrolytic graphite analyzers. Parameters included a dynamic range of 0 – 1000 meV, resolution of $< 1.0 - 1.5 \%$, and a diffraction range of $1.5 - 3.0 \text{ \AA}^{-1}$. The beam line was equipped with a closed-cycle, top-loading refrigerator maintained at 5 – 600 K. Data was collected in event mode and subsequently refined with background subtraction (clean Pt sample and aluminum vessel), rebinning to improve count statistics, and some smoothing (moving average) to reduce statistical noise.

4.2.4 *Density Functional Theory*

The DFT calculations were performed using the Vienna Ab initio Simulation Package (VASP),¹²⁸⁻¹³² which uses plane wave basis sets up to an energy cutoff of 400eV, the PAW pseudopotentials¹³³⁻¹³⁴ and the PBE exchange correlation functional.¹³⁵ The D3 dispersion correction with Becke-Johnson damping.¹³⁶⁻¹³⁷ Spin polarization was turned on, and dipole corrections were applied in the direction normal to the surface. The first Brillouin zones were sampled using $3 \times 3 \times 1$ Monkhorst–Pack G-centered k-point meshes.¹³⁸ Electronic structures are considered converged until the difference between

subsequent iterations was no larger than 10^{-6} eV. Geometries are considered converged when the forces on all atoms are below 0.03 eV/Å in geometry optimizations.

For the vacuum phase calculations, a simulation box of $20 \times 20.1 \times 20.2$ was used and a $3 \times 3 \times 3$ k-point mesh, keeping the previously mentioned parameters in section the same. The simulation supercell (**Figure C1**) is formed from a Platinum FCC bulk with a lattice parameter of 2.8 Å, from it a Platinum (111) surface slab composed with 108 atoms was built, containing three atomic layers and lattice constants $a = b = 16.8$ Å, $c = 19.6$ Å and $\alpha = \beta = 90^\circ$, and $\gamma = 60^\circ$. The closest distance between catalytic species in neighboring images is 11 Å. Binding energies are calculated according to **Equation 4**, subtracting the electronic energies of the adsorbed species in the platinum slab ($E_{Adsorbate*}$) and subtract it from the electronic energy from the slab (E_{Slab}) and the adsorbate in vacuum ($E_{Adsorbate}$).

$$E_{Binding} = E_{Adsorbate*} - (E_{Slab} + E_{Adsorbate}) \quad (4)$$

4.3 Results

4.3.1 Characterization

Detailed characterization data for the two Pt/ γ -Al₂O₃ catalysts is reported elsewhere.¹³⁹ The metal particle size distribution of the Pt_S/ γ -Al₂O₃ ranged from ~0.5 to ~2.0 nm with an average diameter of ~1.1 nm. That of Pt_L/ γ -Al₂O₃ was ~1.0 to ~8.3 nm with an average diameter of ~4.6 nm. Therefore, the former catalyst is expected to have a

high fraction of undercoordinated Pt sites while a high fraction of terrace sites can be attributed to the latter. Both catalysts exhibited similar BET surface areas of $\sim 70 \text{ m}^2/\text{g}$. The Lewis acidity of the $\gamma\text{-Al}_2\text{O}_3$ was measured as 104 and 72 $\mu\text{mol/g}$ at 150 and 250 $^\circ\text{C}$, respectively.

4.3.2 *Di/Ketone adsorption on small Pt particles*

The conversion of methanol on $\text{Pt}/\gamma\text{-Al}_2\text{O}_3$ catalysts is known to result in adsorbed CO due to dehydrogenation on metal sites.¹³⁹ This is evident by band developments in the 1900 – 2150 and 1750 – 1900 cm^{-1} regions that are attributed to the stretching modes of linear CO (CO_L) and bridging CO (CO_B), respectively.^{31, 189} During methanol conversion on $\text{Pt}_\text{S}/\gamma\text{-Al}_2\text{O}_3$, the primary $\nu(\text{C}\equiv\text{O})$ band was centered at 2050 cm^{-1} and was assigned to CO_L on metallic Pt sites (**Figure 19a**). The large, low frequency shoulder that extended as low as 1900 cm^{-1} is characteristic of CO adsorbed near the interface between metal particles and Lewis acidic supports such as $\gamma\text{-Al}_2\text{O}_3$.^{42, 53} The mid-frequency shoulder at 2072 cm^{-1} was attributed to adsorbed CO that is closely surrounded by other CO species that engage in dipole-dipole coupling, a phenomenon that results in slightly stronger $\text{C}\equiv\text{O}$ bonds and a distinguishable band.⁵⁰ The highest frequency shoulder at 2115 cm^{-1} is often assigned to CO adsorbed to single Pt atoms⁵⁵⁻⁵⁶ or Pt sites near adsorbed Cl⁶⁹ from the H_2PtCl_6 synthesis precursor.

This deconvolution of the CO stretching bands provided insight into the locations of CO formed from the decarbonylation of ketones and diketones on $\text{Pt}_\text{S}/\gamma\text{-Al}_2\text{O}_3$ (**Figure 19**). In addition, the $\nu(\text{C}\equiv\text{O})$ frequencies observed during subsequent methanol dehydrogenation showed which sites are occupied by adsorbed poisons. The full IR spectra

of products from methanol and di/ketones adsorbed to $\text{Pt}/\gamma\text{-Al}_2\text{O}_3$ can be seen in **Figure C2**.

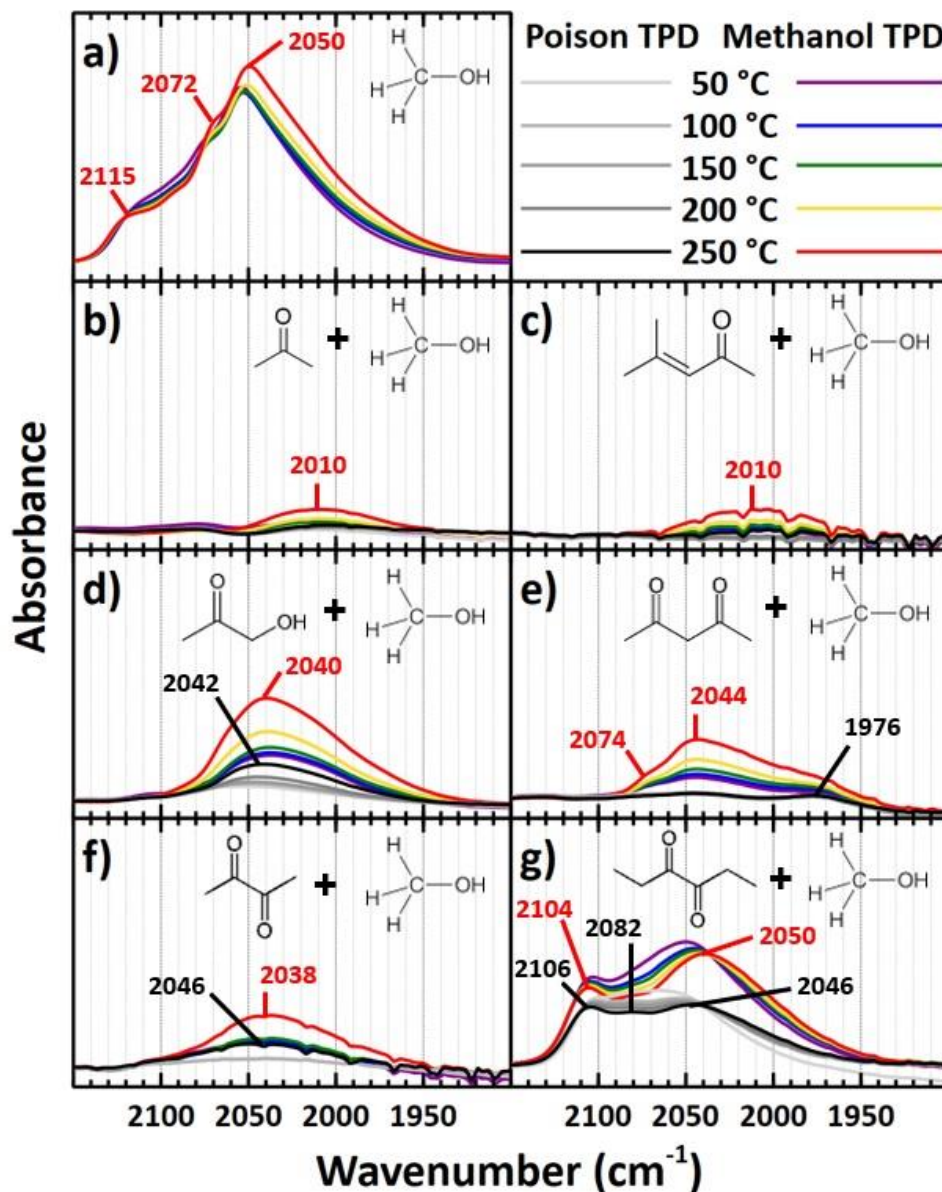


Figure 19. IR spectra of adsorbed CO during TPD experiments with $\text{Pt}/\gamma\text{-Al}_2\text{O}_3$ (~1.1 nm Pt particles) up to 250 °C. **a)** Methanol TPD on clean $\text{Pt}/\gamma\text{-Al}_2\text{O}_3$. Methanol TPDs following poison TPDs in which the poison is **b)** acetone, **c)** mesityl oxide, **d)** hydroxyacetone, **e)** 2,4 pentanedione, **f)** 2,3 butanedione, and **g)** 3,4 hexanedione. Major band frequencies are labeled for adsorbed CO resulting from poison decarbonylation (black) and methanol dehydrogenation (red). All scans were taken at 50 °C.

On small Pt particles, no decarbonylation activity was witnessed when acetone and mesityl oxide were adsorbed (**Figure 19b and Figure 19c**). The development of the CO_L band during subsequent methanol adsorption was very similar for these ketone species given both sets of spectra include a small broad band centered at 2010 cm⁻¹. This could be, in part, due to the conversion of acetone into mesityl oxide by aldol condensation on the Lewis acid sites of the γ -Al₂O₃ support.^{118, 167} Subsequent methanol adsorption resulted in only a slight increase in intensity of the 2010 cm⁻¹ band. As hydroxyacetone was adsorbed, a small CO_L band appeared at 2042 cm⁻¹ evident of some decarbonylation on Pt particles (**Figure 19d**). The further notable development of this band during methanol exposure suggests methanol was still able to dehydrogenate on open Pt sites, including those near the metal/support interface. However, the high frequency bands at 2072 and 2115 cm⁻¹ seen during methanol adsorption on clean Pt₅/γ-Al₂O₃ were absent.

There was minimal decarbonylation of 2,4 pentanedione, the β-diketone, even as high as 250 °C (**Figure 19e**). A very small band at 1976 cm⁻¹ suggested the only decarbonylation occurred near the metal/support interface. However, when methanol was adsorbed, the appearance of distinct bands at 2044 and 2074 cm⁻¹ and a low frequency shoulder implied that methanol was still able to dehydrogenate on a range of different metal sites. Yet, the magnitude of the band was significantly reduced compared to that of the control experiment. The α-diketones, 2,3 butanedione and 3,4 hexanedione, behaved very different on small Pt particles (**Figure 19f and Figure 19g**). Adsorption of the former species resulted in a small, lone broad band at 2046 cm⁻¹. During exposure to methanol, this band and a low frequency shoulder grew only slightly with the primary frequency red shifting to 2038 cm⁻¹. This observation was heavily contrasted by that of 3,4 hexanedione

adsorption. Not only did the larger α -diketone decarbonylate on a variety of sites given the distinct bands witnessed at 2046, 2082 and 2106 cm^{-1} , but the resulting CO_L band was notably larger than that seen during 2,3 butanedione adsorption. This suggested that 3,4 hexanedione decarbonylated on metal sites much more readily than 2,3 butanedione. Subsequent methanol adsorption on 3,4 hexanedione-poisoned $\text{Pt}_\text{s}/\gamma\text{-Al}_2\text{O}_3$ led to growth of the 2046 and 2106 cm^{-1} bands and a gradual shift to 2050 and 2104 cm^{-1} , respectively, at 250 °C. The low frequency shoulder also grew in magnitude. However, the total integral of the final CO_L band during exposure to 3,4 hexanedione and methanol also fell short of that of the control experiment.

4.3.3 *Di/Ketone adsorption on large Pt particles*

The conversion of methanol on $\text{Pt}_\text{L}/\gamma\text{-Al}_2\text{O}_3$ catalyst also resulted in dehydrogenation as indicated by a strong $\nu(\text{C}\equiv\text{O})$ band associated with CO_L (**Figure 20a**). However, this band exhibited a shape different from that of CO_L on smaller Pt particles. For instance, the contribution at 2075 cm^{-1} was dominant for CO on large Pt particles. As aforementioned, this frequency was attributed to adsorbed CO species participating in dipole-dipole coupling, a phenomenon that occurs to much greater extents on the larger terraces of larger Pt particles.⁶⁸ The spectra also contained a smaller feature centered at 2040 cm^{-1} and a broad low frequency shoulder that extended as low as 1900 cm^{-1} . Similar to that of CO on small Pt particles, these represent CO_L bound in isolation to metallic Pt and Pt near the metal/support interface, respectively.^{42, 53} Full IR spectra of are displayed in **Figure C3**.

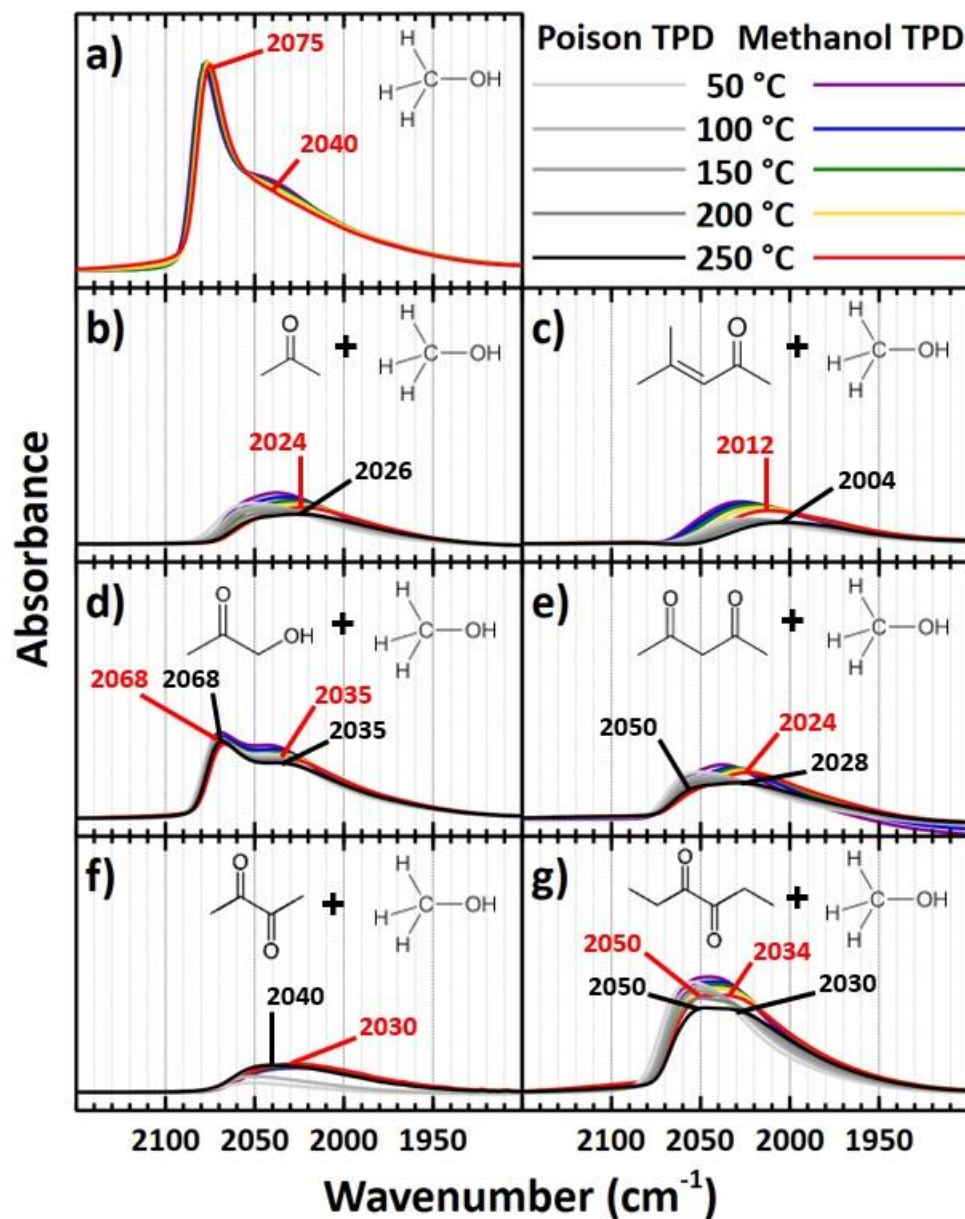


Figure 20. IR spectra of adsorbed CO during TPD experiments with Pt_L/γ-Al₂O₃ (~4.6 nm Pt particles) up to 250 °C. **a)** Methanol TPD on clean Pt_L/γ-Al₂O₃. Methanol TPDs following poison TPDs in which the poison is **b)** acetone, **c)** mesityl oxide, **d)** hydroxyacetone, **e)** 2,4 pentanedione, **f)** 2,3 butanedione, and **g)** 3,4 hexanedione. Major band frequencies are labeled for adsorbed CO resulting from poison decarbonylation (black) and methanol dehydrogenation (red). All scans were taken at 50 °C.

Acetone and mesityl oxide conversion on Pt_L/γ-Al₂O₃ resulted in similar CO_L bands (**Figure 20b** and **Figure 20c**), due to decarbonylation, with frequencies of 2026 and 2004

cm^{-1} , respectively. Although small and broad, these bands appeared larger than those on $\text{Pt}_\text{s}/\gamma\text{-Al}_2\text{O}_3$, suggesting that a greater extent of decarbonylation took place on larger Pt particles, or highly coordinated Pt sites. Yet, only slight growth of the CO_L band occurred during extended methanol exposure. In addition, there was an apparent red shift and broadening of the CO_L bands as the temperature increased from 50 to 250 °C during experiments with acetone and mesityl oxide. Specifically, during conversion of acetone, the $\nu(\text{C}\equiv\text{O})$ frequency shifted from 2052 to 2026 cm^{-1} . During subsequent methanol adsorption at 50 °C, the band grew slightly with a new primary $\nu(\text{C}\equiv\text{O})$ frequency of 2038 cm^{-1} , which red shifted similarly to 2024 cm^{-1} upon heating to 250 °C. For the mesityl oxide experiment, the shifts were 2028 to 2004 cm^{-1} and 2028 to 2012 cm^{-1} after dosing mesityl oxide and methanol, respectively. These observations suggest that while ketone decarbonylation and methanol dehydrogenation initially take place on highly coordinated sites, the red shifts likely represent the migration of adsorbed CO to more undercoordinated sites with increasing temperature where the surface species binds more strongly.¹⁹⁰ The CO_L band for hydroxyacetone adsorption on $\text{Pt}_\text{L}/\gamma\text{-Al}_2\text{O}_3$ also appeared much larger than that on $\text{Pt}_\text{s}/\gamma\text{-Al}_2\text{O}_3$ and exhibited two distinct features (**Figure 20d**). A sharp band at 2068 cm^{-1} and a broad band centered at 2035 cm^{-1} . The existence of these 2068 and 2035 cm^{-1} bands implied that hydroxyacetone decarbonylates on a variety of metal sites with the resulting CO species agglomerating together and participating in dipole-dipole coupling. Minimal growth of these bands occurred during subsequent methanol conversion. In fact, the bands exhibited consistent frequencies at 2035 and 2068 cm^{-1} from hydroxyacetone conversion at 50 °C to attempted methanol dehydrogenation at 250 °C, suggesting that the existing surface species were stable on large Pt particles.

When adsorbed to Pt_L/γ-Al₂O₃, 2,4 pentanedione decarbonylated to a limited extent to form a small CO_L band with distinct features at 2050 and 2028 cm⁻¹ (**Figure 20e**). Methanol dehydrogenation was severely hindered on the 2,4 pentanedione-possioned surface given the lack of band growth during the respective TPD. Like those of acetone and mesityl oxide, the spectra revealed a red shift of the overall band with increasing temperatures, suggesting adsorbed CO migrated to undercoordinated Pt sites.¹⁹¹ Adsorption of the α-diketones displayed contrasting effects (**Figure 20f and Figure 20g**) on Pt_L/γ-Al₂O₃, like those seen on Pt_S/γ-Al₂O₃. 2,3 butanedione was decarbonylated to a minimal extent even at 250 °C, leading to a weak, broad CO_L band centered at 2040 cm⁻¹ with a low frequency shoulder. Subsequent dosing of methanol resulted in virtually no changes to the CO_L band with the exception of a red shift to 2030 cm⁻¹, suggesting molecular 2,3 butanedione or a derivative surface species bound very strongly to the Pt particles and blocked sites that would otherwise be available for methanol dehydrogenation. On the contrary, 3,4 hexanedione was readily decarbonylated as it did on small Pt particles, with distinct CO_L bands at 2050 and 2030 cm⁻¹. Slight growth of these bands occurred following methanol adsorption with only a slight shift of the latter band to 2034 cm⁻¹.

4.3.4 Evolution of CO_L band integrals

Quantitative analysis of the overall CO_L band was conducted to estimate the extent of poisoning by each ketone and diketone species. The CO_L integrals acquired during poison and methanol adsorption were compared directly to that of methanol conversion on clean Pt/ γ-Al₂O₃ catalysts at the same temperatures from 50 to 250 °C (**Figure 21**).

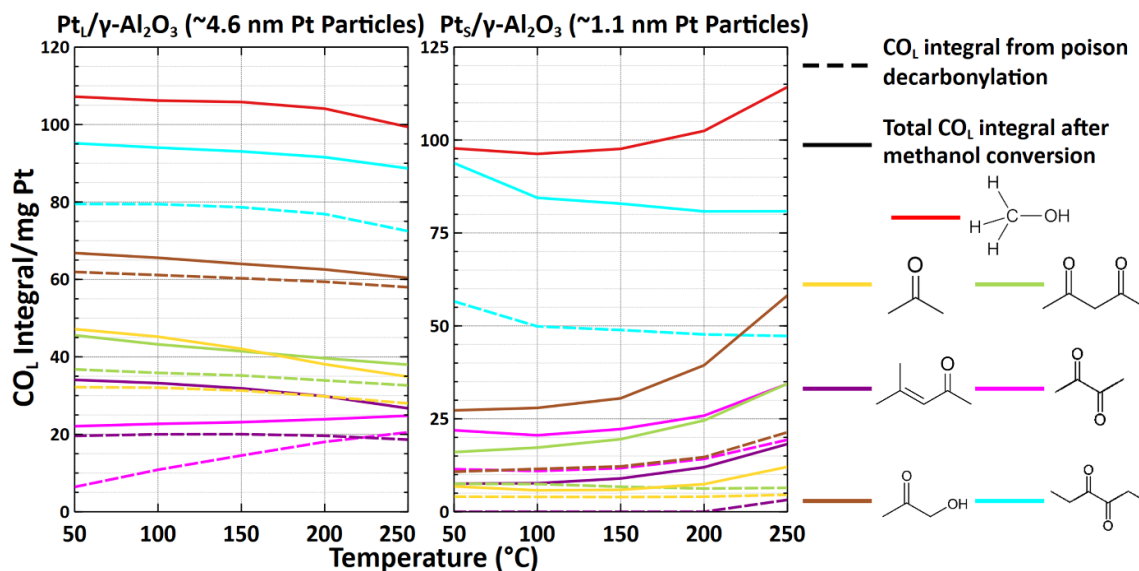


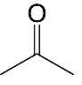
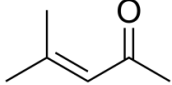
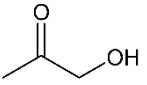
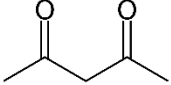
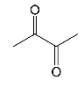
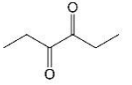
Figure 21. Integrals of the $\nu(\text{C}\equiv\text{O})$ IR band during poison adsorption (dashed lines) and subsequent methanol adsorption (solid lines) from 50 to 250 °C on both small and large Pt particles (left and right, respectively).

The focus was on the percent differences in CO_L band integrals at 250 °C following methanol adsorption (**Table 9**) given typical APR temperatures fall in the range of 200 – 270 °C.¹⁵ Overall, greater reductions in CO_L band integrals were observed during methanol conversion on $\text{Pt}_S/\gamma\text{-Al}_2\text{O}_3$ when pre-exposed to di/ketones. This may suggest that larger Pt particles, or highly coordinated Pt sites, are more active in di/ketone decarbonylation. Regardless of the Pt particle size, the least severe poisons were 3,4 hexanedione and hydroxyacetone.

For $\text{Pt}_S/\gamma\text{-Al}_2\text{O}_3$, pre-adsorbed acetone resulted in the highest reduction of the CO_L band integral during methanol conversion at 250 °C (89%). Pre-adsorbed mesityl oxide showed a similar effect with a 84% reduction of the CO_L band integral. Because acetone readily converts into mesityl oxide through aldol condensation on $\gamma\text{-Al}_2\text{O}_3$,^{118, 141} it is possible that smaller Pt particles, which consist of many interfacial sites, are also poisoned

by species formed from acid-catalyzed reactions on the support. A previous study consisting of IR spectroscopy revealed all of the di/ketones in this study to result in unique chemistry when adsorbed to γ -Al₂O₃, most of which involved the formation of heavier conjugated surface species from aldol condensation at 250 °C.¹⁹²

Table 9. Fractional decreases in total CO_L band integrals at 250 °C following poison and methanol TPDs on Pt/ γ -Al₂O₃ catalysts under HV.

| Catalyst |  |  |  |  |  |  |
|---|---|---|---|--|---|---|
| Pt _S / γ -Al ₂ O ₃ (~1.1 nm) | 89% | 84% | 49% | 70% | 70% | 29% |
| Pt _L / γ -Al ₂ O ₃ (~4.6 nm) | 65% | 73% | 39% | 62% | 75% | 11% |

For Pt_L/ γ -Al₂O₃, pre-adsorbed 2,3 butanedione led to the greatest CO_L band integral reduction (75%), suggesting this particular diketone acts as a strong binding poison. A similar magnitude was observed with mesityl oxide (73%), suggesting that both interfacial sites and more metallic, coordinated sites are vulnerable to strong binding by the conjugated ketone.

4.3.5 Inelastic neutron scattering

INS spectra were acquired to corroborate the existence of strongly binding alkyl groups resulting from di/ketone decarbonylation on a Pt sponge (**Figure 22**). In the case of acetone, for instance, two methyl groups are expected for every adsorbed CO species that was observed in the IR spectra. Similar conclusions can be made for other di/ketones. Pure substance reference INS spectra were acquired for each di/ketone species adsorbed to the Pt sponge (**Figure C4**).

Several INS bands of statistical significance were revealed in the 100 – 600 cm^{-1} range for species on the Pt surface formed from acetone, 2,3 butanedione, and 3,4 hexanedione. Band assignments are listed in **Table 10**. The primary band of interest, located at 304 – 308 cm^{-1} , was observed in each spectrum and was assigned to the A_2 methyl torsional mode of a CH_3 group chemisorbed to a metal site.¹⁹³ The same assignment was made for the 304 cm^{-1} band of the INS spectrum of 3,4 hexanedione-derived surface species on. The band appeared much larger in the INS spectrum of surface species formed from acetone and 3,4 hexanedione compared to those from 2,3 butanedione. This was in agreement with observations of the CO_L band in the IR spectra, which suggested that the former species decarbonylate more readily than 2,3 butanedione on Pt terrace sites, or $\text{Pt}_L/\gamma\text{-Al}_2\text{O}_3$, thus resulting in a larger coverage of methyl or ethyl groups on the Pt surface. Other bands potentially related to methyl group vibrations include those at around 450 – 460 and 500 – 510 cm^{-1} that formed a somewhat convoluted feature. These particular bands were assigned to the $\delta(\text{Pt-C})$ and $\nu(\text{Pt-CH}_3)$ mode of surface methyl groups, respectively.¹⁹³⁻¹⁹⁴

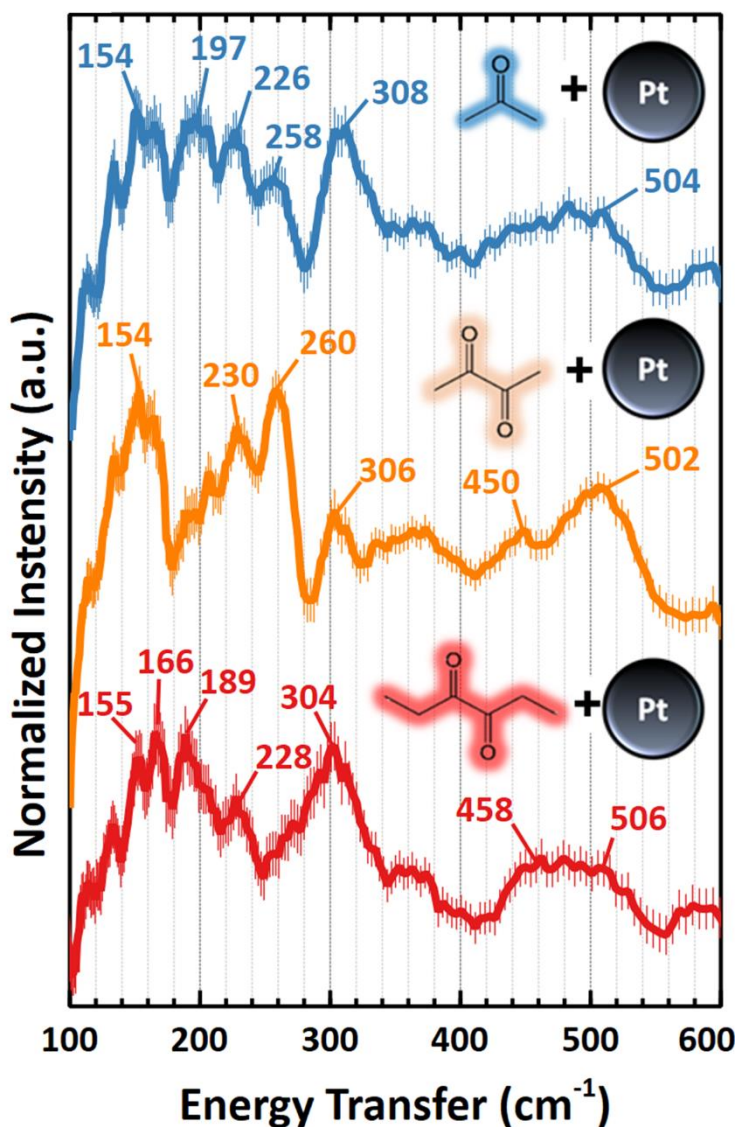


Figure 22. INS of spectra of Pt-bound surface species formed from acetone (blue), 2,3 butanedione (orange), and 3,4 hexanedione (red) with significant bands labeled. Data obtained from collaborators are Oak Ridge National Laboratory.

Various bands were also observed below 300 cm^{-1} . These may possibly be a result of bulk phonon or $\nu[\text{Pt}(\text{CH}_3)\text{-Pt}(\text{CH}_3)]$ modes due to excitation of the Pt sponge. On the other hand, they also may indicate the presence of other alkyl surface species produced from Pt-catalyzed reactions with methyl groups. For instance, Fairbrother et al. adsorbed

methyl radicals to a Pt(111) surface and used reflection-absorption infrared spectroscopy to demonstrate coverage-dependent reaction kinetics which occurred as low as 230 K.¹⁹⁵ They concluded that methyl groups may dehydrogenate and couple to form to form ethylidyne species at high coverages while dehydrogenation into CH_x (X < 3) species was much more significant at low coverages. Given the adsorption of di/ketones for INS experiments was conducted at a much higher temperature of 250 °C and that low coverages were maintained, it is likely that dehydrogenation of surface methyl groups has also occurred herein and may partially explain the presence of bands located below 300 cm⁻¹. Unfortunately, the lack of studies spectroscopically probing such dehydrogenation products (e.g. methylene) made it difficult to make accurate assignments for each individual band. However, band assignments made by Chinta et al. regarding similar species, such as vinylidene and ethylidyne, on metal catalysts suggest the region below 300 cm⁻¹ may be unique to metal bound dehydrogenation products as methylene. In addition, the band at 500 – 510 cm⁻¹ could also be attributed to the $\delta(\mu^3\text{-H})$ mode of low coverage surface hydrogen resulting from methyl group dehydrogenation.¹⁹⁶

Table 10. INS band assignments for di/ketones adsorbed on a Pt sponge.

| Mode | Adsorption Reagent and vibrational frequencies (cm ⁻¹) | | |
|---|--|-----------------|-----------------|
| | Acetone | 2,3 Butanedione | 3,4 Hexanedione |
| v(Pt-Pt), bulk Pt phonons,¹⁹³ or Pt-CH_x (X < 3) related modes¹⁹⁵ | 154 | 154 | 155 |
| | | | 166 |
| | 197 | | 189 |
| | 226 | 230 | 228 |
| | 258 | 260 | |
| $\tau(\text{CH}_3)^{193}$ | 308 | 306 | 304 |
| $\delta(\text{Pt-C})^{193}$ | | 450 | 458 |
| v(Pt-CH₃)¹⁹⁴ or $\delta(\mu^3\text{-H})^{196}$ | 504 | 502 | 506 |

4.3.6 DFT Models of Adsorbate Configuration

The orientations of Pt(111)-adsorbed ketones were optimized based on DFT calculations and are illustratively compared in **Figure 23**. Acetone adsorbed in an upright position, bound to Pt via the oxygen atom with one of the methyl groups pointing away from the surface (**Figure 23a,b**). The model is reminiscent of a monodentate (η_1) adsorbate, perhaps bound to the surface through a σ -bond. These results are well in agreement with those of previous studies that focused on modeling acetone adsorption on metallic surfaces including Pt(111).^{112, 185, 197} Mesityl oxide (**Figure 23c,d**), the product of acetone condensation, however, binded almost completely flat on Pt(111). Both the C=O and C=C bonds were aligned parallel with the surface as a bidentate ($2 \times \eta_2$) species with more π -bond character. The methyl groups of the carbonyl and isobutenyl groups exhibited much less flexibility, seemingly unable to point away from the surface as seen with acetone. Hydroxyacetone (**Figure 23e,f**) also bound to Pt with the carbonyl group parallel with the surface. The adjacent alcohol group also appeared to bind directly to the surface via the oxygen atom with a small Pt-O-C angle. This orientation is perhaps favorable due the maintained intramolecular hydrogen bonding.

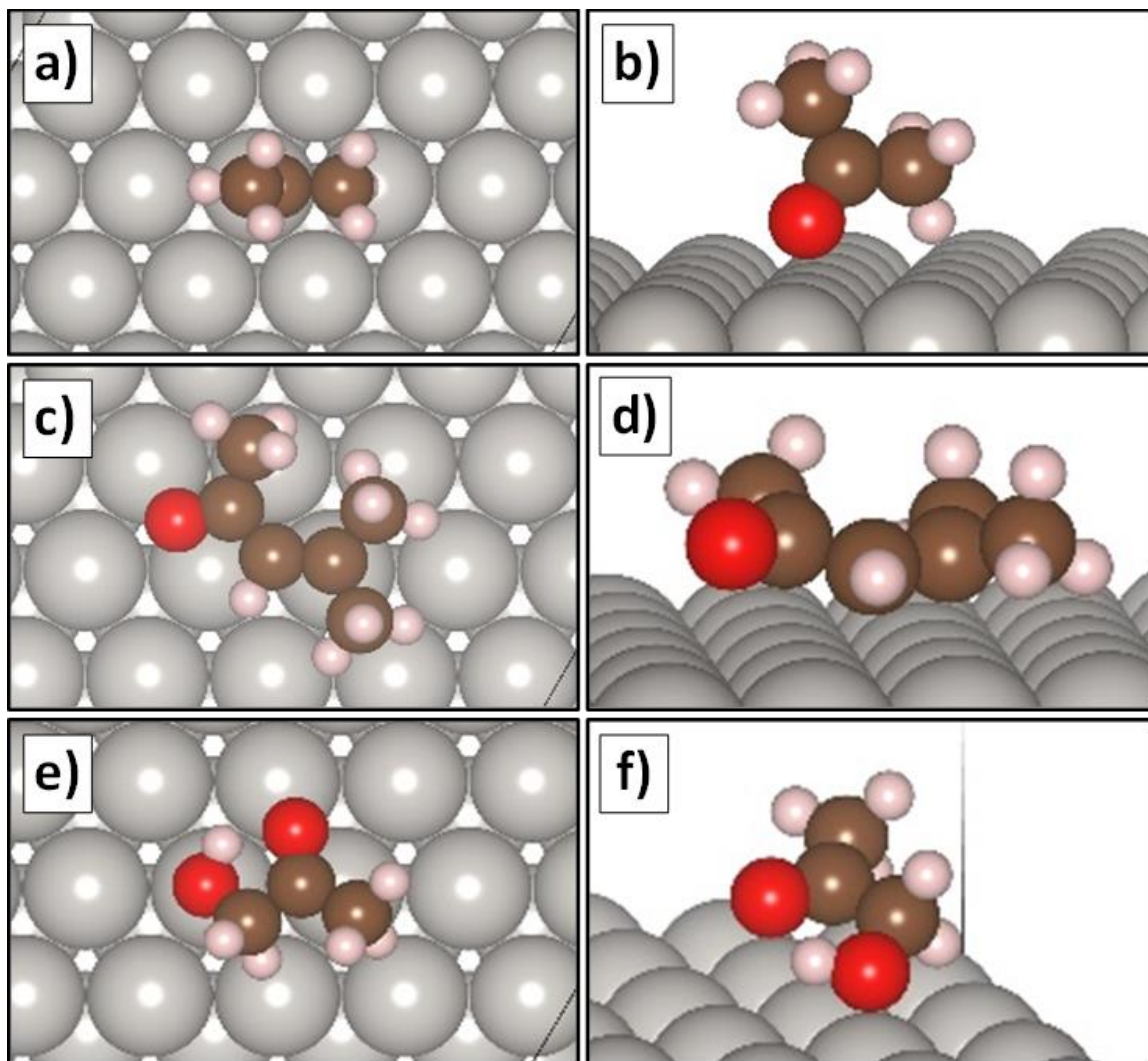


Figure 23. Optimized configurations of ketones adsorbed to a Pt(111) slab under vacuum. **a)** Top and **b)** side view of acetone, **c)** top and **d)** side view of mesityl oxide, **e)** top and **f)** side view of hydroxyacetone. Configurations obtained by collaborators from Clemson University.

Diketone configurations are shown in **Figure 24**. Adsorbed 2,4 pentanedione (**Figure 24a,b**) appeared to bind nearly flat on Pt(111). In addition, the carbonyl groups point in different directions with a wide $\text{O}=\text{C}-\text{C}-\text{C}=\text{O}$ angle. As for 2,3 butanedione (**Figure 24c,d**), the corresponding surface species also binds flat. The symmetric

orientations of these diketones appear reminiscent of bidentate η_2 adsorbates with π -bond character. This contrasts the acquired model for adsorbed 3,4 hexanedione (**Figure 24e,f**). The larger α -diketone was adsorbed with the ethyl groups pointing away from the surface. In addition, the adsorbate is asymmetric with two distinguishable carbonyls. One carbonyl group appeared to be upright with respect to the surface, potentially with a η_1 interaction. The other carbonyl group is more flat but may still be close enough to the surface to maintain a weak η_2 bond.

The binding energies of Pt(111)-adsorbed di/ketones (**Table 11**) were calculated using **Eqn. 4**. Acetone had the weakest binding energy of -0.795 eV. The addition of adjacent functional groups seemed to increase this binding energy to -1.065 and -0.994 eV for mesityl oxide and hydroxyacetone on Pt(111), respectively. The diketones 2,4 pentanedione and 3,4 hexanedione exhibited similar binding energies of -1.079 and -1.095 eV, respectively. However, the binding energy of 2,3 butanedione was calculated to be much higher than that of the other model adsorbates at -1.546 eV, implying that this species exhibited the strongest interaction with Pt(111).

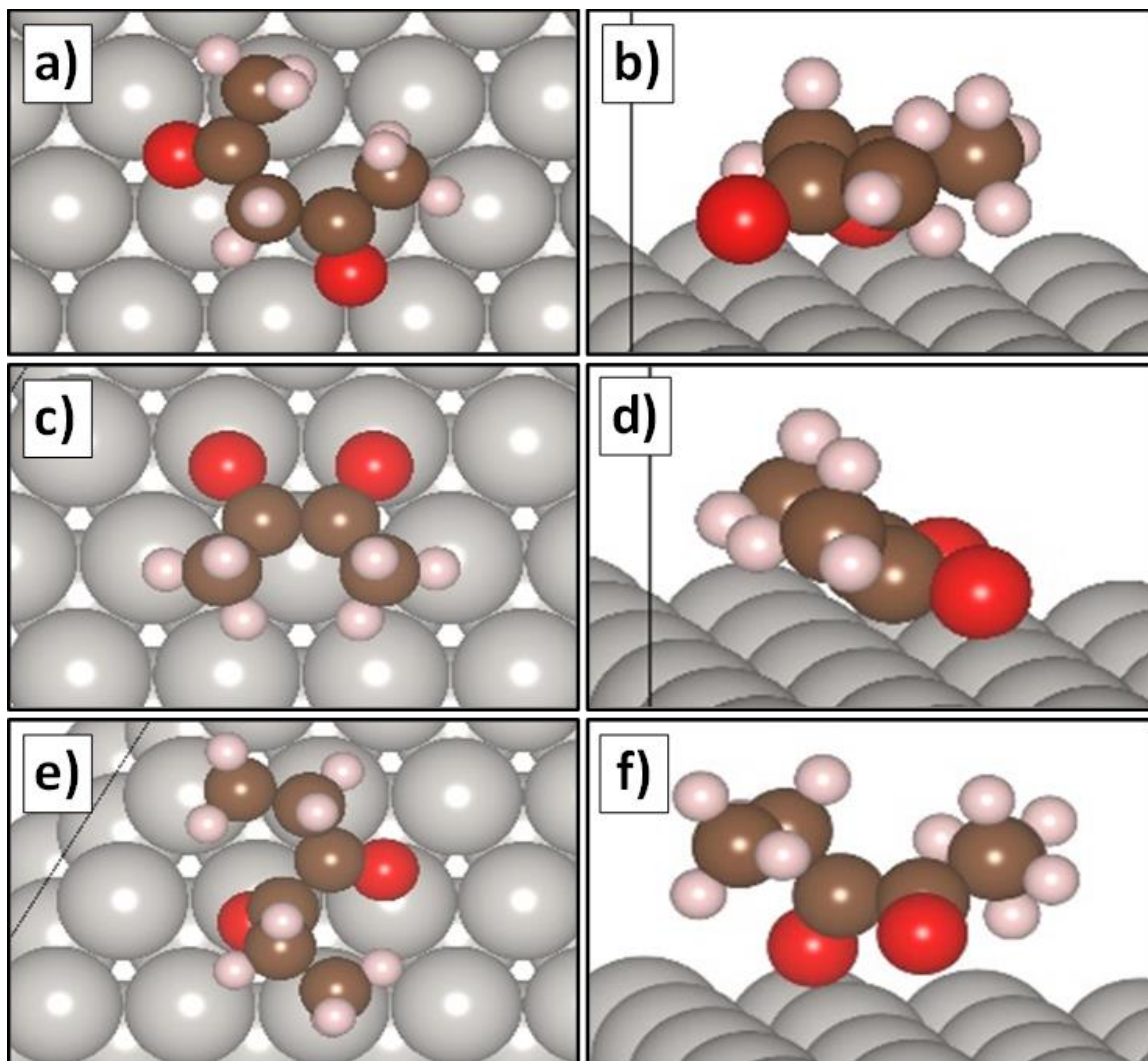


Figure 24. Optimized configurations of diketones adsorbed to a Pt(111) slab under vacuum. **a)** Top and **b)** side view of 2,4 pentanedione, **c)** top and **d)** side view of 2,3 butanedione, **e)** top and **f)** side view of 3,4 hexanedione. Configurations obtained by collaborators from Clemson University.

Table 11. Binding energies for Pt(111)-adsorbed di/ketones. Calculations performed by collaborators from Clemson University.

| Structure | Binding Energy (eV) |
|----------------------------------|---------------------|
| Acetone | -0.80 |
| Mesityl Oxide | -1.07 |
| Hydroxyacetone | -0.99 |
| 2,4 Pentanedione | -1.08 |
| 2,3 Butanedione | -1.55 |
| 3,4 Hexanedione | -1.10 |
| Methyl Group (*CH ₃) | -2.53 |

4.3.7 Thermodynamics of potential reaction paths of surface methyl groups

In principle, the adsorbed CO produced by di/ketone decarbonylation should be accompanied by the alkyl groups originally bound to the carbonyl group(s). In the case of acetone, two methyl groups should be produced per adsorbed CO species. A binding energy of -2.529 eV was calculated for methyl groups chemisorbed to Pt(111) (**Table 11**). In comparison to those of the molecular di/ketones, this implies that these particular alkyl groups bind much stronger to Pt(111) than their respective parent species (acetone, mesityl oxide, hydroxyacetone, 2,4 pentanedione, and 2,3 butanedione) and may also act as a catalyst poison.

Table 12. Reaction energies for processes on Pt(111) that produce and consume methyl groups under APR conditions. Calculations performed by collaborators from Clemon University.

| Reaction | | Reaction energy (eV) |
|--|---|----------------------|
| Acetone Decarbonylation | $(\text{CH}_3)_2\text{CO}^* + 2^* \rightarrow 2\text{CH}_3^* + \text{CO}^*$ | -1.55 |
| Methyl-Hydride Association | $\text{CH}_3^* + \text{H}^* \rightarrow \text{CH}_4(\text{g})$ | 0.73 |
| Methyl-Methyl Association | $2\text{CH}_3^* \rightarrow \text{C}_2\text{H}_6^*$ | 0.48 |
| Methyl Oxidation by H₂O (1) | $2\text{CH}_3^* + 2\text{H}_2\text{O} \rightarrow 2\text{CH}_3\text{OH} + \text{H}_2$ | 1.13 |
| Methyl Oxidation by H₂O (2) | $2\text{CH}_3^* + \text{H}_2\text{O} \rightarrow \text{CH}_3\text{OH} + \text{CH}_4$ | 0.62 |
| Methyl Oxidation by H₂O (3a) | $\text{CH}_3^* + \text{H}_2\text{O} + 5^* \rightarrow \text{CO}^* + 5\text{H}^*$ | -2.32 |
| Methyl Oxidation by H₂O (3b) | $\text{CH}_3^* + \text{H}_2\text{O}^* + 4^* \rightarrow \text{CO}^* + 5\text{H}^*$ | -1.84 |
| Methyl Dehydrogenation | $\text{CH}_3^* + ^* \rightarrow \text{CH}_2^* + \text{H}^*$ | 0.05 |

The energies of reactions involving methyl groups on Pt(111) were calculated (Table 12) and are perhaps reminiscent of those occurring on large, supported Pt particles with large fractions of highly coordinated sites. That of acetone decarbonylation was also presented for direct comparison. The -1.55 eV reaction energy for acetone decarbonylation suggests that the process is favorable on Pt terrace sites. This corroborates the CO formation observed during acetone adsorption on Pt_L/γ-Al₂O₃ as low as 50 °C (Figure 20b). Under APR conditions, contemplated methyl group consumption reactions included association, oxidation by H₂O, and dehydrogenation and coupling into a methyldiene species. Association would result in either methane or ethane with calculated reaction energies of 0.73 and 0.48 eV, respectively. The oxidation option could occur through two distinct pathways: Reaction with two H₂O molecules to produce methanol and hydrogen (1.13 eV) or with one H₂O molecule to produce methanol and methane (0.62 eV). Finally, the dehydrogenation of a methyl group to form a methylene group was also considered yet

was calculated to have a reaction energy of 0.69 eV. The positive energies of these reactions suggest the removal of methyl groups is comparatively unfavorable with respect to their production and that their consumption would reduce the energy efficiency of APR.

4.4 Discussion

4.4.1 Decarbonylation of di/ketones on small and large Pt particles

In the field of heterogeneous catalysis, the size of supported metal particles often times exhibits a direct effect on the ability of metal sites to facilitate the creation or cleavage of chemical bonds.¹⁹⁸ For instance, the highly coordinated sites of large metal particles may reduce the activation energy of a reaction more so than the lowly coordinated sites of small metal particles (or vice versa). This may ultimately lead to observable differences in conversion of a reactant.

In regards to decarbonylation, the difference in activity between small and large Pt particles may in part be due to the configuration of adsorbed di/ketones on different metal sites. As the simplest ketone, acetone has been widely used to study ketone chemistry and adsorption.^{112, 141, 185} It is widely agreed between several studies that a carbonyl group can bind to Pt(111) with either singular hapticity (η^1) in which the molecule binds upright and tilted via a σ bond or dual hapticity (η^2) in which the carbonyl groups lies parallel to the surface through a di- σ interaction.^{112, 115, 185, 197} Delbecq and Sautet took an extensive theoretical approach to model adsorbed acetone on Pt terrace and step sites.¹⁸⁵ They concluded that acetone preferentially binds in an upright position on Pt(111) via a σ bond

due to strong repulsion between the methyl groups and metal surface. Although difficult to confirm experimentally due to low metal loading and rapid conversion of acetone, the modeled configuration for adsorbed acetone presented herein (**Figure 23a,b**) aligns well with their findings. The η^2 species is more characteristic of a di- σ bond between the carbonyl group and the Pt metal surface. Although this di- σ bond is energetically stronger than the σ -bond of the η^1 species, the attraction between the carbonyl group and the Pt surface is counteracted by a slight repulsion between the methyl groups and the metal surface, making the orientation less favorable on highly coordinated Pt sites. However, the authors also illustrated the binding orientation of acetone on a Pt step site, revealing that the molecule binds to the site via a di- σ interaction with the C=O bond aligned perpendicular to the edge. On a more exposed step site, the alkyl-metal repulsion is greatly reduced, allowing the di- σ bond and η^2 configuration to prevail. It was reported in another study that the η^2 species acts as the precursor for acetone decarbonylation into adsorbed CO and methyl groups on Pt(111),¹⁹⁷ suggesting that the steric repulsion is necessary to facilitate decarbonylation. At reaction temperatures, the varying extents of repulsion when di/ketones are adsorbed to highly and lowly coordinated Pt sites may potentially serve as a descriptor for explaining the differences in decarbonylation activity of different metal particle sizes.

The absorbance intensity of the CO_L band provided as a gauge for comparing conversion of methanol and di/ketones on a given Pt/ γ -Al₂O₃ catalyst. Overall, the larger metal particles of Pt_L/ γ -Al₂O₃ appeared more active in decarbonylation as indicated by the larger CO_L bands observed during di/ketone adsorption (**Figure 19 and Figure 20**). Furthermore, the subsequent adsorption of methanol on these larger Pt particles added to

the intensity of this band to closer match that of its clean counterpart indicating less pronounced poisoning by the di/ketones or their fragments (**Table 9**). This suggests that smaller Pt particles are more prone to poisoning than larger ones. However, given the diversity of di/ketones studied on Pt/ γ -Al₂O₃ catalysts, there are a few different chemical species that need to be discussed: Alkyl groups (decarbonylation fragments) and molecular di/ketones.

4.4.2 *Poisoning by alkyl groups and derivatives*

The deactivation of supported metal catalysts by strong binding and kinetically stable surface methyl groups is not new to the field of catalysis. Albers et al. reported strong evidence of adsorbed methyl groups on a Pd catalyst that originated from side reactions in various industrial chemical process including the hydrogenation of functionalized aromatics.¹⁹³ Not only can these methyl groups occupy metal sites and hinder adsorption, but large coverages may alter the surface polarity and thus the catalytic ability of the metal to facilitate the intended reaction. In principle, the formation of surface methyl groups (and other alkyl groups) occurs concomitantly with di/ketone decarbonylation. Therefore, the effects of these surface species herein cannot be ignored.

Larger Pt particles were poisoned less severely by di/ketones due to their higher decarbonylation activity. It can then be inferred that alkyl groups make up a notable coverage. For instance, pre-adsorbed acetone led to a 65% decrease in the CO_L band integral on Pt_L/ γ -Al₂O₃ during subsequent methanol dehydrogenation. Given the 2:1 stoichiometric formation of CH₃:CO surface species during acetone decarbonylation, it is likely this severe extent of poisoning is due to a near 65% coverage by surface methyl

groups. Interpretation of the INS spectra (**Figure 22**) not only presented evidence of these species under high vacuum, but also that they are stable at 250 °C, a temperature at which APR is commonly operated.

Given the thermodynamic stability and -2.53 eV Pt binding energy (**Table 11**), methyl groups, and other alkyl species, must be removed via a reaction to a thermodynamically favorable product. However, the reaction energies calculated herein (**Table 12**) show that the least complex potential reactions (ie., partial oxidation, associative desorption, etc.) are unfavorable and require additional energy input, especially when compared to the acetone decarbonylation reaction shown to occur very readily on large Pt particles with a reaction energy of -1.55 eV. The need for constant catalyst regeneration procedures due to poisoning by alkyl decarbonylation fragments would significantly reduce the efficiency of APR and other Pt-catalyzed reactions. This will be an important factor to consider for future studies that focus on designing Pt-based catalysts with greater resistance to chemical poisoning.

4.4.3 Poisoning by molecular di/ketones

Given the lower decarbonylation activity of small Pt particles, it is possible that adsorbed di/ketones retain their molecular structure and resist conversion when adsorbed to lowly coordinated Pt sites. In addition, di/ketones such as 2,3 butanedione and mesityl oxide still acted as strong poisons for large Pt particles. As aforementioned, the steric repulsion between alkyl groups and Pt terraces may potentially drive the decarbonylation of these species on larger Pt particles. Yet, this repulsion becomes a less significant factor

when adsorbed to more exposed metal sites.¹⁸⁵ Without this essential driving force, lowly coordinated sites may be vulnerable to poisoning by adsorbed di/ketones.

Other di/ketones in this study did not decarbonylate as readily as acetone at temperatures up to 250 °C, yet severely hindered methanol dehydrogenation. 2,3 Butanedione was the strongest poison for large Pt particles, decreasing the CO_L band integral by 75%. It also exhibited the highest binding energy, -1.55 eV, of all the molecular di/ketones adsorbed to Pt(111) and exhibited a relatively flat, symmetric orientation in which both carbonyl groups interact with the metal surface (**Figure 24c,d**). In contrast, 3,4 hexanedione, the larger α -diketone, only had a binding energy of -1.10 eV, bonded upright with monodenticity on Pt(111), and decarbonylated very readily on Pt/ γ -Al₂O₃ catalysts. It is suggested that the more bulky ethyl groups of 3,4 hexanedione prevent the adsorbed species from maintaining a stable flat orientation characteristic of di- σ bonds. For 2,3 butanedione, an adsorbed species with two di- σ bonds and smaller methyl groups, seems to overcome the influence of metal-methyl repulsion. This double di- σ bond interaction with highly coordinated Pt may be the thermodynamic driving force for poisoning large Pt particles.

Hydroxyacetone also bonded flat on the Pt(111) surface (**Figure 23e,f**) unlike acetone, suggesting the OH group stabilizes a surface species with more di- σ bond character. Yet hydroxyacetone decarbonylated very readily on large Pt particles (**Figure 20d**) with a measured poisoning extent of only 39%, but there was negligible subsequent dehydrogenation of methanol, suggesting surface coverage was dominated by hydroxyacetone-derived species. The observed poisoning extent suggests that hydroxyacetone decarbonylated to near completion given that the result should be 1:2

CH₃:CO (with some residual surface hydrogen) due to simultaneous dehydrogenation of the OH group. Just as the η^2 di- σ bond orientation is the decarbonylation precursor for adsorbed acetone, this same configuration for hydroxyacetone with an added interaction between the Pt and OH group may be necessary for the respective reaction. These perspectives are well in agreement with results reported by McManus et al. who showed that the formation of α -oxo- η^2 intermediates were essential for the reforming of C₃ aldoses on Pd.¹⁸⁴ While the study focused on the conversion of aldehydes, hydroxyacetone in this study still appeared to decarbonylate very readily as low as 50 °C, supporting this mechanism.

The few studies focusing on the adsorption of conjugated species onto metal surfaces have generally taken theoretical approaches. For instance, Loffreda studied the adsorption of several different conjugated species on a Pt(110) surface and revealed that conjugated ketones, as opposed to alkenes conjugated with other functional groups (carboxy, nitro, imino, etc.), bind more strongly to metal surfaces due to destabilization of the highest occupied molecular orbital (HOMO) of the molecule.¹⁹⁹ In another study, the same author reported that the trans configurations of these species generally bind flat on metallic surfaces with up to 4-fold hapticity on Pt.²⁰⁰ Not only does this work align well with the configurations reported herein for mesityl oxide on Pt(111) (**Figure 23c,d**), but the combined binding of both the C=O and C=C groups to the metal surface may explain the enhanced binding energy, -1.07 eV, compared to that of adsorbed acetone, -0.80 eV. However, ketone-alkene conjugation, and thus HOMO stabilization, was also reported to reduce the repulsion between the metal surface and the non-bonding alkyl components of

the adsorbed species.¹⁹⁹ This may in part explain why mesityl oxide did not poison large Pt particles as much as 2,3 butanedione.

It is widely known that aldol self condensation of acetone into mesityl oxide occurs very readily on Lewis acidic materials, including γ -Al₂O₃.^{118, 141-142, 167} It was also previously reported that several of the di/ketones employed in this study undergo some extent of enolization and aldol condensation to form bulky conjugated products when adsorbed to γ -Al₂O₃ at temperatures as low as 250 °C.¹⁹² This is important to consider when discussing the vulnerability of interfacial sites. Many of the metal sites on the small Pt particles of Pts/ γ -Al₂O₃ are likely within close proximity to the γ -Al₂O₃ support on which these condensation products reside. Thus, it is to be expected that molecules adsorbed on the support can reduce the methanol dehydrogenation activity of interfacial sites by both steric hinderance in addition to the possibility of direct binding of these multifunctional surface species to the respective metal sites. The enlargement of Pt particles should alleviate these effects given the greater distribution of coordinated metallic sites distant from the Lewis acidic support.

4.4.4 Possibilities for improving APR catalyst and process robustness

The formation of alkyl groups and dehydrogenation products on supported Pt particles is inevitable given the extensive array of APR reactants. One option could be to incorporate a co-feed of dissolved O₂ for routine catalyst regeneration given that presence of H₂O reduces the activation barrier for oxidation reactions for some surface species including adsorbed CO.²⁰¹⁻²⁰² However So et al. showed that, based on adsorbed CO_L and CO_B band integrals, that Pt/ γ -Al₂O₃ seems to lose APR activity after about 30 min.²⁹ The

need to regenerate Pt catalysts every 30 min severely inhibits the feasibility of APR, especially given that a portion of the produced H_2 would be necessary each occurrence to reduce Pt particles back to a metallic state. In addition, oxidation of surface species would likely be nonselective, resulting in the removal of both alkyl groups and essential APR intermediates. Therefore, adjustments should be made directly to the catalyst design to achieve a material that can passively remove alkyl groups with minimal effects on APR efficiency and H_2 yields.

Ni for instance has demonstrated high APR activity with innate selectivity to light alkanes.²⁸ Trace additions of the metal to Pt particles may prove useful for removing alkyl groups through association with surface hydride species. However in the case of methyl groups, the resulting methane is an undesired product given its reputation as a potent greenhouse gas and the consequential reduction in H_2 yields. On the other hand, oxyphilic promoters may prove capable of oxidizing or reforming surface alkyl groups on a local level without disrupting the intended conversion of APR intermediates. A study by Michalak et al. demonstrated the formation of segregated Pt and Sn domains in a supported PtSn bimetallic catalyst.²⁰³ CO oxidation activity was enhanced due to the Sn domains acting as oxygen reservoirs and the reduction of the activation energy at the Pt-Sn interface (compared to that of CO oxidation on a monometallic Pt catalyst). In the context of APR, a multicomponent catalyst that consists of local oxygen reservoirs that may selectively oxidize alkyl groups into adsorbed CO or light alcohols may prove more practical. This would require further study to ensure that adsorbed CO, or other crucial APR intermediates, are not unintentionally converted.

The results herein have also suggested that mesityl oxide, and potentially other conjugated species formed from aldol condensation on the γ -Al₂O₃ support, may act as strong poisons for both metallic and interfacial Pt sites. Koichumanova et al. utilized IR spectroscopy to study the APR of hydroxyacetone with Pt/ γ -Al₂O₃ and Pt/ZrO₂ catalysts and observed no formation of adsorbed CO.¹⁴⁷ Yet, they addressed the formation of conjugated products from the aldol condensation of hydroxyacetone which may have been responsible for the lack of conversion. However, Justicia et al. reported successful APR of hydroxyacetone into mixtures of H₂, CO₂, and CH₄ using a carbon black-supported Pt catalyst with no mention of conjugated species.²⁰⁴ Because the condensation of di/ketones can be facilitated by the Lewis acid sites of γ -Al₂O₃,¹⁹² the employment of a more inert support should circumvent this side reaction and reduce the extent of Pt poisoning.

4.5 Conclusions

Poisoning of Pt/ γ -Al₂O₃ by strongly binding ketone, diketones, and their fragments is investigated to elucidate the limited efficacy of aqueous phase reforming of these molecules. Using IR spectroscopy, it is shown that the adsorption of various di/ketones and their products can severely poison Pt particles of different sizes as indicated by the hinderance of subsequent methanol dehydrogenation, which normally and readily results in a high coverage of adsorbed carbon monoxide and a strong IR band at 1900 – 2100 cm⁻¹ up to 250 °C. Additional results from density functional theory and inelastic neutron scattering indicate that Pt/ γ -Al₂O₃ catalysts are poisoned by a combination of molecular di/ketones, alkyl groups resulting from di/ketone decarbonylation, and conjugated ketones.

Small Pt particles are highly vulnerable to poisoning by molecular di/ketones due to lesser decarbonylation activity, while their relatively abundant interfacial sites are blocked by conjugated species bound to γ -Al₂O₃ formed from aldol self-condensation of di/ketones. Although larger Pt particles appear more active in di/ketone decarbonylation, modeling of di/ketones adsorbed to Pt(111) suggest that some di/ketones with a thermodynamically stable flat configuration (2,3 butanedione, mesityl oxide) can still resist decarbonylation potentially due to greater adsorptive hapticity and insufficient repulsion between the metal surface and alkyl groups. However, inelastic neutron scattering spectra suggests the presence of alkyl groups from di/ketone decarbonylation (e.g. methyl groups from acetone) on a Pt sponge as high as 250 °C. Calculated reaction energies further imply that the removal of surface methyl groups by associative desorption or partial oxidation is energetically unfavored, and the removal of such species may require catalyst regeneration. The findings and perspectives herein provide potential directions for designing more robust, di/ketone resistant heterogeneous catalysts and progressing efforts to achieve efficient, renewable hydrogen from aqueous phase reforming.

CHAPTER 5. SUMMARY AND RECOMMENDATIONS

5.1 Summary

The overall objective of this project was to better understand the mechanisms and surface chemistry of APR constituent reactions necessary to achieve high yields of renewable hydrogen through the stepwise deconstruction of polyols. Using IR spectroscopy to monitor the adsorption and conversion of select reagents, and therefore formation of adsorbed CO, on various Pt/ γ -Al₂O₃ catalysts has provided much insight to the fundamentals of the dehydrogenation, aldol condensation, and decarbonylation reactions as well as Pt deactivation. The results herein have laid groundwork for improving future catalyst designs and achieving higher APR efficiency.

In Chapter 2, methanol was dehydrogenated on Pt/ γ -Al₂O₃ catalysts with average Pt particle sizes ranging from 1.0 to 4.6 nm. TPD experiments performed up to 450 °C showed larger Pt particles exhibiting larger linearly-adsorbed CO (CO_L) band integrals at lower temperatures. This was further corroborated by isothermal (150 °C) kinetic experiments in which 4.6 nm Pt particles reached equilibrium conversion 30x faster than 1.1 nm particles. The precise CO_L band frequencies observed during initial methanol dehydrogenation on 1.1nm Pt particles even suggested that dehydrogenation will preferentially occur on sites with higher coordination first. The presence of co-adsorbed H₂O only appeared to hinder methanol dehydrogenation on small Pt particles while also promoting the formation of bridging CO (CO_B) species.

In Chapter 3, the surface chemistry of γ -Al₂O₃-adsorbed di/ketones up to 250 °C was deduced by means of spectral deconvolution of the 1500 – 1800 cm⁻¹ region unique for ν (C=O) and ν (C=C) vibrational modes. This was essential to determine prior to Chapter 4 in which γ -Al₂O₃ was utilized as a catalyst support with many of the same di/ketone reagents. While acetone readily converted into mesityl oxide via aldol condensation, the presence of OH groups (di/hydroxyacetone) adjacent to the carbonyl group reduced the extent of aldol condensation due to electronic shielding of the carbonyl group from nucleophilic attacks by surface enols. No trend was established relating surface reaction activity to the intramolecular carbonyl distance of diketones, but rather each diketone (α , β , γ) demonstrated unique chemistry. 2,4 Pentanedione formed a stable mesomeric, chelating surface species similar to the acetylacetate ligand often encountered in coordination chemistry while 2,5 hexanedione readily underwent intramolecular aldol condensation. 2,3 Butanedione gradually enolized and dimerized, either via aldol condensation or carbonyl-olefin metathesis, with increasing temperature while 3,4 hexanedione readily enolized yet resisted subsequent reactions perhaps due to increased thermodynamic stability and steric hindrance of the ethyl group-derived alkene groups. Identification of surface reaction products from di/ketone adsorption on γ -Al₂O₃ served as a necessary prerequisite for better understanding the effects of these species on Pt/ γ -Al₂O₃ catalysts.

Finally, in Chapter 4, the poisoning effects of di/ketones adsorbates on Pt/ γ -Al₂O₃ catalysts with varying Pt particles sizes were studied both experimentally and computationally. Suppression of methanol dehydrogenation, quantified using CO_L band integrals, on small Pt particles were largely due to adsorbed molecular di/ketones and

condensation products, likely poisoning lowly coordinated and interfacial Pt sites, respectively. Larger Pt particles, however, appeared more active in di/ketone decarbonylation with 2,3 butanedione and mesityl oxide still acting as strong poisons. Adsorbate configurations on Pt(111) suggest that these particular di/ketones, which bind flat on the surface with di- σ or π bond characteristics, are able to resist decarbonylation. On the other hand, di/ketones such as acetone and 3,4 hexanedione that bind upright, characteristic of M-O σ bonds, are more likely to decarbonylate due to greater repulsion between the alkyl groups and the metal surface. Yet, INS spectra and binding energy calculations revealed that large Pt particles may still be poisoned by the alkyl groups resulting from di/ketone decarbonylation and their dehydrogenation products (e.g. methyl and methylene groups). These results together insist that advancements must be made in Pt-based catalyst designs to promote adsorption of large polyol reagents by primary alcohol groups or reactions of alkyl groups that result in their desorption. Potential directions for such future work will be discussed later.

5.2 Recommendations for Future Work

5.2.1 Experiments in the Aqueous Phase

One of the key parameters of APR is the presence of a bulk H₂O phase which serves as both a reagent, solvent, and transport medium. On the catalyst surface, co-adsorbed H₂O is an essential intermediate in the water-gas shift reaction, the last constituent reaction of APR. This was even observed by the formation of surface formate species during the co-adsorption of methanol and H₂O on large Pt particles in Chapter 2. However, while

studying the effects of co-adsorbed H₂O proved sufficient for studying inter-adsorbate interactions (solvation or retardation) and charge transfers (CO_L to CO_B transition), the experiments within this work should be repeated under actual APR conditions which consists of a bulk aqueous phase under elevated temperatures and pressures.

There are some studies that have utilized IR spectroscopy to probe surface species during APR of different oxygenates with liquid flow and focus allocated to bands representing adsorbed CO. For instance, So et al. monitored the CO_L band integrals on Pt/ γ -Al₂O₃ during the liquid-phase conversion of glycerol, sorbitol, and glucose at ambient pressure and low temperatures (24 – 72 °C).²⁹ Interpretations of their IR spectra led to the conclusion that the ratio of CO_L and CO_B species on Pt depends on the oxygenate identity and unique corresponding intermediates. Given the very weak CO_B bands during high vacuum experiments herein, the presence of a bulk H₂O phase may result in a similar phenomenon during the adsorption and decarbonylation of di/ketones. The differences seen in the CO_L and CO_B bands could potentially provide additional insight to the mechanism and reaction intermediates of di/ketone decarbonylation necessary to further improve catalyst resistance to poisoning.

Another important clarification would be required regarding the ability of Pt to facilitate APR reactions while in the aqueous phase. A study by Koichumanova et al. included IR spectra that showed the complete absence of a CO_L band during the APR of hydroxyacetone using Pt/ZrO₂ and Pt/AlO(OH) at 30 bar and 230 °C.¹⁴⁷ This suggests that hydroxyacetone decarbonylation does not occur as readily as was seen herein under high vacuum. Ide et al. even reported that mesityl oxide and 2,4 pentanedione acted as strong catalyst poisons during the liquid-phase partial oxidation of 1,6 hexanediol on Pt/C at 70

°C.¹⁸³ Using IR spectroscopy would be a practical approach to confirm the conversion of these species during APR as well. It was theorized herein, with the support of adsorbate configurations and binding energies, that while di/ketones that bind flat on Pt surfaces with di- σ or π bond characteristics, the repulsion between the alkyl groups and metal surfaces drives the decarbonylation reaction. However, the presence of a bulk, polar aqueous phase may introduce repulsion against the nonpolar alkyl chains, thus limiting the catalytic ability of Pt to cleave the C-C bonds. The same experiments with the sequential adsorption of di/ketones and methanol would be of high interest for future work.

5.2.2 *Promotion of Highly Coordinated Metal Sites*

This work demonstrated the greater activity of larger Pt particles in both dehydrogenation and decarbonylation reactions as well as an enhanced resistance to poisoning by molecular di/ketones. While the largest average Pt particle size used in this study was 4.6 nm, it will be important to perform similar experiments on even larger Pt particles to determine when the observed increases in reaction rates will begin to saturate with less dependency on particle size. This will eventually allow researchers to optimize the APR process based on reaction rates and capital costs of catalysts with large Pt particles. Regardless, it is recommended that future studies promote the formation of highly coordinated Pt sites when designing more advanced catalysts.

Large, supported metal particles can be synthesized in a variety of ways. Generally, catalyst reduction temperature and precursor solution pH are parameters that can be altered to tailor the metal particle size of supported catalysts synthesized via wet impregnation or deposition precipitation procedures, respectively.²⁰⁵ Larger metal particles would also

require higher metal loadings. While this may be convenient for laboratory scale research, the use of more Pt to synthesize larger metal particles will decrease Pt dispersion and increase capital costs. One possibility to circumvent this economic challenge may be to synthesize heterogeneous metal particles consisting of Pt shells and cores made from a different metal (e.g. Pt shell and Ni core). This would reduce both capital costs and the quantity of unused, inaccessible Pt. Fortunately, some studies focused on APR have already considered this with the intention of enhancing the activity of Pt. For instance, Dietrich et al. synthesized carbon nanotube-supported PtCo catalysts with up to 30% of particles exhibiting a Pt shell/Co core configuration. They concluded that the Pt shell/Co core particles were the most active in glycerol APR, compared to alloy particles, due to enhancement of water-gas shift or CO desorption activity on the Pt shell by the Co core.²⁰⁶ The use of shell/core metal particles clearly has potential to improve both the economic feasibility and kinetic efficiency of APR. More research is perhaps necessary to test the effects of particle cores made from different metals as well as synthesizing catalysts with higher distributions of these shell/core particles.

5.2.3 Improving Catalyst Tolerance Against Di/Ketones and Alkyl Groups

A number of di/ketones were shown to reduce methanol dehydrogenation activity of Pt/ γ -Al₂O₃ whether by strong binding of the molecular poisons or their decarbonylation fragments. Because larger Pt particles demonstrate higher overall activity in APR constituent reactions, further research should be conducted to improve Pt endurance against di/ketones and alkyl groups.

The strongest di/ketone poisons for large Pt particles were 2,3 butanedione and mesityl oxide, likely due to multiple strong bonds of the multidentate adsorbates and insufficient repulsion between the alkyl groups and the metal surface. Chemistry of 2,3 butanedione on metal surfaces has been seldom studied. One study by Carrara et al. demonstrated the hydrogenation of 2,3 butanedione on Pt/C into 2,3 butanediol.²⁰⁷ However this reaction included organic solvents and hydrogen at high pressures and would be highly unlikely to occur under APR conditions. Fortunately, other separate studies regarding decarbonylation on other metals may provide insight for potential improvements to Pt catalysts. Fundamental mechanistic studies by Houtman and Barteau showed that acetaldehyde decarbonylation, methyl group association with a surface hydrogen, and methane desorption all readily take place on Rh(111).²⁰⁸ In the homogenous catalysis field, the [Rh(COD)Cl]₂ complex was shown to perform a double decarbonylation reaction with alkynyl α -diketones ($R^1-(CO)_2-R^2$) to evolve CO and form R^1-R^2 products. Rh has proven to be active in C-C bond cleavage as well as C-C and C-H bond creation in both heterogeneous and homogenous catalytic applications. By synthesizing Pt catalysts with traces of Rh, or perhaps other suitable metal dopants, on the metal particle surfaces, alkyl group association and desorption could potentially be better facilitated without risk of further alkyl group dehydrogenation and sacrificing decarbonylation activity of the Pt. This particular Pt/Rh combination has yet to be studied for APR applications.

Another viable direction for future work would be to improve the catalytic ability of a Pt-based catalyst to oxidize or even reform surface alkyl groups. This would likely require the adsorption of oxygen to metal particles without altering metallic Pt sites. A study by Michalak et al. demonstrated the segregation of Pt and Sn domains in a PtSn

bimetallic catalyst and the ability for the Sn domains to serve as oxygen reservoirs.²⁰³ In applied experiments, they reported that CO oxidation occurred more readily at the Pt-Sn interface due to an innate reduction of the activation barrier in comparison to that of the same reaction on metallic Pt sites. In regards to APR and the issue of strong binding methyl groups, the employment of local oxygen reservoirs may show potential for oxidizing or reforming methyl groups into CO₂ or methanol, respectively, thus liberating previously deactivated sites. However, extensive research may be required for improving the selectivity of local oxygen reservoirs of bimetallic catalysts for converting surface alkyl groups rather than adsorbed CO given its importance as an APR intermediate.

5.2.4 *Alternative Catalyst Supports*

Another topic to be addressed in future work is the impact of an alternative support for Pt particles. Numerous materials have been tested for APR catalyst supports.¹⁵ γ -Al₂O₃ in particular was employed herein due to its compatibility with IR spectroscopy, adsorption capacity, and retainment narrow particle size distributions at the studied temperatures due to strong metal-support interactions.²⁰⁹ However, this work along with that of other studies suggest that γ -Al₂O₃ may not be a practical choice support for a commercial APR process.

Characterization data in Chapter 2 showed adsorption sites of γ -Al₂O₃ to be highly Lewis acidic. Chapter 3 revealed these same sites to be responsible for the adsorption of di/ketones and their subsequent conversion into higher molecular weight conjugated products by aldol condensation. It was concluded herein that these conjugated products may play a role in poisoning interfacial metal sites due to their proximity to the support. In addition, as observed in the case of mesityl oxide, if these conjugated species were to

migrate to Pt terraces, highly coordinated metal sites also can be poisoned by these multidentate adsorbates. Therefore, it may be of interest to minimize the presence of conjugated species in APR and employ a support that is less active in the production of these catalyst poisons.

A study by Ravenelle et al. showed that γ -Al₂O₃ will undergo a phase transition into boehmite, AlO(OH), under APR conditions.⁹¹ This new phase is characteristic of severely reduced Lewis acidity and surface area as well as promoted sintering of supported metal particles which in turn would decrease Pt dispersion. Other previous studies have demonstrated increased stability of the γ -Al₂O₃ supporting by forming protective adlayers comprised of polyols or alkyl phosphonates.²¹⁰⁻²¹¹ It was also theorized in Chapter 3 that stable adsorbates derived from di/ketones, such as 2,4 pentanedione, may also exhibit such potential. However, improved convenience and feasibility, it may be of higher interest to utilize a more chemically inert and hydrothermally stable catalyst support for commercial APR processes. Some candidate materials may include carbon black or Mg-based oxides.²¹²

APPENDIX A. SUPPLEMENTARY INFORMATION FOR CHAPTER 2

A.1 Lewis Acid Site Concentrations

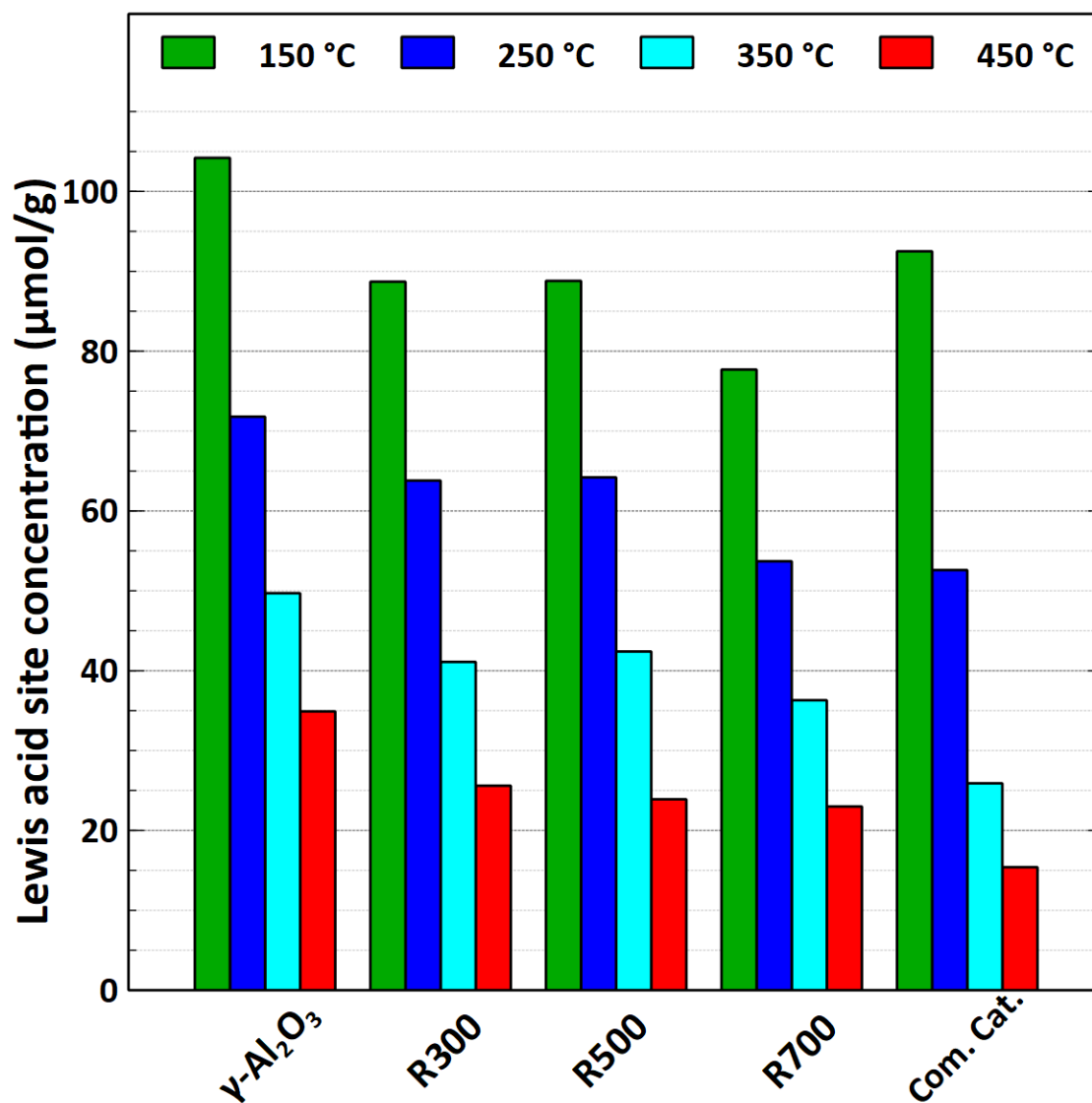


Figure A1. Lewis acidity of $\gamma\text{-Al}_2\text{O}_3$, synthesized Pt/ $\gamma\text{-Al}_2\text{O}_3$ samples, and the commercial obtained Pt/ $\gamma\text{-Al}_2\text{O}_3$ catalyst.

A.2 Methanol-derived Surface Species on γ -Al₂O₃

Methanol adsorption on γ -Al₂O₃ has been extensively studied with focus allocated towards the species formed and molecular distinctions from free methanol vapor. Numerous species have been proposed including surface methoxides,²¹³⁻²¹⁴ alkoxides,²¹⁵ to a whole collection of both weakly physisorbed and dissociatively chemisorbed species with temperature dependence.^{49, 216-217} The general consensus regarding dissociative adsorption, however, seems to encompass the formation of a methoxy surface intermediate on Lewis acid sites following cleavage of the OH bond.¹⁶³ The vibrational modes acquired from methanol adsorption on γ -Al₂O₃ in this study (**Figure A2**) echo that of Busca et. al.⁴⁹ For instance, the OH stretching band owes much of its broadness to the presence of undissociated methanol that is hydrogen bonded to Lewis base sites (surface Al hydroxyls). This species was apparently removed at 350 °C under UHV. Methanol may also develop a stronger bond to Lewis acid sites (exposed Al³⁺) and resonate between 1- and 2-fold denticity via the hydroxyl oxygen. At elevated temperatures, the bidentate form typically dissociates by donating a proton to the adjacent site, creating a methoxy species that is covalently bonded to γ -Al₂O₃. Provided a proximal base site, the donated hydrogen will be accepted by a surface hydroxyl and result in observable H₂O desorption.^{163, 218} Preliminary exposure to H₂O, as in APR, is expected to reduce the extent of methanol chemisorption due to the universal distribution of surface hydroxyl groups that block the aforementioned acid sites.

The vibrational frequencies of methanol adsorbed on γ -Al₂O₃ appear somewhat different than that of its free vapor counterpart.²¹⁹⁻²²⁰ The C-H stretching bands, namely $\nu_{as} = 2940\text{ cm}^{-1}$ and $\nu_s = 2818\text{ cm}^{-1}$, appear about 20 – 30 cm^{-1} than what one would expect for

methanol vapor. This is likely due to enhanced back donation from the hydroxyl oxygen lone pairs to the C-H antibonding orbitals within stabilized methoxy species, a phenomenon known as the trans lone pair effect.²²¹ The single bond CO stretching frequencies appear much higher than the expected 1034 cm^{-1} . With the loss of the hydroxyl hydrogen, the resulting methoxy species exhibits a shorter CO bond which is inclined to approach the stretching frequencies of carbonyls.¹⁶³ The 1595 and 1395 cm^{-1} bands introduced at $350\text{ }^{\circ}\text{C}$ is a result of asymmetric and symmetric O-C-O stretching within a formate surface species produced at high temperatures.^{49, 60, 213, 222-223} The formate bands enlarge at $450\text{ }^{\circ}\text{C}$ and suggest decomposition of methoxy intermediates in contact with surface oxygen to form these strongly bond species that would other not be expected at the lower temperatures and conditions of APR.

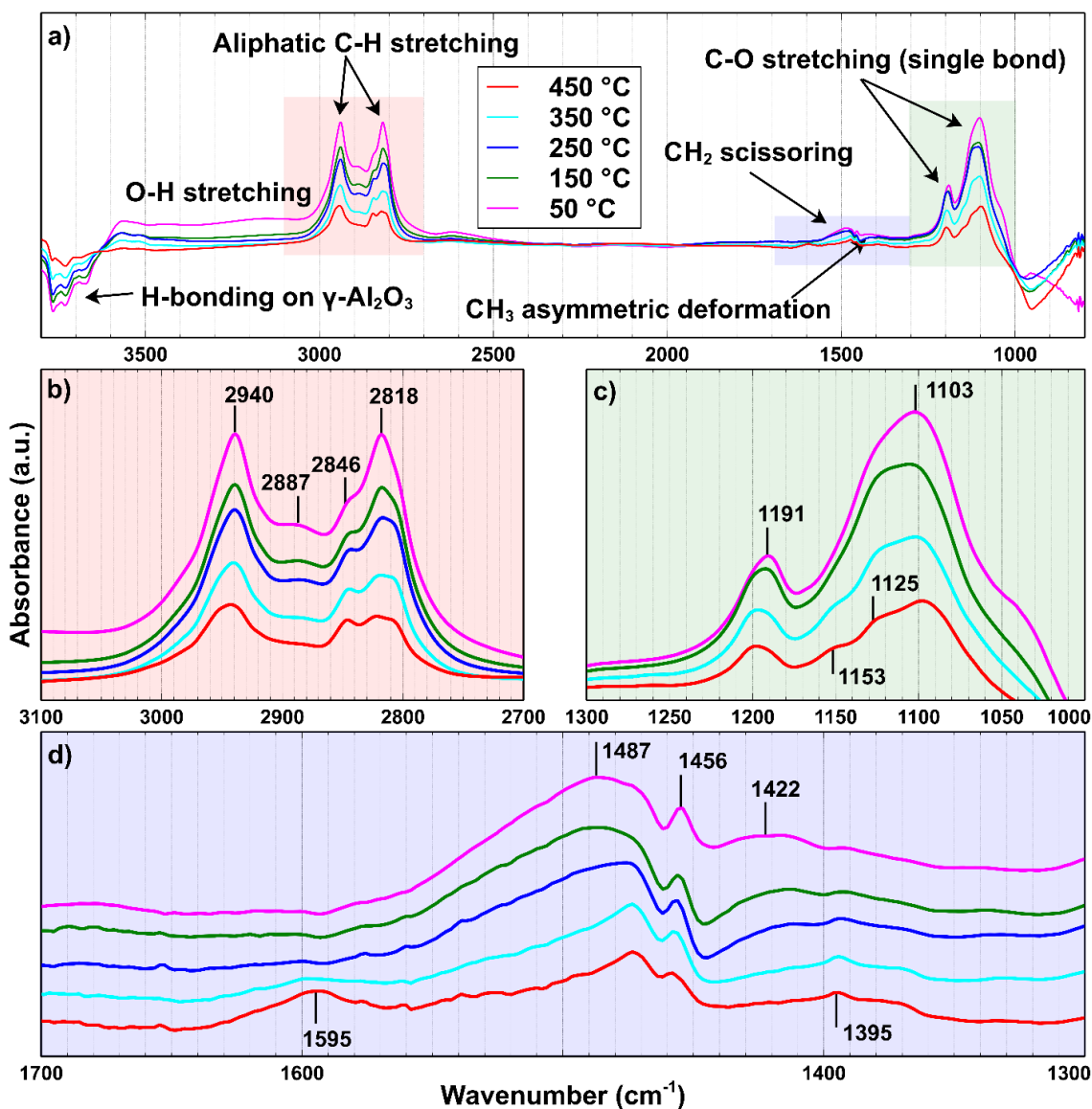


Figure A2. a) Full infrared spectrum of methanol adsorption on γ - Al_2O_3 at various temperatures. Cropped portions contain the b) C-H stretching, c) C-O single bond stretching, and d) C-H bending with the emergence of a couple weak surrounding bands.

A minute presence of Cl is known to increase the Lewis acidity of γ - Al_2O_3 , even under vacuum at elevated temperatures.²²⁴⁻²²⁵ Initially, the chlorine adsorption is depicted by the diminishment of a small OH band at 3767 cm^{-1} (**Figure A3**) which suggests the process is site-selective.²²⁶ The lower frequency hydroxyl bands located at 3728, 3673, and 3584 cm^{-1} were each maintained during chlorination. When observing methanol

adsorption, the spectra for chlorinated γ -Al₂O₃ is predominantly mirrored by that of clean γ -Al₂O₃. Frederick et al. have contemplated the role of chlorine in stabilizing methoxy species by enhancing the Lewis acidity of Al₂O₃ and obstructing oxidation into formate species.²²⁷ Chlorine is expected to desorb in the form of HCl.²²⁸ This is likely initiated by surface protons resulting from reduction by hydrogen gas or the dissociative adsorption of methanol on γ -Al₂O₃. One considerable difference in the IR spectra is the introduction of a relatively weak, yet very broad band centered at $\sim 1840\text{ cm}^{-1}$ first noted at 350 °C (**Figure A3**). We believe this to be halogenated oxygenates produced from reactions with chlorine and formate surface species.

A.3 Effects of Chlorine

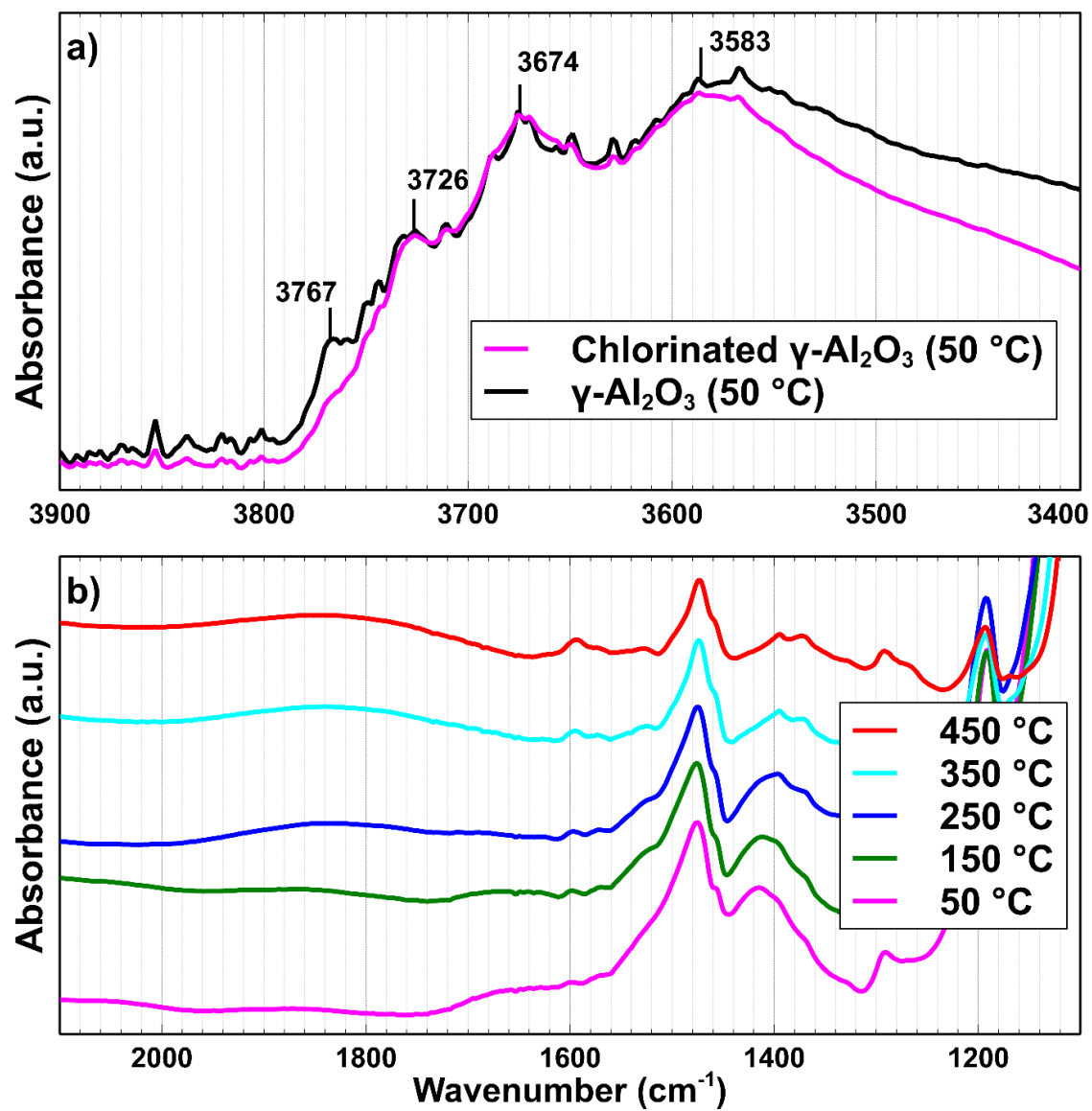


Figure A3. a) Residual OH stretching modes on activated $\gamma\text{-Al}_2\text{O}_3$ and b) the low-frequency IR regime of adsorbed methanol on chlorinated $\gamma\text{-Al}_2\text{O}_3$ at different temperatures. Note the emergence of a broad feature at $\sim 1840\text{ cm}^{-1}$.

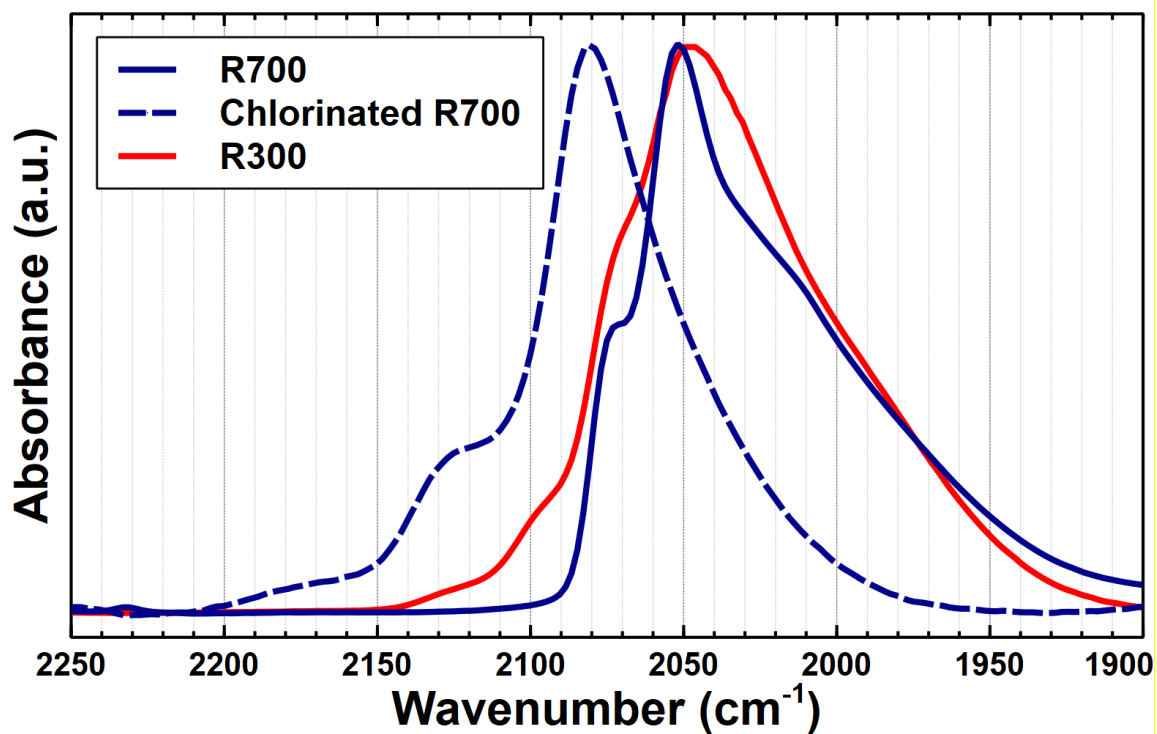


Figure A4. Effect of Cl on the CO_L stretching bands after impregnation with HCl to achieve 5 wt. % Cl.

A.4 H₂O Adsorption

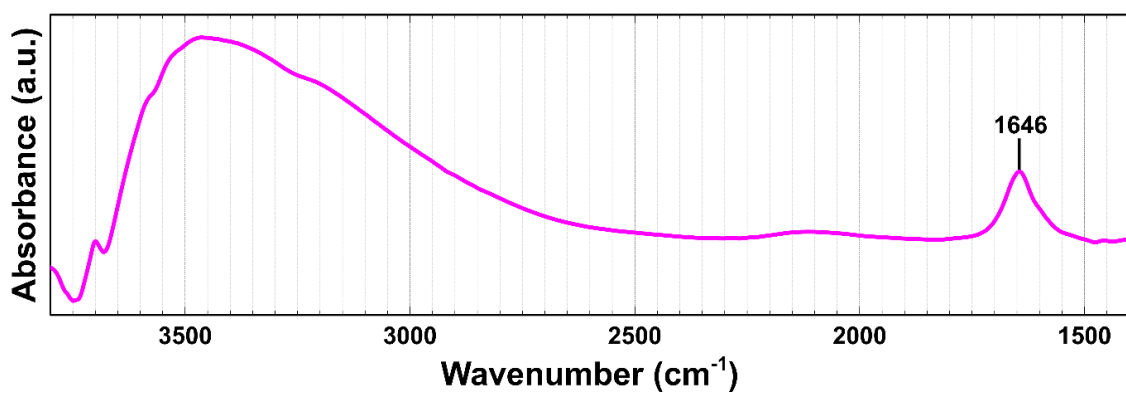


Figure A5. IR spectrum of surface species following exposure of R700 to 0.5 mbar H₂O vapor at 50 °C.

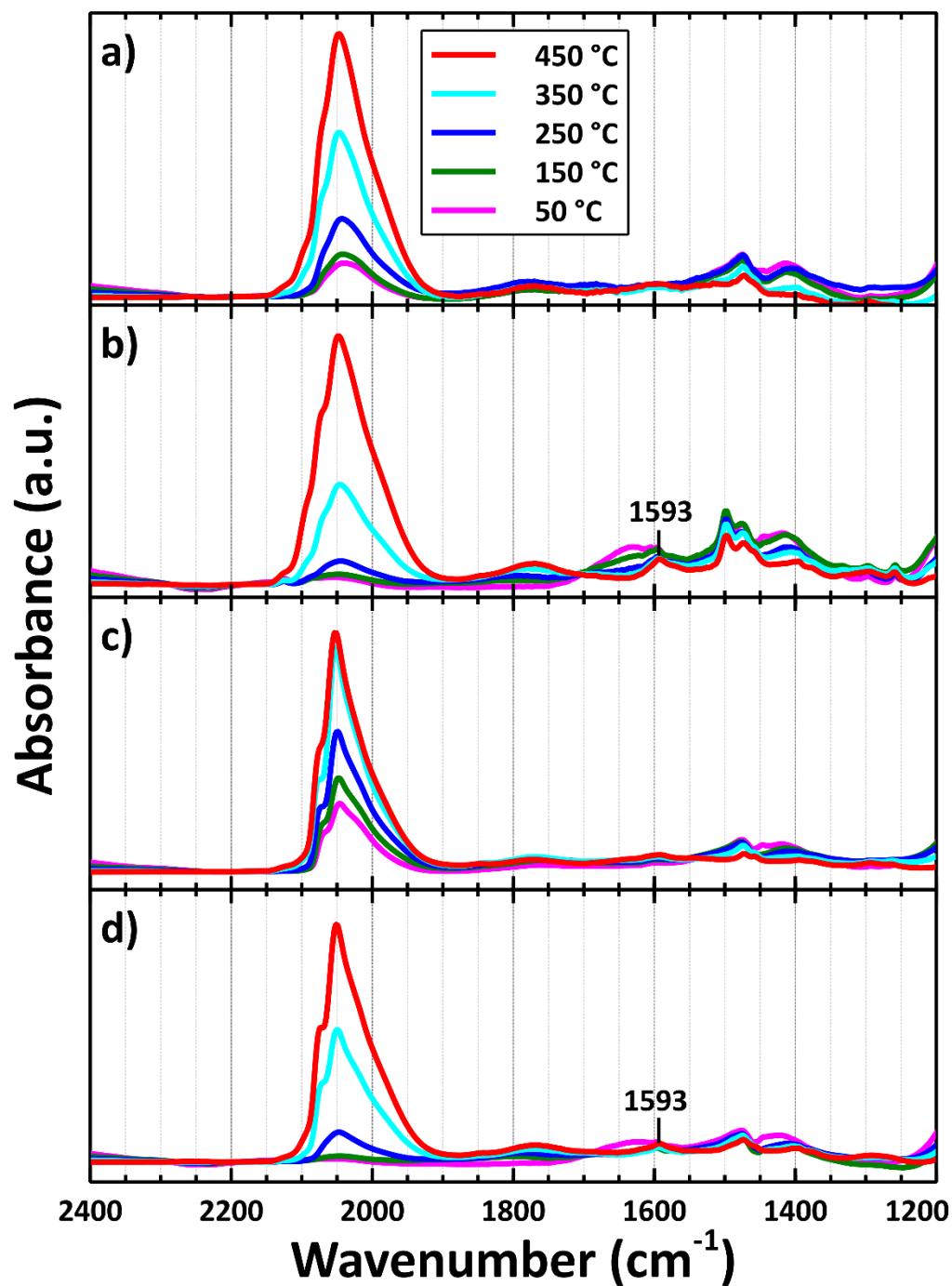


Figure A6. IR spectra of temperature-programmed methanol dehydrogenation on 1% Pt/ γ -Al₂O₃ catalysts. **a)** Methanol on R300, **b)** methanol/H₂O on R300, **c)** methanol on R500, and **d)** methanol/H₂O on R500.

APPENDIX B. SUPPLEMENTARY INFORMATION FOR CHAPTER 3

B.1 DFT Cells

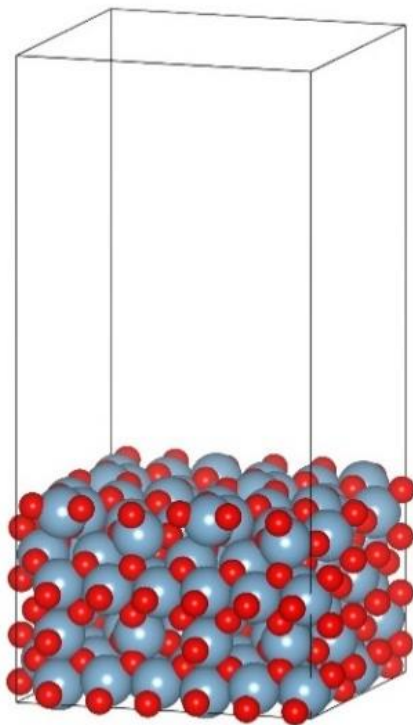


Figure B1. The simulation supercell for the clean γ -Al₂O₃. Used by collaborators at Clemson University.

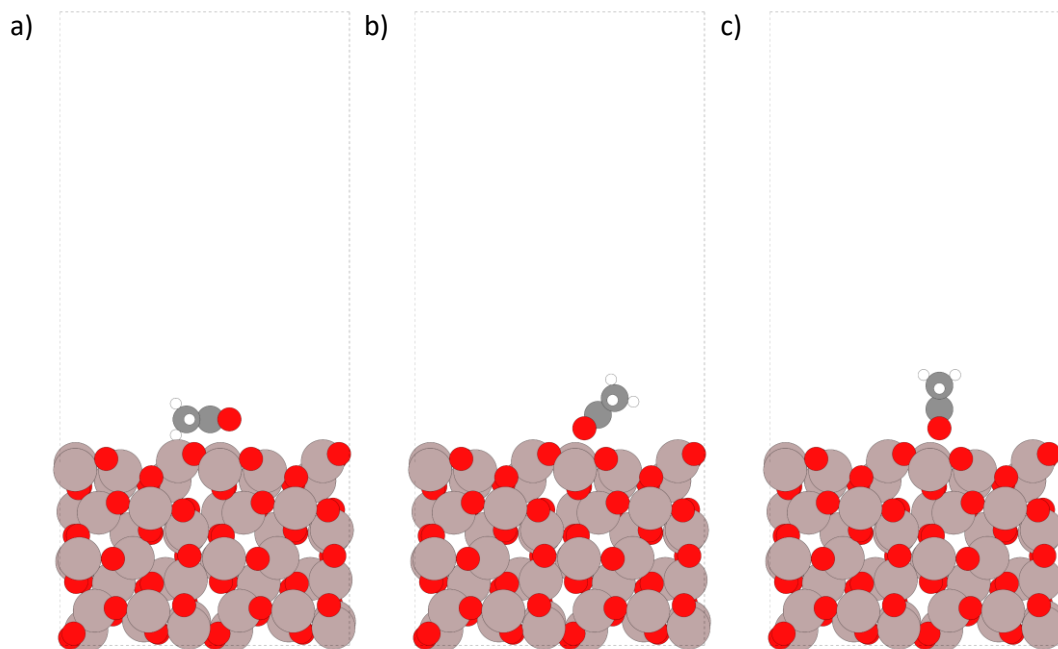


Figure B2. Different adsorbate orientations. a) Horizontal b) Tilted c) Vertical. Tested by collaborators at Clemson University.

B.2 IR Spectra of Vapor Phase Di/Ketones

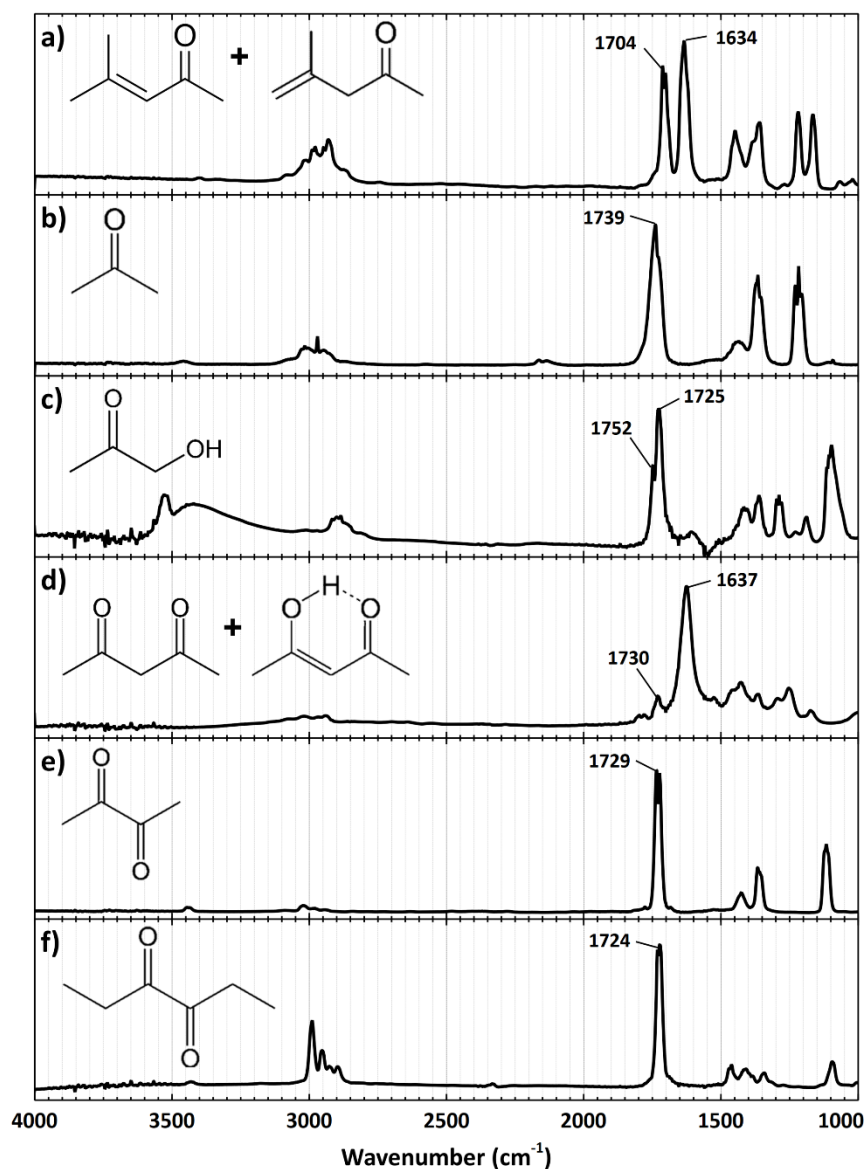


Figure B3. Infrared spectra of vapor-phase **a)** mesityl oxide (10 mbar, includes isomesityl isomer), **b)** acetone (7 mbar), **c)** hydroxyacetone (6 mbar), **d)** 2,4 pentanedione (10 mbar, includes enol tautomer), **e)** 2,3 butanedione (10 mbar), and **f)** 3,4 hexanedione (8 mbar).

Table B1. Infrared band assignments for vapor-phase di/ketones. Frequencies correspond to bands displayed in Figure B3. Assignments were based on references included.

| Mesityl Oxide | | Acetone | | Hydroxyacetone | | 2,4 Pentanedione | | 2,3 Butanedione | | 3,4 Hexanedione | |
|---------------|-------------------------------|---------|--------------------------|----------------|--|------------------|------------------------------|-----------------|-------------------------------|-----------------|-----------------------------|
| Freq. | Vib. Mode ^{141, 143} | Freq. | Vib. Mode ²²⁹ | Freq. | Vib. Mode ²³⁰⁻²³¹ | Freq. | Vib. Mode ²³² | Freq. | Vib. Mode ^{157, 233} | Freq. | Vib. Mode |
| | | | | | | 1788 | ? | | | | |
| | v(C=O) | | | 1752 | v(C=O) | | | | | | |
| 1742 | | 1739 | v(C=O) | | | | | | | | |
| | | | | | | 1730 | v(C=O) (keto) | 1729 | v(C=O) | | |
| | | | | 1725 | | | | | | 1724 | v(C=O) |
| 1714 | | | | | | | | | | | |
| 1704 | | | | | | | | | | | |
| 1634 | v(C=C) | | | | | 1637 | v(C=O) (enol) | | | | |
| | | | | | | 1625 | v(C=O) + δ (OH) | | | | |
| 1555 | | | | | | | | | | | |
| | | 1532 | ? | | | 1533 | ? | | | | |
| 1505 | | | | | | | | | | | |
| | δ (CH) | | | | | 1465 | ? | | | 1468 | δ (CH ₂) |
| 1448 | | | | | | | | | | 1457 | |
| | | 1435 | δ (CH) | 1437 | δ (CH) | | | | | | |
| 1423 | | | | | | 1425 | δ (CH) + v(CCH) | 1426 | $\delta_{As}(\text{CH}_3)$ | | |
| | | | | 1409 | | | | | | 1413 | $\delta_{As}(\text{CH}_3)$ |
| 1378 | | 1375 | | | | | | | | 1382 | |
| | | | | | | | | 1368 | $\delta_s(\text{CH}_3)$ | | |
| 1358 | | 1356 | | 1362 | | 1366 | $\delta_s(\text{CH}_3)$ | 1358 | | | |
| | | | | | | | | 1348 | | 1344 | $\delta_s(\text{CH}_3)$ |
| | | | | | | | | | | 1315 | |
| | | | | | | | | | | | |
| | | | | 1298 | $\delta_s(\text{CCH})$ / $\delta(\text{COH})$ | 1296 | ? | | | | |
| | | | | 1288 | | | | | | | |
| | | | | 1280 | | | | | | | |
| 1265 | v(C-C) | | | | | | | | | | |
| | | | | | | 1248 | $\nu_s(\text{C-C}=\text{C})$ | | | | |
| | | 1231 | $\nu_{As}(\text{C-C})$ | 1230 | $\delta_{As}(\text{CCH})$ / $\delta(\text{COH})$ | | | | | | |
| 1218 | | 1217 | | | | | | | | | |
| | | 1204 | | 1190 | $\nu_{As}(\text{C-C})$ | | | | | | |
| | | | | | | 1176 | $\delta(\text{CH})$ (enol) | | | | |
| 1165 | | | | | | | | | | | |
| | | | | | | | | 1125 | $\rho(\text{CH}_3)$ | | |
| | | | | 1115 | v(C-O) | | | 1115 | | | |
| | | | | 1107 | | | | 1105 | | 1109 | $\rho(\text{CH}_3)$ |
| | | 1098 | $\delta(\text{CCH})$ | 1098 | | | | | | 1097 | |
| 1066 | $\rho(\text{CH}_3)$ | | | 1075 | $\delta(\text{CCH})$ | | | | | 1087 | |
| 1023 | | | | | | | | | | | |
| | | | | | | | | | | | |

B.3 Full IR Spectra of Adsorbed Di/Ketones

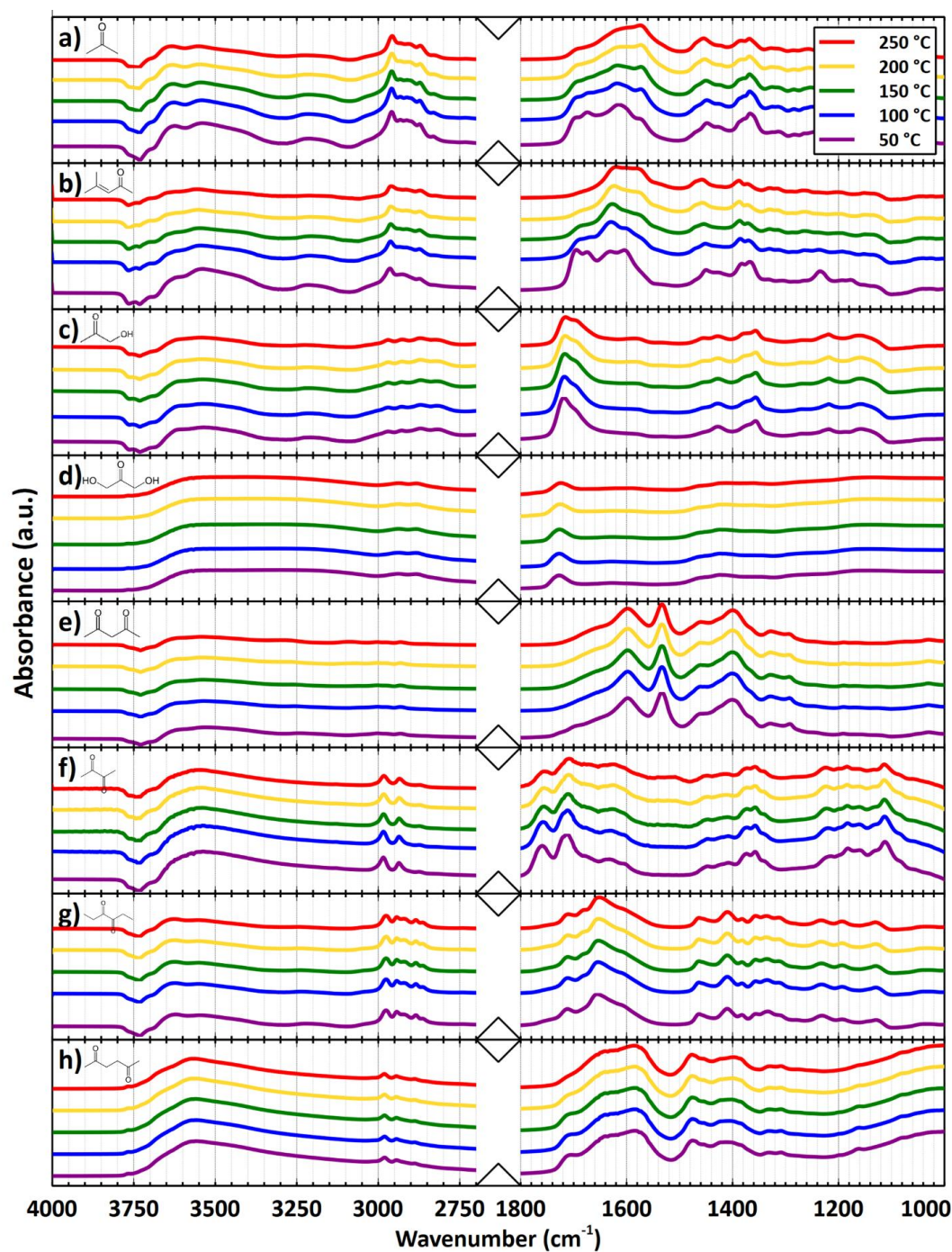


Figure B4. Full IR spectra of γ -Al₂O₃-adsorbed **a)** acetone, **b)** mesityl oxide, **c)** hydroxyacetone, **d)** dihydroxyacetone (γ -Al₂O₃ not subtracted), **e)** 2,4 pentanedione, **f)** 2,3 butanedione, **g)** 3,4 hexanedione, and **h)** 2,5 hexanedione (γ -Al₂O₃ not subtracted).

B.4 Supplementary IR Spectra

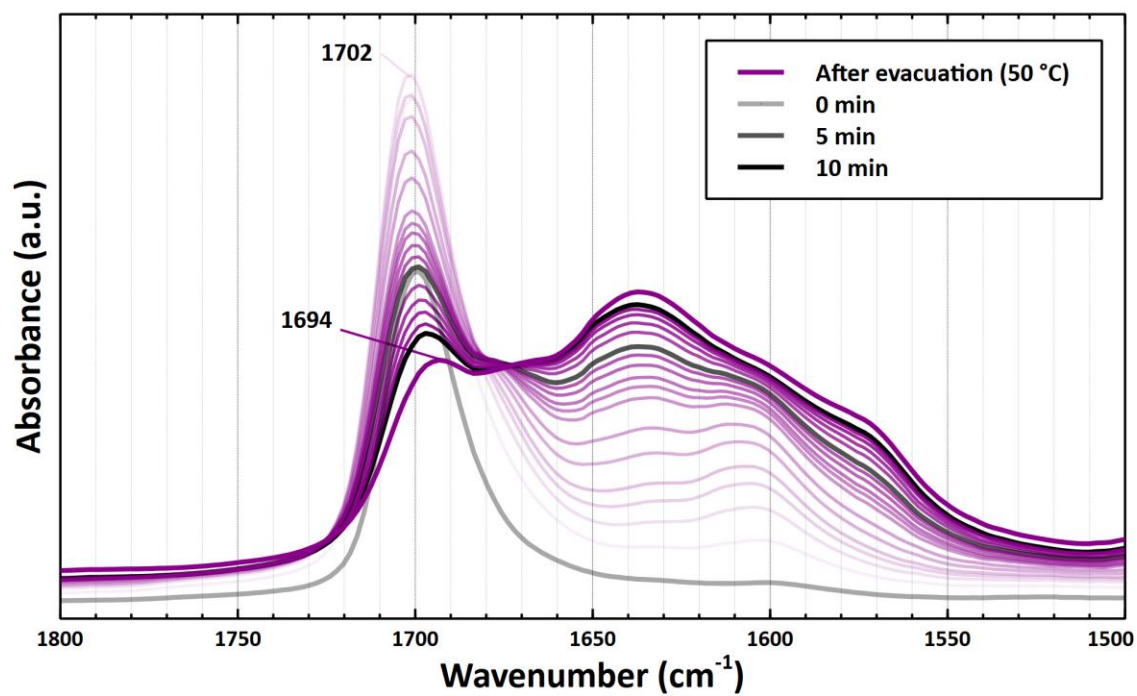


Figure B5. IR spectra of acetone adsorption and conversion kinetics on γ -Al₂O₃ at 50 °C; mid-frequency region.

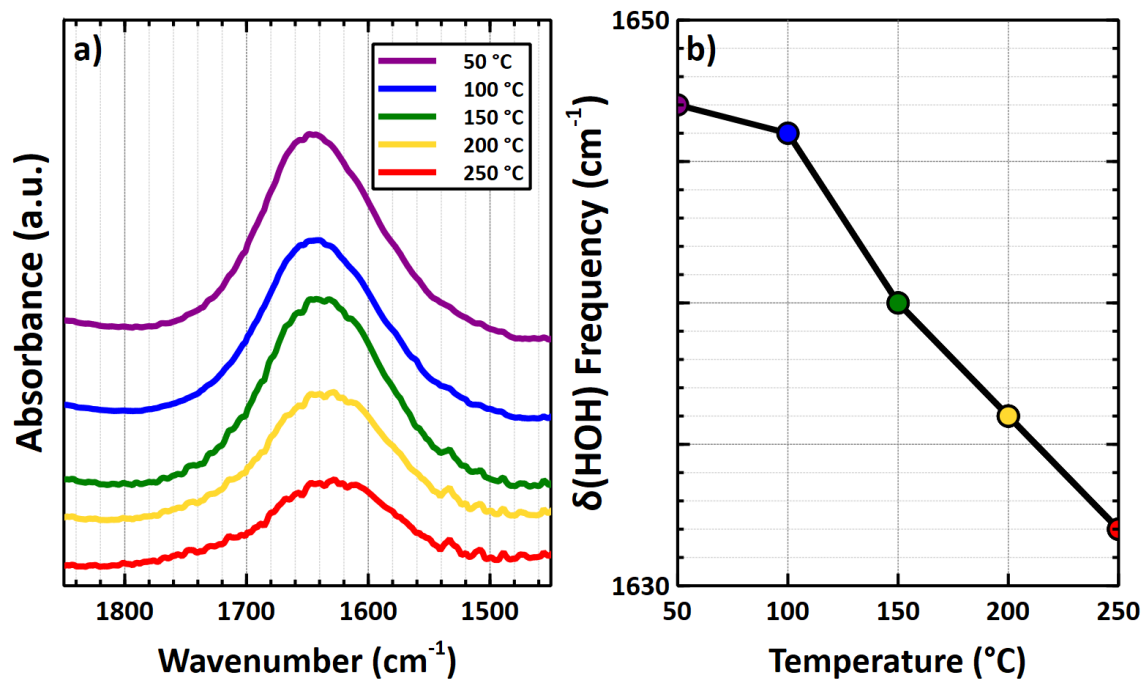


Figure B6. IR spectra of TPD of adsorbed H₂O on γ -Al₂O₃.

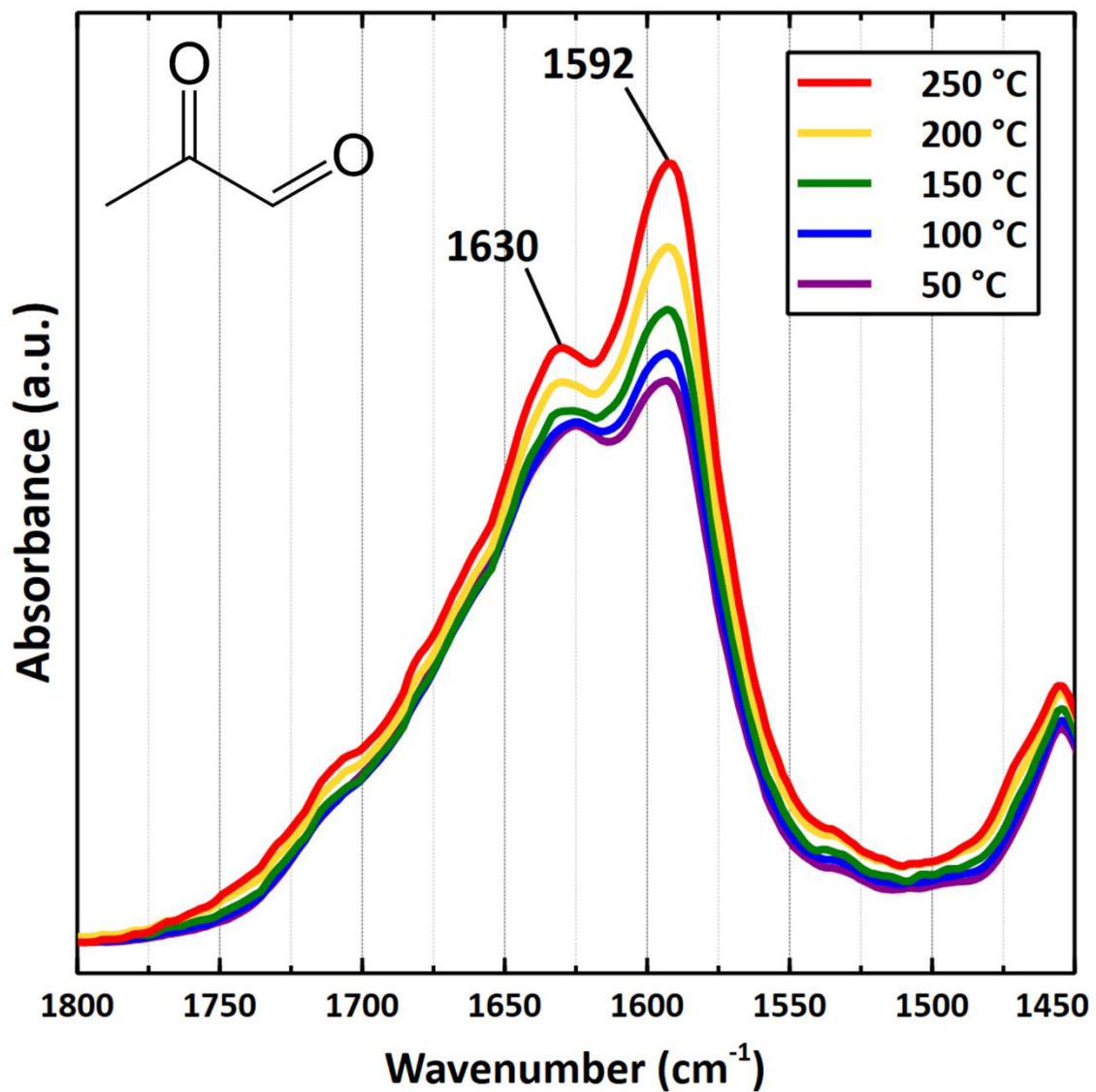


Figure B7. Infrared spectra ($\nu(\text{C}=\text{O})$ region) of $\gamma\text{-Al}_2\text{O}_3$ -adsorbed pyruvaldehyde during TPD experiments from 50 to 250 °C.

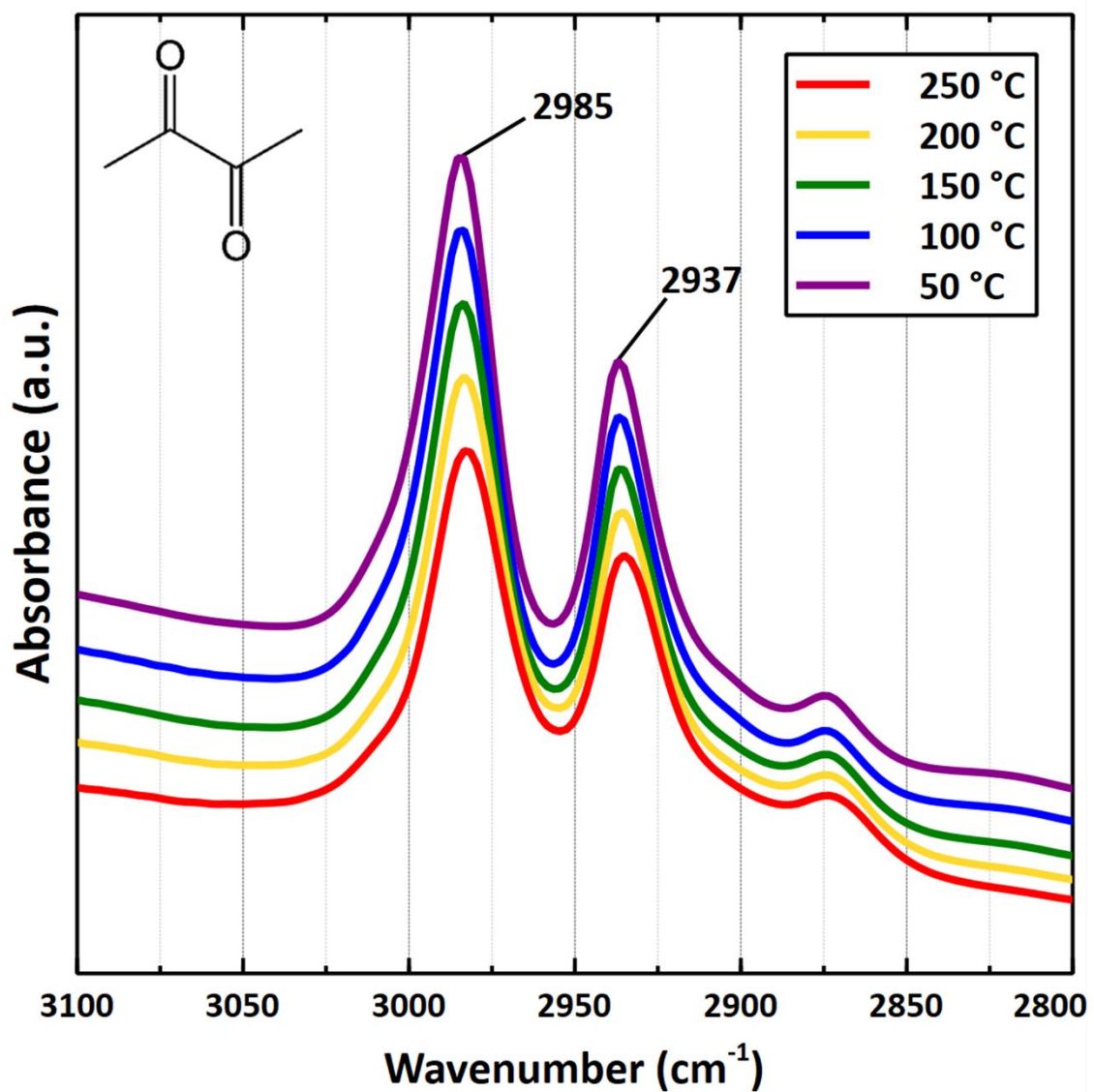


Figure B8. Infrared spectra ($\nu(\text{C-H})$ region) of $\gamma\text{-Al}_2\text{O}_3$ -adsorbed 2,3 butanedione during TPD experiments from 50 to 250 °C.

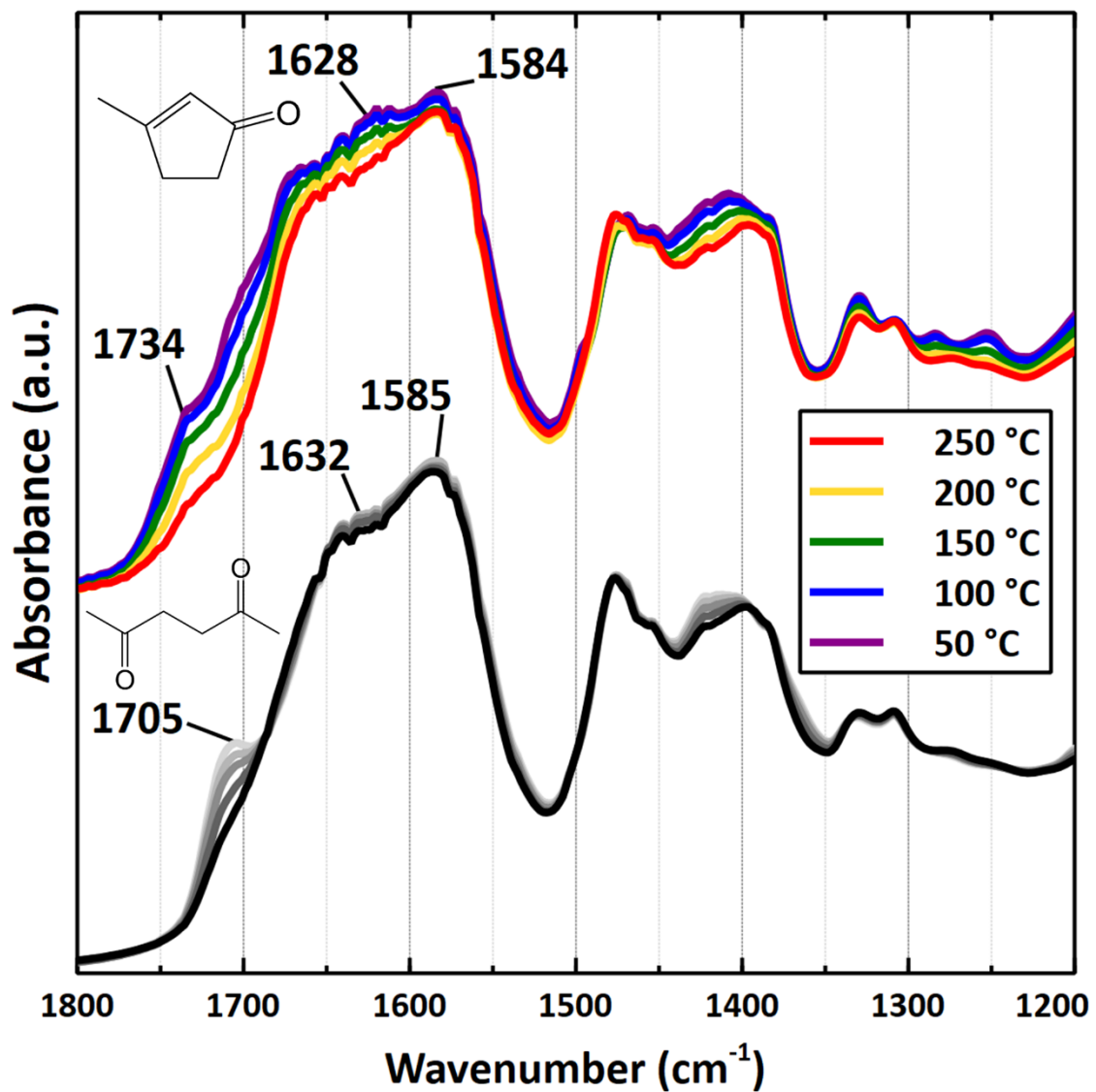


Figure B9. Infrared spectra ($\nu(\text{C}=\text{O})$ region) of $\gamma\text{-Al}_2\text{O}_3$ -adsorbed 3-methylcyclopent-2-en-1-one (prepared via ex-situ impregnation) during TPD experiments from 50 to 250 °C. The IR spectra from the same experiment with 2,5 hexanedione is shown in gray/black for direct comparison.

B.5 Supplementary DFT Calculations

Table B2. Geometrical parameters of γ -Al₂O₃-adsorbed acetone and diketones.

| Adsorbate | Al-O Distance (Å) | Al-O=C Angle (°) |
|------------------|-------------------|------------------|
| Acetone | 1.90 | 124 |
| 2,4 Pentanedione | 1.92 | 116 |
| 2,3 Butanedione | 1.95 | 129 |
| 3,4 Hexanedione | 1.91 | 122 |
| 2,5 Hexanedione | 1.85 | 154 |

Table B3. DFT-calculated binding energies for γ -Al₂O₃-adsorbed diketones, relative to that of acetone.

| Adsorbate | Site geometry | E _{Relative Binding} (eV) |
|------------------|---------------|------------------------------------|
| Acetone | Tetrahedral | 0.00 |
| 2,3 Butanedione | Tetrahedral | 0.51 |
| | Octahedral | 0.44 |
| 2,4 Pentanedione | Tetrahedral | -0.64 |
| | Octahedral | 0.33 |
| 3,4 Hexanedione | Tetrahedral | 0.26 |
| | Octahedral | 0.64 |
| 2,5 Hexanedione | Tetrahedral | -0.26 |
| | Octahedral | 0.37 |

APPENDIX C. SUPPLEMENTARY INFORMATION FOR CHAPTER 4

C.1 DFT Cells

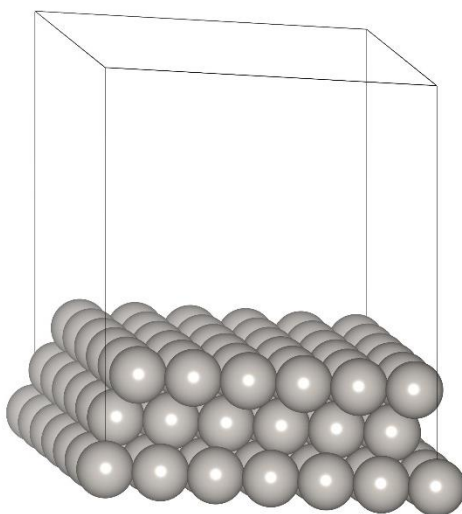


Figure C1. DFT simulation supercell for Pt(111). Used by collaborators at Clemson University.

C.2 Full IR Spectra of Adsorbed Di/Ketones

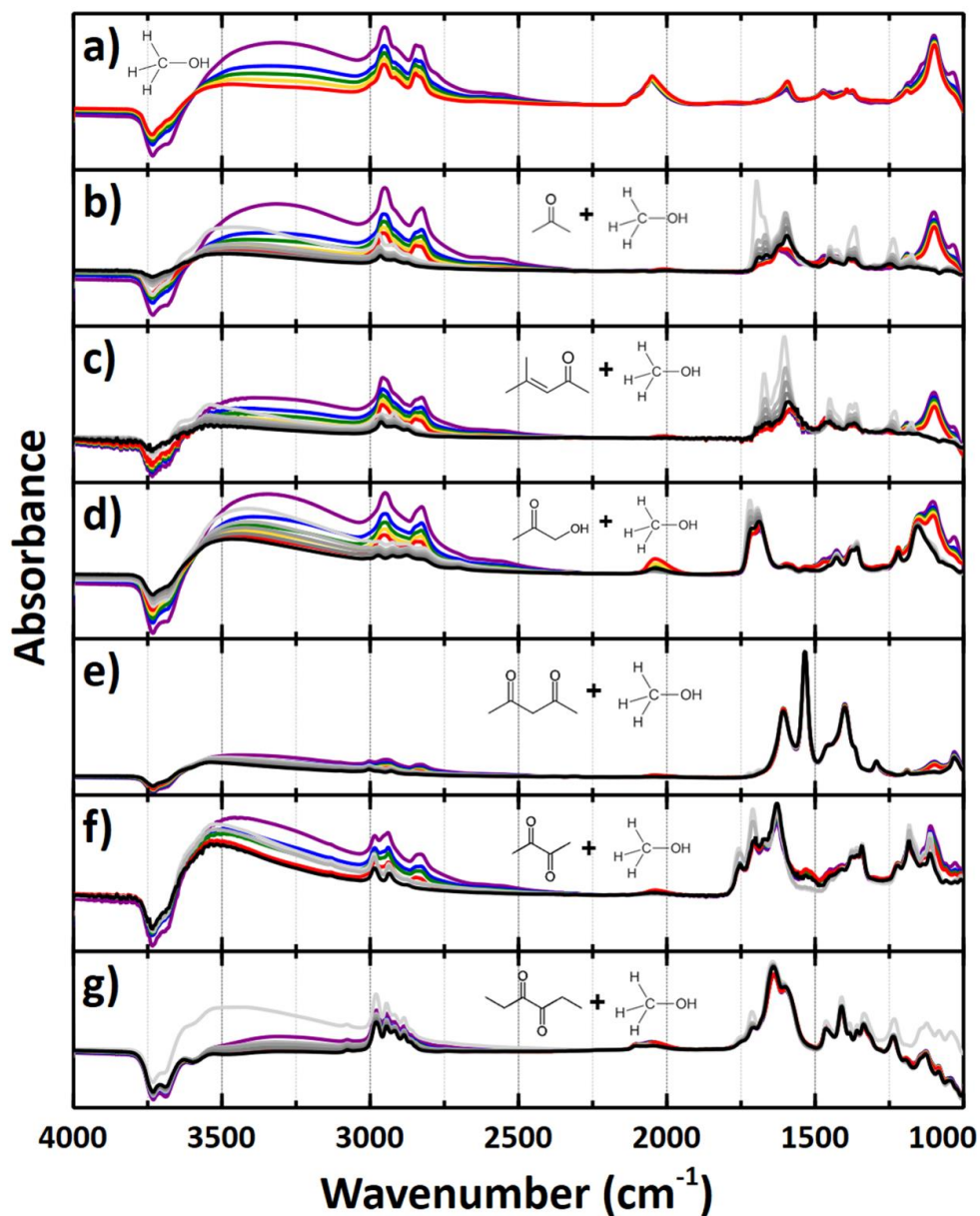


Figure C2. Full IR spectra during TPD experiments with $\text{Pt}/\gamma\text{-Al}_2\text{O}_3$ (~1.1 nm Pt particles) up to 250 °C. **a)** Methanol TPD on clean $\text{Pt}/\gamma\text{-Al}_2\text{O}_3$. Methanol TPDs following poison TPDs in which the poison is **b)** acetone, **c)** mesityl oxide, **d)** hydroxyacetone, **e)** 2,4 pentanedione, **f)** 2,3 butanedione, and **g)** 3,4 hexanedione.

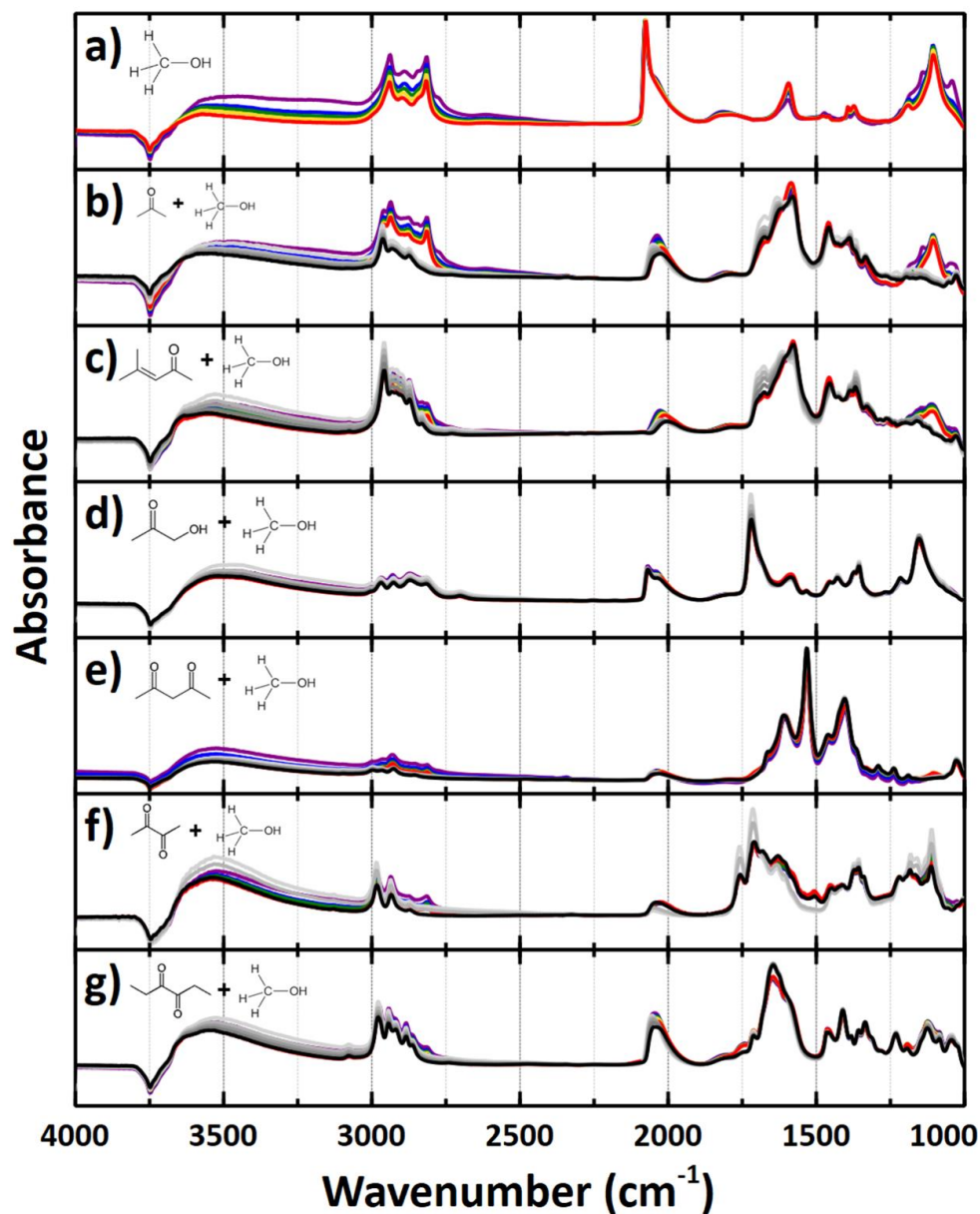


Figure C3. Full IR spectra during TPD experiments with $\text{Pt}_L/\gamma\text{-Al}_2\text{O}_3$ (~4.6 nm Pt particles) up to 250 °C. **a)** Methanol TPD on clean $\text{Pt}_L/\gamma\text{-Al}_2\text{O}_3$. Methanol TPDs following poison TPDs in which the poison is **b)** acetone, **c)** mesityl oxide, **d)** hydroxyacetone, **e)** 2,4 pentanedione, **f)** 2,3 butanedione, and **g)** 3,4 hexanedione.

C.3 INS Spectra of Di/Ketones

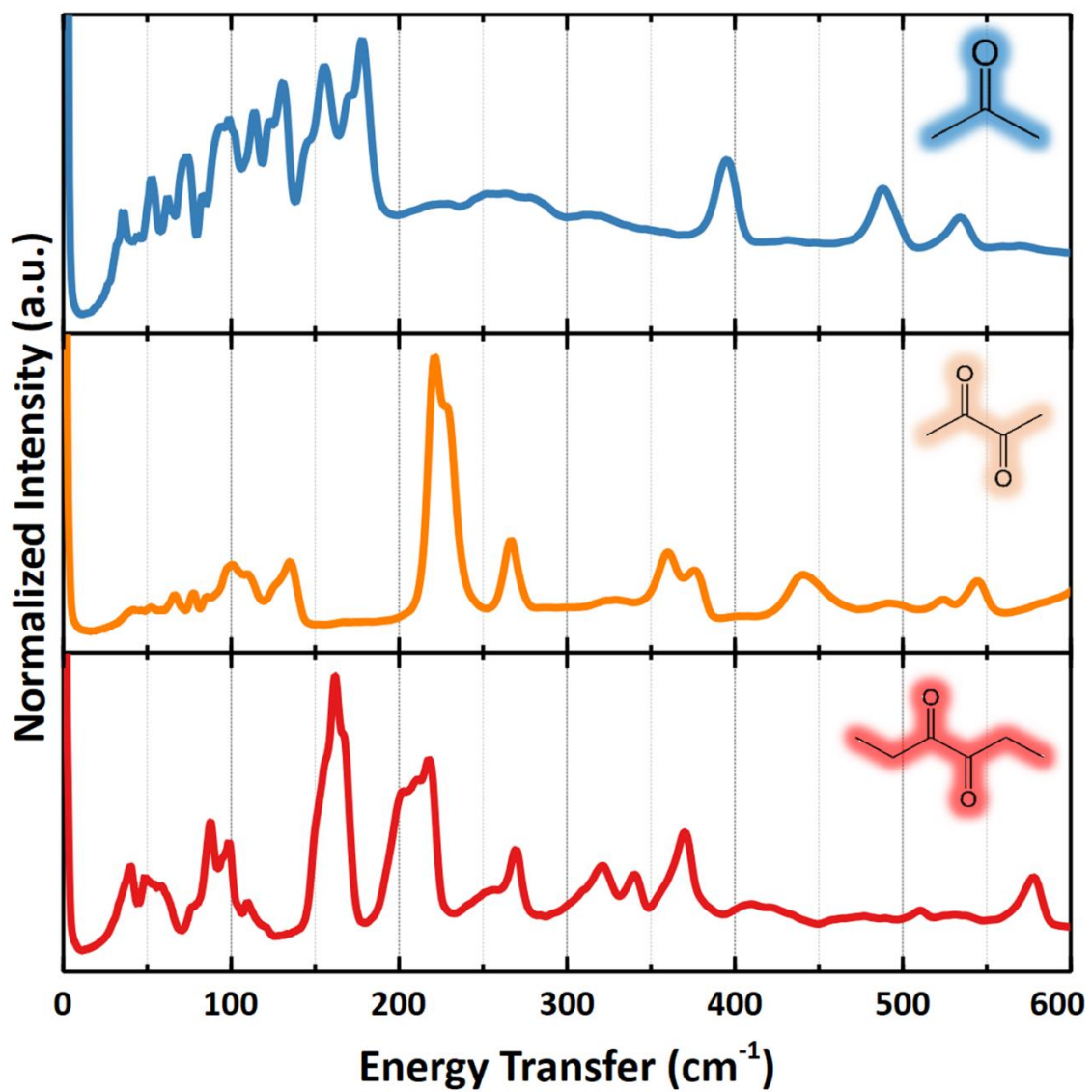


Figure C4. Reference inelastic neutron scattering spectra for some free di/ketone reagents. Data obtained by collaborators at the Oak Ridge National Laboratory.

REFERENCES

1. Winter, C.-J., Hydrogen energy—Abundant, efficient, clean: A debate over the energy-system-of-change. *Int. J. Hydrogen Energy* **2009**, *34*, S1-S52.
2. Veziroğlu, T. N.; Şahi, S., 21st Century's energy: Hydrogen energy system. *Energy Convers. Manage.* **2008**, *49*, 1820-1831.
3. Piemonte, V.; Capocelli, M.; Orticello, G.; Di Paola, L., Bio-oil production and upgrading: New challenges for membrane applications. In *Membrane Technologies for Biorefining*, Elsevier: 2016; pp 263-287.
4. Tanabe, Y.; Nishibayashi, Y., Developing more sustainable processes for ammonia synthesis. *Coord. Chem. Rev.* **2013**, *257*, 2551-2564.
5. Krylova, A. Y., Products of the Fischer-Tropsch synthesis (A Review). *Solid Fuel Chem.* **2014**, *48*, 22-35.
6. Taibi, E.; Miranda, R.; Vanhoudt, W.; Winkel, T.; Lanoix, J.-C.; Barth, F., Hydrogen From Renewable Power: Technology Outlook for the Energy Transition. Agency, I. R. E., Ed. Abu Dhabi, 2018.
7. Balat, H.; Kırtay, E., Hydrogen from biomass—present scenario and future prospects. *Int. J. Hydrogen Energy* **2010**, *35*, 7416-7426.
8. Huber, G. W.; Iborra, S.; Corma, A., Synthesis of Transportation Fuels from Biomass: Chemistry, Catalysts, and Engineering. **2006**, *106*, 4044-4098.
9. Kırtay, E., Recent advances in production of hydrogen from biomass. *Energy Convers. Manage.* **2011**, *52*, 1778-1789.
10. Cortright, R. D.; Davda, R. R.; Dumesic, J. A., Hydrogen from catalytic reforming of biomass-derived hydrocarbons in liquid water. *Nature* **2002**, *418*, 964-967.
11. Huber, G. W.; Dumesic, J. A., An overview of aqueous-phase catalytic processes for production of hydrogen and alkanes in a biorefinery. *Catal. Today* **2006**, *111*, 119-132.
12. Davda, R. R.; Dumesic, J. A., Renewable hydrogen by aqueous-phase reforming of glucose. *Chem. Commun.* **2004**, 36-37.
13. Wen, G.; Xu, Y.; Ma, H.; Xu, Z.; Tian, Z., Production of hydrogen by aqueous-phase reforming of glycerol. *Int. J. Hydrogen Energy* **2008**, *33*, 6657-6666.

14. Davda, R. R.; Shabaker, J. W.; Huber, G. W.; Cortright, R. D.; Dumesic, J. A., A review of catalytic issues and process conditions for renewable hydrogen and alkanes by aqueous-phase reforming of oxygenated hydrocarbons over supported metal catalysts. *Appl. Catal. B* **2005**, *56*, 171-186.
15. Coronado, I.; Stekrova, M.; Reinikainen, M.; Simell, P.; Lefferts, L.; Lehtonen, J., A review of catalytic aqueous-phase reforming of oxygenated hydrocarbons derived from biorefinery water fractions. *Int. J. Hydrogen Energy* **2016**, *41*, 11003-11032.
16. Huang, Y.-B.; Fu, Y., Hydrolysis of cellulose to glucose by solid acid catalysts. *Green Chem.* **2013**, *15*, 1095-1111.
17. Cantero, D. A.; Sánchez Tapia, Á.; Bermejo, M. D.; Cocero, M. J., Pressure and temperature effect on cellulose hydrolysis in pressurized water. *Chem. Eng. J.* **2015**, *276*, 145-154.
18. Ciftci, A.; Eren, S.; Ligthart, D. A. J. M.; Hensen, E. J. M., Platinum–Rhenium Synergy on Reducible Oxide Supports in Aqueous-Phase Glycerol Reforming. *ChemCatChem* **2014**, *6*, 1260-1269.
19. Kim, T.-W.; Park, H. J.; Yang, Y.-C.; Jeong, S.-Y.; Kim, C.-U., Hydrogen production via the aqueous phase reforming of polyols over three dimensionally mesoporous carbon supported catalysts. *Int. J. Hydrogen Energy* **2014**, *39*, 11509-11516.
20. Kim, H.-D.; Park, H. J.; Kim, T.-W.; Jeong, K.-E.; Chae, H.-J.; Jeong, S.-Y.; Lee, C.-H.; Kim, C.-U., Hydrogen production through the aqueous phase reforming of ethylene glycol over supported Pt-based bimetallic catalysts. *Int. J. Hydrogen Energy* **2012**, *37*, 8310-8317.
21. Huber, G. W.; Shabaker, J. W.; Evans, S. T.; Dumesic, J. A., Aqueous-phase reforming of ethylene glycol over supported Pt and Pd bimetallic catalysts. *Appl. Catal. B* **2006**, *62*, 226-235.
22. Sakamoto, T.; Miyao, T.; Yoshida, A.; Naito, S., Effect of Re and Mo addition upon liquid phase methanol reforming with water over SiO₂, ZrO₂ and TiO₂ supported Ir catalysts. *Int. J. Hydrogen Energy* **2010**, *35*, 6203-6209.
23. Luo, N.; Fu, X.; Cao, F.; Xiao, T.; Edwards, P. P., Glycerol aqueous phase reforming for hydrogen generation over Pt catalyst–Effect of catalyst composition and reaction conditions. *Fuel* **2008**, *87*, 3483-3489.
24. Subramanian, N. D.; Callison, J.; Catlow, C. R. A.; Wells, P. P.; Dimitratos, N., Optimised hydrogen production by aqueous phase reforming of glycerol on Pt/Al₂O₃. *Int. J. Hydrogen Energy* **2016**, *41*, 18441-18450.
25. Neira D'Angelo, M. F.; Ordonsky, V.; van der Schaaf, J.; Schouten, J. C.; Nijhuis, T. A., Aqueous phase reforming in a microchannel reactor: the effect of mass transfer on hydrogen selectivity. *Catal. Sci. Technol.* **2013**, *3*, 2834-2842.

26. Neira D'Angelo, M. F.; Ordonsky, V.; van der Schaaf, J.; Schouten, J. C.; Nijhuis, T. A., Continuous hydrogen stripping during aqueous phase reforming of sorbitol in a washcoated microchannel reactor with a Pt–Ru bimetallic catalyst. *Int. J. Hydrogen Energy* **2014**, *39*, 18069-18076.
27. Shabaker, J. W.; Huber, G. W.; Davda, R. R.; Cortright, R. D.; Dumesic, J. A., Aqueous-Phase Reforming of Ethylene Glycol Over Supported Platinum Catalysts. *Catal. Lett.* **2003**, *88*, 1-8.
28. Huber, G. W.; Shabaker, J.; Dumesic, J., Raney Ni-Sn catalyst for H₂ production from biomass-derived hydrocarbons. *Science* **2003**, *300*, 2075-2077.
29. So, J.; Chung, Y.; Sholl, D. S.; Sievers, C., In-situ ATR-IR study of surface reaction during aqueous phase reforming of glycerol, sorbitol and glucose over Pt/ γ -Al₂O₃. *Mol. Catal.* **2019**, *475*, 110423.
30. Barnes, R. B.; Bonner, L. G., The early history and the methods of infrared spectroscopy. *Am. J. Phys.* **1936**, *4*, 181-189.
31. Colthup, N. B.; Daly, L. H.; Wiberly, S. E., *Introduction to Infrared and Raman Spectroscopy*, Third edition ed.; Academic Press, Inc. and Harcourt Brace Jovanovich, Inc.: San Diego, CA, USA, 1990.
32. Mojet, B. L.; Ebbesen, S. D.; Lefferts, L., Light at the interface: the potential of attenuated total reflection infrared spectroscopy for understanding heterogeneous catalysis in water. *Chem. Soc. Rev.* **2010**, *39*, 4643-4655.
33. Shi, H.; Lercher, J. A.; Yu, X.-Y., Sailing into uncharted waters: recent advances in the in situ monitoring of catalytic processes in aqueous environments. *Catal. Sci. Technol.* **2015**, *5*, 3035-3060.
34. Koichumanova, K.; Visan, A.; Geerdink, B.; Lammertink, R. G. H.; Mojet, B. L.; Seshan, K.; Lefferts, L., ATR-IR spectroscopic cell for in situ studies at solid-liquid interface at elevated temperatures and pressures. *Catal. Today* **2017**, *283*, 185-194.
35. Sheppard, N., Infra-red spectra of adsorbed molecules. *Spectrochim. Acta, Part A* **1989**, *45*, 239-250.
36. Hollins, P., The Influence of surface defects on the infrared spectra of adsorbed species. *Surf. Sci.* **1992**, *16*, 51-94.
37. Pines, H.; Manassen, J., The Mechanism of Dehydration of Alcohols over Alumina Catalysts. In *Advances in Catalysis*, Eley, D. D.; Pines, H.; Weisz, P. B., Eds. Academic Press: 1966; Vol. 16, pp 49-93.
38. Zhang, Q.; Deng, W.; Wang, Y., Effect of size of catalytically active phases in the dehydrogenation of alcohols and the challenging selective oxidation of hydrocarbons. *Chem. Commun.* **2011**, *47*, 9275-9292.

39. Friedrich, A.; Schneider, S., Acceptorless Dehydrogenation of Alcohols: Perspectives for Synthesis and H₂ Storage. *ChemCatChem* **2009**, *1*, 72-73.
40. Mitsudome, T.; Mikami, Y.; Funai, H.; Mizugaki, T.; Jitsukawa, K.; Kaneda, K., Oxidant-Free Alcohol Dehydrogenation Using a Reusable Hydrotalcite-Supported Silver Nanoparticle Catalyst. *Angew. Chem., Int. Ed.* **2008**, *47*, 138-141.
41. Fang, W.; Zhang, Q.; Chen, J.; Deng, W.; Wang, Y., Gold nanoparticles on hydrotalcites as efficient catalysts for oxidant-free dehydrogenation of alcohols. *Chem. Commun.* **2010**, *46*, 1547-1549.
42. Xie, T.; Hare, B. J.; Meza-Morales, P. J.; Sievers, C.; Getman, R. B., Identification of the Active Sites in the Dehydrogenation of Methanol on Pt/ γ -Al₂O₃ from a Combined Density Functional Theory and Spectroscopic Analysis. *J. Phys. Chem. C* **2020**, *124*, 19015-19023.
43. Sievers, C.; Noda, Y.; Qi, L.; Albuquerque, E. M.; Rioux, R. M.; Scott, S. L., Phenomena Affecting Catalytic Reactions at Solid–Liquid Interfaces. *ACS Catal.* **2016**, *6*, 8286-8307.
44. Saleheen, M.; Heyden, A., Liquid-Phase Modeling in Heterogeneous Catalysis. *ACS Catal.* **2018**, *8*, 2188-2194.
45. Standard XPS Sensitivity Factors. ThermoFisher Scientific Avantage Data System, pp List of standard sensitivity factors for X-ray photoelectron spectroscopy.
46. Brunauer, S.; Emmett, P. H.; Teller, E., Adsorption of Gases in Multimolecular Layers. *J. Am. Chem. Soc.* **1938**, *60*, 309-319.
47. Tamura, M.; Shimizu, K.-i.; Satsuma, A., Comprehensive IR study on acid/base properties of metal oxides. *Appl. Catal. A: Gen.* **2012**, *433*, 135-145.
48. Liu, X.; Truitt, R. E., DRFT-IR Studies of the Surface of γ -Alumina. *J. Am. Chem. Soc.* **1997**, *119*, 9856-9860.
49. Busca, G.; Rossi, P. F.; Lorenzelli, V.; Benaissa, M.; Travert, J.; Lavalley, J. C., Microcalorimetric and Fourier transform infrared spectroscopic studies of methanol adsorption on alumina. *J. Phys. Chem.* **1985**, *89*, 5433-5439.
50. Krebs, H.-J.; Lüth, H., Evidence for two different adsorption sites of CO on Pt (111) from infrared reflection spectroscopy. *Appl. Phys.* **1977**, *14*, 337-342.
51. Kappers, M. J.; van der Maas, J. H., Correlation between CO frequency and Pt coordination number. A DRIFT study on supported Pt catalysts. *Catal. Lett.* **1991**, *10*, 365-373.

52. Kappers, M.; Miller, J.; Koningsberger, D., Deconvolution and curve fitting of IR spectra for CO adsorbed on Pt/K-LTL: Potassium promoter effect and adsorption site distribution. *J. Phys. Chem.* **1996**, *100*, 3227-3236.
53. Barth, R.; Ramachandran, A., Temperature effects on the infrared spectrum of carbon monoxide adsorbed by supported platinum. *J. Catal.* **1990**, *125*, 467-471.
54. Deshlahra, P.; Conway, J.; Wolf, E. E.; Schneider, W. F., Influence of Dipole–Dipole Interactions on Coverage-Dependent Adsorption: CO and NO on Pt(111). *Langmuir* **2012**, *28*, 8408-8417.
55. Ding, K.; Gulec, A.; Johnson, A. M.; Schweitzer, N. M.; Stucky, G. D.; Marks, L. D.; Stair, P. C., Identification of active sites in CO oxidation and water-gas shift over supported Pt catalysts. *Science* **2015**, *350*, 189-192.
56. Dessal, C.; Len, T.; Morfin, F.; Rousset, J.-L.; Aouine, M.; Afanasiev, P.; Piccolo, L., Dynamics of single Pt atoms on alumina during CO oxidation monitored by operando X-ray and infrared spectroscopies. *ACS Catal.* **2019**, *9*, 5752-5759.
57. Zhao, Y.; Wang, L.; Kochubei, A.; Yang, W.; Xu, H.; Luo, Y.; Baiker, A.; Huang, J.; Wang, Z.; Jiang, Y., Formation and Location of Pt Single Sites Induced by Pentacoordinated Al Species on Amorphous Silica–Alumina. *J. Phys. Chem. Lett.* **2021**, *12*, 2536-2546.
58. Ebbesen, S. D.; Mojet, B. L.; Lefferts, L., In situ ATR-IR study of CO adsorption and oxidation over Pt/Al₂O₃ in gas and aqueous phase: Promotion effects by water and pH. *J. Catal.* **2007**, *246*, 66-73.
59. Germani, G.; Schuurman, Y., Water-gas shift reaction kinetics over μ -structured Pt/CeO₂/Al₂O₃ catalysts. *AIChE J.* **2006**, *52*, 1806-1813.
60. Amenomiya, Y., Active sites of solid acidic catalysts: III. Infrared study of the water gas conversion reaction on alumina. *J. Catal.* **1979**, *57*, 64-71.
61. Goguuet, A.; Meunier, F. C.; Tibiletti, D.; Breen, J. P.; Burch, R., Spectrokinetic Investigation of Reverse Water-Gas Shift Reaction Intermediates over a Pt/CeO₂ Catalyst. *J. Phys. Chem. B* **2004**, *108*, 20240-20246.
62. Wagner, F. T.; Moylan, T. E.; Schmiege, S. J., Hydrophilic versus hydrophobic coadsorption: Carbon monoxide and water on Rh(111) versus Pt(111). *Surf. Sci.* **1988**, *195*, 403-428.
63. Weller, M.; Overton, T.; Rourke, J.; Armstrong, F., *Inorganic Chemistry*, 7th ed.; Oxford University Press: New York, NY 10016, United States of America, 2018.
64. Vannice, M. A.; Twu, C. C., Extinction coefficients and integrated intensities for linear- and bridged-bonded CO on platinum. *J. Chem. Phys* **1981**, *75*, 5944-5948.

65. Beden, B.; Bewick, A.; Kunitatsu, K.; Lamy, C., Infrared study of adsorbed species on electrodes: Adsorption of carbon monoxide on Pt, Rh and Au. *J. Electroanal. Chem. Interfacial Electrochem.* **1982**, *142*, 345-356.
66. Copeland, J. R.; Foo, G. S.; Harrison, L. A.; Sievers, C., In situ ATR-IR study on aqueous phase reforming reactions of glycerol over a Pt/ γ -Al₂O₃ catalyst. *Catal. Tod.* **2013**, *205*, 49-59.
67. Garnier, A.; Sall, S.; Garin, F.; Chetcuti, M. J.; Petit, C., Site effects in the adsorption of carbon monoxide on real 1.8nm Pt nanoparticles: An Infrared investigation in time and temperature. *J. Mol. Cat. A: Chem.* **2013**, *373*, 127-134.
68. Hollins, P.; Pritchard, J., Infrared studies of chemisorbed layers on single crystals. *Prog. Surf. Sci.* **1985**, *19*, 275-349.
69. Queau, R.; Labroue, D.; Poilblanc, R., Interactions of chlorine and bromine with chemisorbed carbon monoxide on evaporated platinum, rhodium, and iridium films. *J. Catal.* **1981**, *69*, 249-253.
70. Qiao, B.; Wang, A.; Yang, X.; Allard, L. F.; Jiang, Z.; Cui, Y.; Liu, J.; Li, J.; Zhang, T., Single-atom catalysis of CO oxidation using Pt₁/FeO_x. *Nat. Chem.* **2011**, *3*, 634-641.
71. Olsen, C. W.; Masel, R. I., An infrared study of CO adsorption on Pt(111). *Surf. Sci.* **1988**, *201*, 444-460.
72. Tüshaus, M.; Schweizer, E.; Hollins, P.; Bradshaw, A., Yet another vibrational study of the adsorption system Pt {111}-CO. *J. Electron Spectrosc. Relat. Phenom.* **1987**, *44*, 305-316.
73. Raval, R.; Haq, S.; Harrison, M.; Blyholder, G.; King, D., Molecular adsorbate-induced surface reconstruction: CO/Pd {110}. *Chem. Phys. Lett.* **1990**, *167*, 391-398.
74. Brako, R.; Šokčević, D., Adsorbate interactions of CO chemisorbed on Pt (111). *Surf. Sci.* **1998**, *401*, L388-L394.
75. Petrova, N. V.; Yakovkin, I. N., Lateral interaction and CO adlayer structures on the Pt(111) surface. *Surf. Sci.* **2002**, *519*, 90-100.
76. Myshlyavtsev, A.; Zhdanov, V., Surface reconstruction and thermal desorption: the missing-row model for carbon monoxide/platinum (110). *Langmuir* **1993**, *9*, 1290-1298.
77. Hofmann, P.; Bare, S. R.; King, D. A., Surface phase transitions in CO chemisorption on Pt {110}. *Surf. Sci.* **1982**, *117*, 245-256.
78. Tao, F.; Dag, S.; Wang, L.-W.; Liu, Z.; Butcher, D. R.; Bluhm, H.; Salmeron, M.; Somorjai, G. A., Break-up of stepped platinum catalyst surfaces by high CO coverage. *Science* **2010**, *327*, 850-853.

79. Behm, R.; Thiel, P.; Norton, P.; Ertl, G., The interaction of CO and Pt (100). I. Mechanism of adsorption and Pt phase transition. *J. Chem. Phys.* **1983**, 78, 7437-7447.
80. van Beurden, P.; Verhoeven, H.; Kramer, G.; Thijsse, B., Atomistic potential for adsorbate/surface systems: CO on Pt. *Phys. Rev. B* **2002**, 66, 235409.
81. Cheah, S. K.; Bernardet, V. r. P.; Franco, A. A.; Lemaire, O.; Gelin, P., Study of CO and hydrogen interactions on carbon-supported Pt nanoparticles by quadrupole mass spectrometry and operando diffuse reflectance FTIR spectroscopy. *J. Phys. Chem. C* **2013**, 117, 22756-22767.
82. Roman, T.; Nakanishi, H.; Kasai, H., Coadsorbed H and CO interaction on platinum. *Phys. Chem. Chem. Phys.* **2008**, 10, 6052-6057.
83. Zhou, P.; Zhang, H.; Ji, H.; Ma, W.; Chen, C.; Zhao, J., Identifying the active photocatalytic H₂-production sites on TiO₂-supported Pt nanoparticles by the in-situ infrared spectrum of CO. *Sci. China Chem.* **2020**, 63, 354-360.
84. Wei, G.-F.; Liu, Z.-P., Restructuring and hydrogen evolution on Pt nanoparticle. *Chem. Sci.* **2015**, 6, 1485-1490.
85. Kajiwarra, R.; Asaumi, Y.; Nakamura, M.; Hoshi, N., Active sites for the hydrogen oxidation and the hydrogen evolution reactions on the high index planes of Pt. *J. Electroanal. Chem.* **2011**, 657, 61-65.
86. Gudmundsdóttir, S.; Skúlason, E.; Jónsson, H., Reentrant Mechanism for Associative Desorption: H₂/Pt (110)–(1×2). *Phys. Rev. Lett.* **2012**, 108, 156101.
87. Modica, F.; Miller, J.; Meyers, B.; Koningsberger, D., Role of spill-over hydrogen in the hydrogenolysis of neopentane. *Catal. Tod.* **1994**, 21, 37-48.
88. Stoica, M.; Caldararu, M.; Rusu, F.; Ionescu, N., Some experimental evidences for hydrogen spillover on Pt/Al₂O₃ catalysts by electrical conductivity transient response. *Appl. Catal. A: Gen.* **1999**, 183, 287-293.
89. Karim, W.; Spreafico, C.; Kleibert, A.; Gobrecht, J.; VandeVondele, J.; Ekinici, Y.; van Bokhoven, J. A., Catalyst support effects on hydrogen spillover. *Nature* **2017**, 541, 68-71.
90. RJ, B. S.; Loganathan, M.; Shantha, M. S., A review of the water gas shift reaction kinetics. *Int. J. Chem. React. Eng.* **2010**, 8.
91. Ravenelle, R. M.; Copeland, J. R.; Kim, W.-G.; Crittenden, J. C.; Sievers, C., Structural Changes of γ -Al₂O₃-Supported Catalysts in Hot Liquid Water. *ACS Catal.* **2011**, 1, 552-561.

92. Ciftci, A.; Peng, B.; Jentys, A.; Lercher, J. A.; Hensen, E. J., Support effects in the aqueous phase reforming of glycerol over supported platinum catalysts. *Appl. Catal., A* **2012**, *431*, 113-119.
93. Koichumanova, K.; Gupta, K. S. S.; Lefferts, L.; Mojet, B.; Seshan, K., An in situ ATR-IR spectroscopy study of aluminas under aqueous phase reforming conditions. *Phys. Chem. Chem. Phys.* **2015**, *17*, 23795-23804.
94. Nortier, P.; Fourre, P.; Saad, A. B. M.; Saur, O.; Lavalley, J. C., Effects of crystallinity and morphology on the surface properties of alumina. *Appl. Catal.* **1990**, *61*, 141-160.
95. Men, Y.; Gnaser, H.; Ziegler, C., Adsorption/desorption studies on nanocrystalline alumina surfaces. *Anal. Bioanal. Chem.* **2003**, *375*, 912-916.
96. MacDonald, D. D.; Butler, P., The thermodynamics of the aluminium—water system at elevated temperatures. *Corros. Sci.* **1973**, *13*, 259-274.
97. den Dunnen, A.; van der Niet, M. J.; Badan, C.; Koper, M. T.; Juurlink, L. B., Long-range influence of steps on water adsorption on clean and D-covered Pt surfaces. *Phys. Chem. Chem. Phys.* **2015**, *17*, 8530-8537.
98. Mojet, B. L.; Miller, J. T.; Ramaker, D. E.; Koningsberger, D. C., A New Model Describing the Metal–Support Interaction in Noble Metal Catalysts. **1999**, *186*, 373–386.
99. van Santen, R. A., Coordination of carbon monoxide to transition-metal surfaces. *J. Chem. Soc., Faraday Trans. 1* **1987**, *83*, 1915-1934.
100. Kizhakevariam, N.; Jiang, X.; Weaver, M. J., Infrared spectroscopy of model electrochemical interfaces in ultrahigh vacuum: The archetypical case of carbon monoxide/water coadsorption on Pt (111). *J. Chem. Phys.* **1994**, *100*, 6750-6764.
101. Mokhtari, M.; Archer, E.; Bloomfield, N.; Harkin-Jones, E.; McIlhagger, A., A review of electrically conductive poly(ether ether ketone) materials. *Polym. Int.* **2021**, *70*, 1016-1025.
102. Shukla, D.; Negi, Y. S.; Uppadhyaya, J. S.; Kumar, V., Synthesis and Modification of Poly(ether ether ketone) and their Properties: A Review. *Polym. Rev.* **2012**, *52*, 189-228.
103. Morris, R. H., Asymmetric hydrogenation, transfer hydrogenation and hydrosilylation of ketones catalyzed by iron complexes. *Chem. Soc. Rev.* **2009**, *38*, 2282-2291.
104. Mäki-Arvela, P.; Simakova, I. L.; Murzin, D. Y., One-pot amination of aldehydes and ketones over heterogeneous catalysts for production of secondary amines. *Catal. Rev.* **2021**, 1-68.

105. Kell'in, A. V.; Maioli, A., Recent advances in the chemistry of 1, 3-diketones: Structural modifications and synthetic applications. *Curr. Org. Chem.* **2003**, *7*, 1855-1886.
106. Samanta, S.; Zhao, C.-G., Asymmetric direct aldol reaction of 1,2-diketones and ketones mediated by proline derivatives. *Tetrahedron Lett.* **2006**, *47*, 3383-3386.
107. Trueba, M.; Trasatti, S. P., γ -Alumina as a support for catalysts: a review of fundamental aspects. *Eur. J. Inorg. Chem.* **2005**, *2005*, 3393-3403.
108. Prins, R., On the structure of γ -Al₂O₃. **2020**, *392*, 336-346.
109. Dry, M. E., Practical and theoretical aspects of the catalytic Fischer-Tropsch process. *Appl. Catal. A: Gen.* **1996**, *138*, 319-344.
110. Pineda, M.; Palacios, J. M., The performance of a γ -Al₂O₃ catalyst for the Claus reaction at low temperature in a fixed bed reactor. *Appl. Catal. A: Gen.* **1996**, *136*, 81-96.
111. Knözinger, H.; Bühl, H.; Kochloefl, K., The dehydration of alcohols on alumina: XIV. Reactivity and mechanism. *J. Catal.* **1972**, *24*, 57-68.
112. Avery, N. R., EELS identification of the adsorbed species from acetone adsorption on Pt (111). *Surf. Sci.* **1983**, *125*, 771-786.
113. Lin, Y.; Ji, H.; Shen, Z.; Jia, Q.; Wang, D., Enhanced acetone sensing properties of Co₃O₄ nanosheets with highly exposed (111) planes. *J. Mater. Sci.: Mater. Electron.* **2016**, *27*, 2086-2095.
114. Würger, T.; Heckel, W.; Sellschopp, K.; Müller, S.; Stierle, A.; Wang, Y.; Noei, H.; Feldbauer, G., Adsorption of Acetone on Rutile TiO₂: A DFT and FTIRS Study. *J. Phys. Chem. C* **2018**, *122*, 19481-19490.
115. Vannice, M. A.; Erley, W.; Ibach, H., A RAIRS and HREELS study of acetone on Pt(111). *Surf. Sci.* **1991**, *254*, 1-11.
116. Gao, J.; Teplyakov, A. V., Chemical transformations of acetone on ZnO powder. *J. Catal.* **2014**, *319*, 136-141.
117. Johnston, S. M.; Mulligan, A.; Dhanak, V.; Kadodwala, M., The bonding of acetone on Cu(111). *Surf. Sci.* **2004**, *548*, 5-12.
118. Panov, A.; Fripiat, J., Acetone condensation reaction on acid catalysts. *J. Catal.* **1998**, *178*, 188-197.
119. Hanson, B. E.; Wieserman, L. F.; Wagner, G. W.; Kaufman, R. A., Identification of acetone enolate on γ -alumina: implications for the oligomerization and polymerization of adsorbed acetone. *Langmuir* **1987**, *3*, 549-555.

120. Qi, G.; Chu, Y.; Wang, Q.; Wang, X.; Li, Y.; Trébosc, J.; Lafon, O.; Xu, J.; Deng, F., gem-Diol-Type Intermediate in the Activation of a Ketone on Sn- β Zeolite as Studied by Solid-State NMR Spectroscopy. *Angew. Chem., Int. Ed.* **2020**, *59*, 19532-19538.
121. Senanayake, S. D.; Gordon, W. O.; Overbury, S. H.; Mullins, D. R., Adsorption and Reaction of Acetone over CeOx(111) Thin Films. *J. Phys. Chem. C* **2009**, *113*, 6208-6214.
122. Connor, P. A.; Dobson, K. D.; McQuillan, A. J., New sol-gel attenuated total reflection infrared spectroscopic method for analysis of adsorption at metal oxide surfaces in aqueous solutions. Chelation of TiO₂, ZrO₂, and Al₂O₃ surfaces by catechol, 8-quinolinol, and acetylacetone. *Langmuir* **1995**, *11*, 4193-4195.
123. Blanck, S.; Martí, C.; Loehlé, S.; Steinmann, S. N.; Michel, C., (Dis)Similarities of adsorption of diverse functional groups over alumina and hematite depending on the surface state. *J. Chem. Phys.* **2021**, *154*, 084701.
124. Sadeghian Lemraski, M.; Nadimi, E., Acetone gas sensing mechanism on zinc oxide surfaces: A first principles calculation. *Surf. Sci.* **2017**, *657*, 96-103.
125. Lin, F.; Wang, H.; Zhao, Y.; Fu, J.; Mei, D.; Jaegers, N. R.; Gao, F.; Wang, Y., Elucidation of Active Sites in Aldol Condensation of Acetone over Single-Facet Dominant Anatase TiO₂ (101) and (001) Catalysts. *JACS Au* **2021**, *1*, 41-52.
126. Innocenti, G., giadainnocenti/FTIR_analyzer. 2021, GitHub. https://github.com/giadainnocenti/FTIR_analyzer
127. Digne, M.; Sautet, P.; Raybaud, P.; Euzen, P.; Toulhoat, H., Use of DFT to achieve a rational understanding of acid–basic properties of γ -alumina surfaces. *J. Catal.* **2004**, *226*, 54-68.
128. Kresse, G.; Hafner, J., *Ab initio* molecular dynamics for liquid metals. *Phys. Rev. B* **1993**, *47*, 558-561.
129. Kresse, G.; Furthmüller, J., Efficiency of ab-initio total energy calculations for metals and semiconductors using a plane-wave basis set. *Comp. Mater. Sci.* **1996**, *6*, 15-50.
130. Kresse, G.; Furthmüller, J., Efficient iterative schemes for *ab initio* total-energy calculations using a plane-wave basis set. *Phys. Rev. B* **1996**, *54*, 11169-11186.
131. Hacene, M.; Anciaux-Sedrakian, A.; Rozanska, X.; Klahr, D.; Guignon, T.; Fleurat-Lessard, P., Accelerating VASP electronic structure calculations using graphic processing units. *J. Comput. Chem.* **2012**, *33*, 2581-2589.
132. Hutchinson, M.; Widom, M., VASP on a GPU: Application to exact-exchange calculations of the stability of elemental boron. *Comput. Phys. Commun.* **2012**, *183*, 1422-1426.

133. Mortensen, J. J.; Hansen, L. B.; Jacobsen, K. W., Real-space grid implementation of the projector augmented wave method. *Phys. Rev. B* **2005**, *71*, 035109.
134. Kresse, G.; Joubert, D., From ultrasoft pseudopotentials to the projector augmented-wave method. *Phys. Rev. B* **1999**, *59*, 1758-1775.
135. Perdew, J. P.; Burke, K.; Ernzerhof, M., Generalized Gradient Approximation Made Simple. *Phys. Rev. Lett.* **1996**, *77*, 3865-3868.
136. Grimme, S.; Antony, J.; Ehrlich, S.; Krieg, H., A consistent and accurate ab initio parametrization of density functional dispersion correction (DFT-D) for the 94 elements H-Pu. *J. Chem. Phys.* **2010**, *132*, 154104.
137. Grimme, S.; Ehrlich, S.; Goerigk, L., Effect of the damping function in dispersion corrected density functional theory. *J. Comput. Chem.* **2011**, *32*, 1456-1465.
138. Monkhorst, H. J.; Pack, J. D., Special points for Brillouin-zone integrations. *Phys. Rev. B* **1976**, *13*, 5188-5192.
139. Hare, B. J.; Garcia Carcamo, R. A.; Xie, T.; Meza-Morales, P. J.; Getman, R. B.; Sievers, C., Active sites and effects of co-adsorbed H₂O on isolated methanol dehydrogenation over Pt/ γ -Al₂O₃. *J. Catal.* **2021**, *402*, 218-228.
140. Busca, G., The surface of transitional aluminas: A critical review. *Catal. Tod.* **2014**, *226*, 2-13.
141. Zaki, M. I.; Hasan, M. A.; Al-Sagheer, F. A.; Pasupulety, L., Surface Chemistry of Acetone on Metal Oxides: IR Observation of Acetone Adsorption and Consequent Surface Reactions on Silica–Alumina versus Silica and Alumina. *Langmuir* **2000**, *16*, 430-436.
142. Panov, A.; Fripiat, J. J., An Infrared Spectroscopic Study of Acetone and Mesityl Oxide Adsorption on Acid Catalyst. *Langmuir* **1998**, *14*, 3788-3796.
143. Gray Jr, H.; Rasmussen, R.; Tunnicliff, D., The infrared and ultraviolet absorption spectra of two isomers of mesityl oxide. *J. Am. Chem. Soc.* **1947**, *69*, 1630-1631.
144. Najmi, S.; So, J.; Stavitski, E.; McDermott, W. P.; Lyu, Y.; Burt, S. P.; Hermans, I.; Sholl, D. S.; Sievers, C., In-situ IR Spectroscopy Study of Reactions of C₃ Oxygenates on Heteroatom (Sn, Mo, and W) doped BEA Zeolites and the Effect of Co-adsorbed Water. *ChemCatChem* **2021**, *13*, 445-458.
145. Faba, L.; Díaz, E.; Ordóñez, S., Gas phase acetone self-condensation over unsupported and supported Mg–Zr mixed-oxides catalysts. *Appl. Catal. B: Environ.* **2013**, *142-143*, 387-395.
146. Ramis, G.; Lorenzelli, V., Adsorption and oligomerization of isobutene on oxide catalyst surfaces. A Fourier-transform infrared study. *J. Chem. Soc., Faraday Trans. 1* **1989**, *85*, 137-146.

147. Koichumanova, K.; Vikla, A. K. K.; Cortese, R.; Ferrante, F.; Seshan, K.; Duca, D.; Lefferts, L., In situ ATR-IR studies in aqueous phase reforming of hydroxyacetone on Pt/ZrO₂ and Pt/AlO(OH) catalysts: The role of aldol condensation. *Appl. Catal. B: Environ.* **2018**, 232, 454-463.
148. Yaylayan, V. A.; Harty-Majors, S.; Ismail, A. A., Monitoring Carbonyl–Amine Reaction and Enolization of 1-Hydroxy-2-propanone (Acetol) by FTIR Spectroscopy. *J. Agric. Food Chem.* **1999**, 47, 2335-2340.
149. Hossain, M. A.; Mills, K. N.; Molley, A. M.; Rahaman, M. S.; Tulaphol, S.; Lalvani, S. B.; Dong, J.; Sunkara, M. K.; Sathitsuksanoh, N., Catalytic isomerization of dihydroxyacetone to lactic acid by heat treated zeolites. *Appl. Catal. A: Gen.* **2021**, 611, 117979.
150. Innocenti, G.; Papadopoulos, E.; Fornasari, G.; Cavani, F.; Medford, A. J.; Sievers, C., Continuous Liquid-Phase Upgrading of Dihydroxyacetone to Lactic Acid over Metal Phosphate Catalysts. *ACS Catal.* **2020**, 10, 11936-11950.
151. Temprado, M.; Roux, M. V.; Umnahanant, P.; Zhao, H.; Chickos, J. S., The Thermochemistry of 2,4-Pentanedione Revisited: Observance of a Nonzero Enthalpy of Mixing between Tautomers and Its Effects on Enthalpies of Formation. *J. Phys. Chem. B* **2005**, 109, 12590-12595.
152. Kytöki, A.; Rautiainen, A.; Root, A., Reaction of acetylacetone vapour with γ -alumina. *J. Chem. Soc., Faraday Trans.* **1997**, 93, 4079-4084.
153. Dickie, S. A.; McQuillan, A. J., In-Situ Infrared Spectroscopic Studies of Adsorption Processes on Boehmite Particle Films: Exchange of Surface Hydroxyl Groups Observed upon Chelation by Acetylacetone. *Langmuir* **2004**, 20, 11630-11636.
154. Dismukes, J.; Jones, L.; Bailar Jr, J. C., The Measurement of Metal-Ligand Bond Vibrations in Acetylacetonate Complexes. *J. Phys. Chem.* **1961**, 65, 792-795.
155. Tsyganova, E. I.; Dyagileva, L. M., The reactivity of metal β -diketonates in the thermal decomposition reaction. *Russ. Chem. Rev.* **1996**, 65, 315.
156. Grimm, S.; Baik, S.-J.; Hemberger, P.; Bodi, A.; Kempf, A. M.; Kasper, T.; Atakan, B., Gas-phase aluminium acetylacetonate decomposition: revision of the current mechanism by VUV synchrotron radiation. *Phys. Chem. Chem. Phys.* **2021**, 23, 15059-15075.
157. Profeta, L. T. M.; Sams, R. L.; Johnson, T. J.; Williams, S. D., Quantitative Infrared Intensity Studies of Vapor-Phase Glyoxal, Methylglyoxal, and 2,3-Butanedione (Diacetyl) with Vibrational Assignments. *J. Phys. Chem. A* **2011**, 115, 9886-9900.
158. Cross, S. N.; Rochester, C. H., Infrared study of the adsorption of diketones on silica immersed in carbon tetrachloride. *J. Chem. Soc., Faraday Trans. 1* **1978**, 74, 2130-2140.

159. Albright, H.; Davis, A. J.; Gomez-Lopez, J. L.; Vonesh, H. L.; Quach, P. K.; Lambert, T. H.; Schindler, C. S., Carbonyl–Olefin Metathesis. *Chem. Rev.* **2021**, *121*, 9359-9406.
160. Román-Leshkov, Y.; Davis, M. E., Activation of Carbonyl-Containing Molecules with Solid Lewis Acids in Aqueous Media. *ACS Catal.* **2011**, *1*, 1566-1580.
161. Hirva, P.; Pakkanen, T. A., The interaction of amine bases on the Lewis acid sites of aluminum oxide — a theoretical study. *Surf. Sci.* **1992**, *277*, 389-394.
162. Zecchina, A.; Platero, E. E.; Areán, C. O., Low temperature CO adsorption on alum-derived active alumina: An infrared investigation. *J. Catal.* **1987**, *107*, 244-247.
163. De Vito, D. A.; Gilardoni, F.; Kiwi-Minsker, L.; Morgantini, P.-Y.; Porchet, S.; Renken, A.; Weber, J., Theoretical investigation of the adsorption of methanol on the (110) surface of γ -alumina. *J. Mol. Struct.: THEOCHEM* **1999**, *469*, 7-14.
164. Tillotson, M. J.; Brett, P. M.; Bennett, R. A.; Grau-Crespo, R., Adsorption of organic molecules at the $\text{TiO}_2(110)$ surface: The effect of van der Waals interactions. *Surf. Sci.* **2015**, *632*, 142-153.
165. Lee, J.-K.; Kung, M. C.; Kung, H. H., Cooperative Catalysis: A New Development in Heterogeneous Catalysis. *Top. Catal.* **2008**, *49*, 136-144.
166. Kung, H. H.; Kung, M. C., Inspiration from Nature for Heterogeneous Catalysis. **2014**, *144*, 1643-1652.
167. Zaki, M. I.; Hasan, M. A.; Pasupulety, L., Surface Reactions of Acetone on Al_2O_3 , TiO_2 , ZrO_2 , and CeO_2 : IR Spectroscopic Assessment of Impacts of the Surface Acid–Base Properties. *Langmuir* **2001**, *17*, 768-774.
168. Perrin, C. L.; Chang, K.-L., The Complete Mechanism of an Aldol Condensation. *J. Org. Chem* **2016**, *81*, 5631-5635.
169. A. Yaylayan, V.; Harty-Majors, S.; A. Ismail, A., Investigation of dl-glyceraldehyde–dihydroxyacetone interconversion by FTIR spectroscopy. *Carbohydr. Res.* **1999**, *318*, 20-25.
170. Yamaguchi, S.; Yabushita, M.; Kim, M.; Hirayama, J.; Motokura, K.; Fukuoka, A.; Nakajima, K., Catalytic Conversion of Biomass-Derived Carbohydrates to Methyl Lactate by Acid–Base Bifunctional γ - Al_2O_3 . *ACS Sustainable Chem. Eng.* **2018**, *6*, 8113-8117.
171. Silva de Freitas, G. R.; Firme, C. L., New insights into the stability of alkenes and alkynes, fluoro-substituted or not: a DFT, G4, QTAIM and GVB study. *J. Mol. Model.* **2013**, *19*, 5267-5276.

172. Dougherty, D.; Brint, P.; McGlynn, S., Photoelectron spectroscopy of carbonyls. Lone-pair interactions in. α -, β -, γ -, and δ -dicarbonyls. *J. Am. Chem. Soc.* **1978**, *100*, 5597-5603.
173. Eriks, K.; Hayden, T. D.; Yang, S. H.; Chan, I. Y., Crystal and molecular structure of biacetyl (2,3-butanedione), (H₃CCO)₂, at -12 and -100.degree.C. *J. Am. Chem. Soc.* **1983**, *105*, 3940-3942.
174. Ausfelder, F.; Bazzanella, A., Hydrogen in the Chemical Industry. In *Hydrogen Science and Engineering : Materials, Processes, Systems and Technology*, Stolten, P. D. D.; Emonts, D. B., Eds. 2016; pp 19-40.
175. Armaroli, N.; Balzani, V., The Hydrogen Issue. *ChemSusChem* **2011**, *4*, 21-36.
176. Ramachandran, R.; Menon, R. K., An overview of industrial uses of hydrogen. *Int. J. Hydrogen Energy* **1998**, *23*, 593-598.
177. Sladkovskiy, D. A.; Godina, L. I.; Semikin, K. V.; Sladkovskaya, E. V.; Smirnova, D. A.; Murzin, D. Y., Process design and techno-economical analysis of hydrogen production by aqueous phase reforming of sorbitol. *Chem. Eng. Res. Des.* **2018**, *134*, 104-116.
178. Huber, G. W.; Cortright, R. D.; Dumesic, J. A., Renewable alkanes by aqueous-phase reforming of biomass-derived oxygenates. *Angew. Chem.* **2004**, *116*, 1575-1577.
179. Tanksale, A.; Beltramini, J. N.; Lu, G. Q., Reaction Mechanisms for Renewable Hydrogen from Liquid Phase Reforming of Sugar Compounds. *Dev. Chem. Eng. Miner. Process.* **2006**, *14*, 9-18.
180. Tanksale, A.; Wong, Y.; Beltramini, J.; Lu, G. Q., Hydrogen generation from liquid phase catalytic reforming of sugar solutions using metal-supported catalysts. *Int. J. Hydrogen Energy* **2007**, *32*, 717-724.
181. Vaidya, P. D.; Lopez-Sanchez, J. A., Review of hydrogen production by catalytic aqueous-phase reforming. *ChemistrySelect* **2017**, *2*, 6563-6576.
182. Zope, B. N.; Davis, R. J., Inhibition of gold and platinum catalysts by reactive intermediates produced in the selective oxidation of alcohols in liquid water. *Green Chem.* **2011**, *13*, 3484-3491.
183. Ide, M. S.; Falcone, D. D.; Davis, R. J., On the deactivation of supported platinum catalysts for selective oxidation of alcohols. *J. Catal.* **2014**, *311*, 295-305.
184. McManus, J. R.; Saliccioli, M.; Yu, W.; Vlachos, D. G.; Chen, J. G.; Vohs, J. M., Correlating the Surface Chemistry of C₂ and C₃ Aldoses with a C₆ Sugar: Reaction of Glucose, Glyceraldehyde, and Glycolaldehyde on Pd(111). *J. Phys. Chem. C* **2012**, *116*, 18891-18898.

185. Delbecq, F.; Sautet, P., Adsorption of aldehydes and ketones on platinum and palladium: influence of steps, open faces and metal nature: A theoretical study. *Surf. Sci.* **1993**, 295, 353-373.
186. Davis, J.; Barteau, M., Polymerization and decarbonylation reactions of aldehydes on the Pd (111) surface. *J. Am. Chem. Soc.* **1989**, 111, 1782-1792.
187. Davis, J. L.; Barteau, M. A., Decarbonylation and decomposition pathways of alcohol's on Pd(111). *Surf. Sci.* **1987**, 187, 387-406.
188. Mason, T. E., et al., The Spallation Neutron Source in Oak Ridge: A powerful tool for materials research. *Phys. B* **2006**, 385-386, 955-960.
189. Haaland, D. M., Infrared studies of CO adsorbed on Pt/Al₂O₃: Evidence for CO bonded in 3-fold coordination. *Surf. Sci.* **1987**, 185, 1-14.
190. McClellan, M. R.; Gland, J. L.; McFeeley, F. R., Carbon monoxide adsorption on the kinked Pt(321) surface. *Surf. Sci.* **1981**, 112, 63-77.
191. Hayden, B. E.; Kretzschmar, K.; Bradshaw, A. M., An infrared study of adsorption of CO on a stepped platinum surface. *Surf. Sci.* **1985**, 149, 394-406.
192. Hare, B. J.; Garcia Carcamo, R. A.; Getman, R. B.; Sievers, C., Surface Chemistry of Ketones and Diketones on Lewis Acidic γ -Al₂O₃ Probed by Infrared Spectroscopy. *J. Phys. Chem. C* **2022**, 126, 17554-17568.
193. Albers, P.; Angert, H.; Prescher, G.; Seibold, K., Catalyst poisoning by methyl groups. *Chem. Commun.* **1999**, 1619-1620.
194. Henderson, M. A.; Mitchell, G. E.; White, J. M., The chemisorption of methyl halides (Cl, Br and I) on Pt(111). *Surf. Sci.* **1987**, 184, L325-L331.
195. Howard Fairbrother, D.; Peng, X. D.; Viswanathan, R.; Stair, P. C.; Trenary, M.; Fan, J., Carbon-carbon coupling of methyl groups on Pt(111). *Surf. Sci. Lett.* **1993**, 285, L455-L460.
196. Graham, D.; Howard, J.; Waddington, T. C., Hydrogen adsorbed on platinum and nickel. Comparison with new incoherent inelastic neutron scattering data on some metal hydridocarbonyls. *J. Chem. Soc., Faraday Trans. 1* **1983**, 79, 1281-1287.
197. Avery, N. R.; Weinberg, W. H.; Anton, A. B.; Toby, B. H., End-on and side-on bonding of ketones to surfaces: Acetone on the Ru(001) and Pt(111) surfaces. *Phys. Rev. Lett.* **1983**, 51, 682-685.
198. Bond, G. C., The origins of particle size effects in heterogeneous catalysis. *Surf. Sci.* **1985**, 156, 966-981.

199. Loffreda, D., Theoretical insight of adsorption thermodynamics of multifunctional molecules on metal surfaces. *Surf. Sci.* **2006**, *600*, 2103-2112.
200. Loffreda, D., Structural Identification of Conjugated Molecules on Metal Surfaces by Means of Soft Vibrations. *Angew. Chem., Int. Ed.* **2006**, *45*, 6537-6540.
201. Mhadeshwar, A.; Vlachos, D., Microkinetic modeling for water-promoted CO oxidation, water– gas shift, and preferential oxidation of CO on Pt. *J. Phys. Chem. B* **2004**, *108*, 15246-15258.
202. Gong, X.-Q.; Hu, P.; Raval, R., The catalytic role of water in CO oxidation. *J. Chem. Phys.* **2003**, *119*, 6324-6334.
203. Michalak, W. D.; Krier, J. M.; Alayoglu, S.; Shin, J.-Y.; An, K.; Komvopoulos, K.; Liu, Z.; Somorjai, G. A., CO oxidation on PtSn nanoparticle catalysts occurs at the interface of Pt and Sn oxide domains formed under reaction conditions. *J. Catal.* **2014**, *312*, 17-25.
204. Justicia, J.; Baeza, J. A.; de Oliveira, A. S.; Calvo, L.; Heras, F.; Gilarranz, M. A., Aqueous-phase reforming of water-soluble compounds from pyrolysis bio-oils. *Renewable Energy* **2022**, *199*, 895-907.
205. Mäki-Arvela, P.; Murzin, D. Y., Effect of catalyst synthesis parameters on the metal particle size. *Appl. Catal. A: Gen.* **2013**, *451*, 251-281.
206. Dietrich, P. J.; Akatay, M. C.; Sollberger, F. G.; Stach, E. A.; Miller, J. T.; Delgass, W. N.; Ribeiro, F. H., Effect of Co Loading on the Activity and Selectivity of PtCo Aqueous Phase Reforming Catalysts. *ACS Catal.* **2014**, *4*, 480-491.
207. Carrara, N.; Badano, J. M.; Vailard, S.; Vera, C.; Quiroga, M., Selective Hydrogenation of Diketones on Supported Transition Metal Catalysts. *Catal. Lett.* **2020**, *150*, 461-470.
208. Houtman, C. J.; Barteau, M. A., Divergent pathways of acetaldehyde and ethanol decarbonylation on the Rh(111) surface. *J. Catal.* **1991**, *130*, 528-546.
209. Penner, S.; Wang, D.; Su, D. S.; Rupprechter, G.; Podloucky, R.; Schlögl, R.; Hayek, K., Platinum nanocrystals supported by silica, alumina and ceria: metal–support interaction due to high-temperature reduction in hydrogen. *Surf. Sci.* **2003**, *532-535*, 276-280.
210. Ravenelle, R. M.; Copeland, J. R.; Van Pelt, A. H.; Crittenden, J. C.; Sievers, C., Stability of Pt/ γ -Al₂O₃ catalysts in model biomass solutions. *Top. Catal.* **2012**, *55*, 162-174.
211. Van Cleve, T.; Underhill, D.; Veiga Rodrigues, M.; Sievers, C.; Medlin, J. W., Enhanced hydrothermal stability of γ -Al₂O₃ catalyst supports with alkyl phosphonate coatings. *Langmuir* **2018**, *34*, 3619-3625.

212. Pipitone, G.; Zoppi, G.; Pirone, R.; Bensaid, S., A critical review on catalyst design for aqueous phase reforming. *Int. J. Hydrogen Energy* **2022**, *47*, 151-180.
213. Greenler, R. G., Infrared Study of the Adsorption of Methanol and Ethanol on Aluminum Oxide. *J. Chem. Phys* **1962**, *37*, 2094-2100.
214. Kiwi-Minsker, L.; Porchet, S.; Moeckli, P.; Doepper, R.; Renken, A., Selective methylation of catechol: catalyst development and characterisation. In *Studies in Surface Science and Catalysis*, Hightower, J. W.; Nicholas Delgass, W.; Iglesia, E.; Bell, A. T., Eds. Elsevier: 1996; Vol. 101, pp 171-180.
215. Kagel, R. O., Infrared investigation of the adsorption and surface reactions of the C1 through C4 normal alcohols on γ -alumina. *J. Phys. Chem.* **1967**, *71*, 844-850.
216. Padmanabhan, V. R.; Eastburn, F. J., Mechanism of ether formation from alcohols over alumina catalyst. *J. Catal.* **1972**, *24*, 88-91.
217. Schiffino, R. S.; Merrill, R. P., A mechanistic study of the methanol dehydration reaction on γ -alumina catalyst. *J. Phys. Chem.* **1993**, *97*, 6425-6435.
218. Morávek, V.; Kraus, M.; Malysheva, L.; Paukshtis, E.; Yurchenko, E., IR study of dynamic behaviour of 2-propanol on alumina. *Collect. Czech. Chem. Commun.* **1988**, *53*, 459-465.
219. Falk, M.; Whalley, E., Infrared spectra of methanol and deuterated methanols in gas, liquid, and solid phases. *J. Chem. Phys.* **1961**, *34*, 1554-1568.
220. Plyler, E. K., Infrared spectra of methanol, ethanol, and *trans*-propanol. *J. Res. Natl. Bur. Stand.* **1952**, *48*, 281-286.
221. Bellamy, L.; Mayo, D., Infrared frequency effects of lone pair interactions with antibonding orbitals on adjacent atoms. *J. Phys. Chem.* **1976**, *80*, 1217-1220.
222. Vigué, H.; Quintard, P.; Merle-Méjean, T.; Lorenzelli, V., An FT-IR Study of the Chlorination of γ -Alumina Surfaces. *J. Eur. Ceram. Soc.* **1998**, *18*, 305-309.
223. Matyshak, V.; Berezina, L.; Sil'chenkova, O.; Tret'yakov, V.; Lin, G.; Rozovskii, A. Y., Properties of surface compounds in methanol conversion on γ -Al₂O₃: Data of in situ IR spectroscopy. *Kinet. Catal.* **2009**, *50*, 111-121.
224. Clet, G.; Goupil, J.-M.; Cornet, D., Chlorination of alumina: an IR spectroscopic study. *Bull. Soc. Chim. Fr.* **1997**, *134*, 223-233.
225. Parry, E. P., An Infrared Study of Pyridine Adsorbed on Acidic Solids: Characterization of Surface Acidity. *J. Catal.* **1963**, *2*, 371-379.
226. Digne, M.; Raybaud, P.; Sautet, P.; Guillaume, D.; Toulhoat, H., Atomic Scale Insights on Chlorinated γ -Alumina Surfaces. *J. Am. Chem. Soc.* **2008**, *130*, 11030-11039.

227. Frederick, B. G.; Apai, G.; Rhodin, T. N., Defect structure of clean and chlorinated aluminum oxide films probed by methanol chemisorption. *Surf. Sci.* **1992**, 277, 337-350.
228. Shelimov, B.; Lambert, J.-F.; Che, M.; Didillon, B., Initial Steps of the Alumina-Supported Platinum Catalyst Preparation: A Molecular Study by ¹⁹⁵Pt NMR, UV–Visible, EXAFS, and Raman Spectroscopy. *J. Catal.* **1999**, 185, 462-478.
229. Rogers, J.; Rub, B.; Goldman, S.; Person, W., Measurement of infrared intensities for fundamental vibrations of gaseous acetone. *J. Phys. Chem.* **1981**, 85, 3727-3729.
230. Lindenmaier, R.; Tipton, N.; Sams, R. L.; Brauer, C. S.; Blake, T. A.; Williams, S. D.; Johnson, T. J., Assignment of the Fundamental Modes of Hydroxyacetone Using Gas-Phase Infrared, Far-Infrared, Raman, and ab Initio Methods: Band Strengths for Atmospheric Measurements. *J. Phys. Chem. A* **2016**, 120, 5993-6003.
231. Mohaček-Grošev, V., Vibrational analysis of hydroxyacetone. *Spectrochim. Acta, Part A* **2005**, 61, 477-484.
232. Tayyari, S. F.; Milani-nejad, F., Vibrational assignment of acetylacetone. *Spectrochim. Acta, Part A* **2000**, 56, 2679-2691.
233. Noack, K.; Jones, R. N., The vibrational spectra of diacetyl and diacetyl-d₆. *Zeitschrift für Elektrochemie, Berichte der Bunsengesellschaft für physikalische Chemie* **1960**, 64, 707-713.